December 2020

Ultrafast Laser Pulse Interaction with Dielectric Materials: Numerical and Experimental Investigations on Ablation and Micromachining

Xiao Jia
Clemson University, xiaoj906@gmail.com

ULTRAFAST LASER PULSE INTERACTION WITH DIELECTRIC MATERIALS: NUMERICAL AND EXPERIMENTAL INVESTIGATIONS ON ABLATION AND MICROMACHINING

A Dissertation
Presented to
the Graduate School of
Clemson University

In Partial Fulfillment
of the Requirements for the Degree
Doctor of Philosophy
Mechanical Engineering

---

by
Xiao Jia
December 2020

Accepted by:
Dr. Xin Zhao, Committee Chair
Dr. Gang Li
Dr. Laine Mears
Dr. Hongseok Choi

ABSTRACT

Ultrafast lasers have great capability and flexibility in micromachining of various materials. Due to the involved complicated multi-physical processes, mechanisms during laser-material interaction have not been fully understood. To improve and explore ultrafast laser processing and treatment of dielectric materials, numerical and experimental investigations have been devoted to better understanding the underlying fundamental physics during laser-material interaction and material micromachining.

A combined continuum-atomistic model has been developed to investigate thermal and non-thermal (photomechanical) responses of materials to ultrafast laser pulse irradiation. Coexistence of phase explosion and spallation can be observed for a considerably wide range of laser fluences. Phase explosion becomes the primary ablation mechanism with the increase of laser fluence, and spallation can be restrained due to the weakened tensile stress by the generation of recoil pressure from ejection of hot material plume. For dielectric materials, due to the much lower temperature gradient by non-linear absorption, the generated thermal-elastic stress is much weaker than that in non-transparent materials, making spallation less important. Plasma dynamics is studied with respect to ejection directions and velocities based on fluorescence and shadowgraph measurements. The most probable direction (angle) is found insensitive to laser fluence/energy. The plasma expansion velocity is closely related to electron thermal velocity, indicating the significance of thermal ablation in dielectric material decomposition by laser irradiation.

A numerical study of ultrafast laser-induced ablation of dielectric materials is presented based on a one-dimensional plasma-temperature model. Plasma dynamics

including photoionization, impact ionization and relaxation are considered through a single rate equation. Material decomposition is captured by a temperature-based ablation criterion. Dynamic description of ablation process has been achieved through an improved two-temperature model. Laser-induced ablation threshold, transient optical properties and ablation depth have been investigated with respect to incident fluences and pulse durations. Good agreements are shown between numerical predictions and experimental observations. Fast increase of ablation depth, followed by saturation, can be observed with the increase of laser fluence. Reduction of ablation depth at fluences over 20 J/cm^2 is resulted from plasma defocusing effect by air ionization. Thermal accumulation effect can be negligible with repetition rate lower than 1 kHz for fused silica and helps to enhance the ablation depth at 10 kHz (100 pulses) to almost double of that with single pulse. The ablation efficiency decreases with fluence after reaching the peak value at the fluence twice of the ablation threshold. The divergence of tightly focused Gaussian beam in transparent materials has been revealed to significantly affect the ablation process, particularly at high laser fluence.

A comprehensive study of ultrafast laser direct drilling in fused silica is performed with a wide range of drilling speeds (20-500 μm/s) and pulse energy (60-480 μJ). Taper-free and uniform channels are drilled with the maximum length over 2000 μm, aspect ratio as high as ~40:1 and excellent sidewall quality (roughness ~0.65 μm) at 270 μJ. The impacts of pulse energy and drilling speeds on channel aspect ratio and quality are studied. Optimal drilling speeds are determined at different pulse energy. The dominating mechanisms of channel early-termination are beam shielding by material modification at

excessive laser irradiation for low speed drilling and insufficient laser energy deposition for high speed drilling, respectively. An analytical model is developed to validate these mechanisms. The feasibility of direct drilling high-aspect-ratio and high-quality channels by ultrafast laser in transparent materials is demonstrated.

DEDICATION

This dissertation is dedicated to my family for their love and support.

ACKNOWLEDGMENTS

I would like to express my sincere gratitude to my academic advisor, Prof. Xin Zhao, for his immense knowledge, valuable advice, effective guidance, continuous patience, passionate encouragement, and kind support during my Ph.D. study at Clemson University. I also would like to thank Prof. Gang Li, Prof. Laine Mears and Prof. Hongseok Choi with all my heart for serving on my committee and their insightful comments for my study.

I am grateful to my fellow labmates, Yuxin Li, Kewei Li, Ankit Varma, Shreyas Limaye, Sai Kosaraju, who worked together with me on different projects, and gave me fruitful inspirations and advices.

I am also greatly thankful to my friends, Mingdong Song, Jixuan Gong, Xingchen Shao, Baobao Tang, Yingye Gan, Qian Mao and many other people, who enriched my life at Clemson University and gave me a lot of help in many aspects.

Finally, I want to deeply thank my family, for their selfless love, support, and encouragement during my Ph.D. study and in my whole life.

TABLE OF CONTENTS

Page

LIST OF TABLES

Table Page

LIST OF FIGURES

Figure Page

CHAPTER ONE

INTRODUCTION

1.1 Ultrafast laser-matter interaction

Ultrafast laser pulses refer to the laser pulses with the pulse duration in the order of femtosecond ($1fs=10^{-15}s$) to picosecond ($1ps=10^{-12}s$). Compared with the longer laser pulses (nanosecond=$10^{-9}s$ and millisecond=$10^{-6}s$), unique characteristics and advantages can be achieved during ultrafast laser pulses interaction with different materials, such as minimized heat-affected zones (as shown in Figure 1.1), ultrafast material ionization and plasma formation, which have attracted intensive attentions in the past several decades on the application of processing different materials with ultrafast lasers.

It has been demonstrated in [1] that ultrafast laser ablation has great advantages over longer laser pulses (ns). As shown in Figure 1.2, the molten materials are obvious in nanosecond laser ablation in metal, where the drilled hole has rough surfaces and edges. By contrast, in femtosecond laser ablation (Figure 1.2), the drilled hole shows sharp edges, smooth side walls, and very clean surfaces. This is also true for dielectric materials, as studied by [2]. It can be seen from Figure 1.3 that both the surface and the edge quality of the machined structures can be improved and better controlled by ultrafast laser pulses. With longer pulses, due to the brittleness of fused silica, the structure can be heavily broken with 3 ps laser pulses. While for femtosecond laser pulses, the resultant structures can be far better controlled during the interaction between fused silica and the laser pulses.

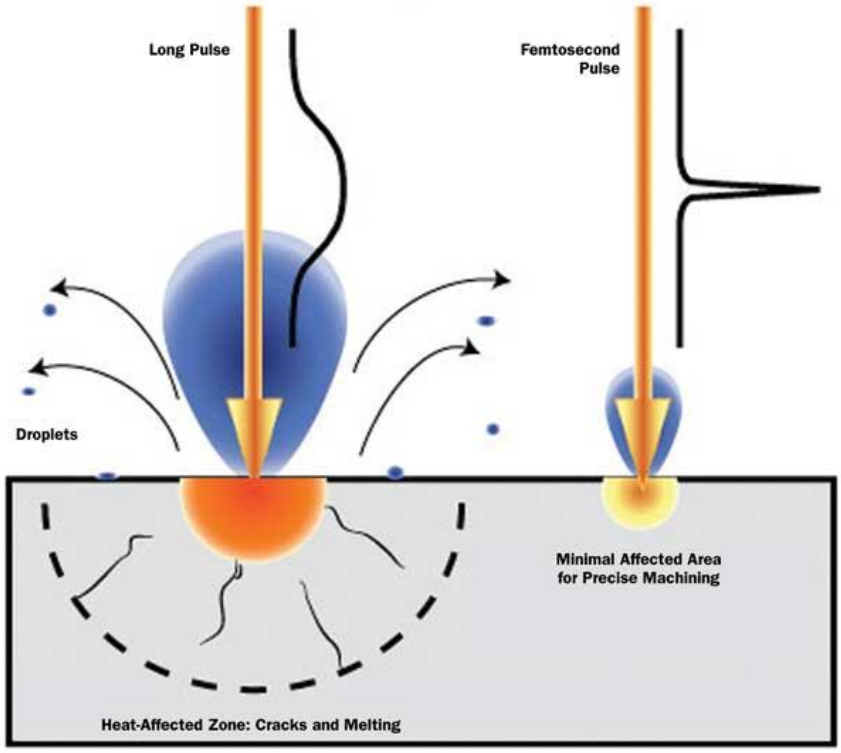

Figure 1.1 Material processing side effects of long laser pulses compared with femtosecond laser pulses [3].

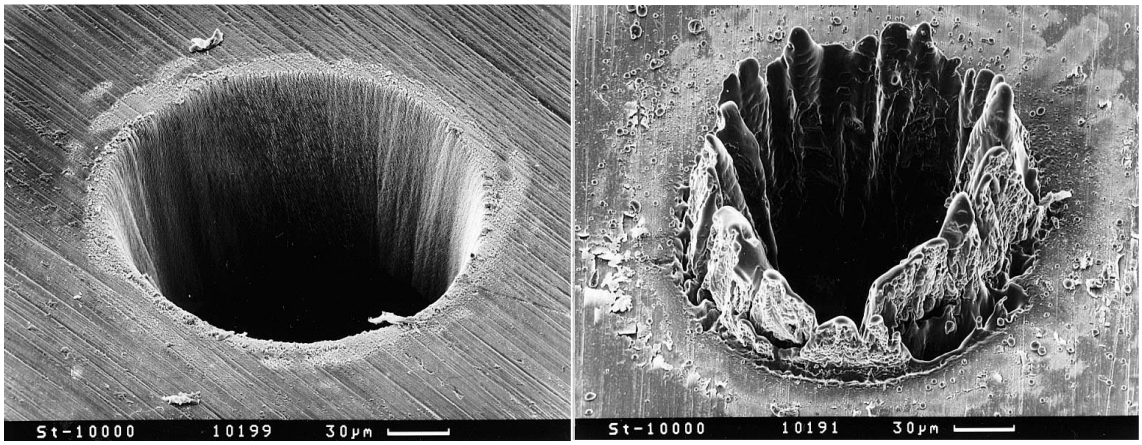

Figure 1.2 SEM micrographs of pulse laser ablation and hole drilled in a 100 µm thick steel foil with (a) pulse duration 200 fs, fluence 0.5 J/cm^2, (b) pulse duration 3.3 ns, fluence 4.2 J/cm^2 [1].

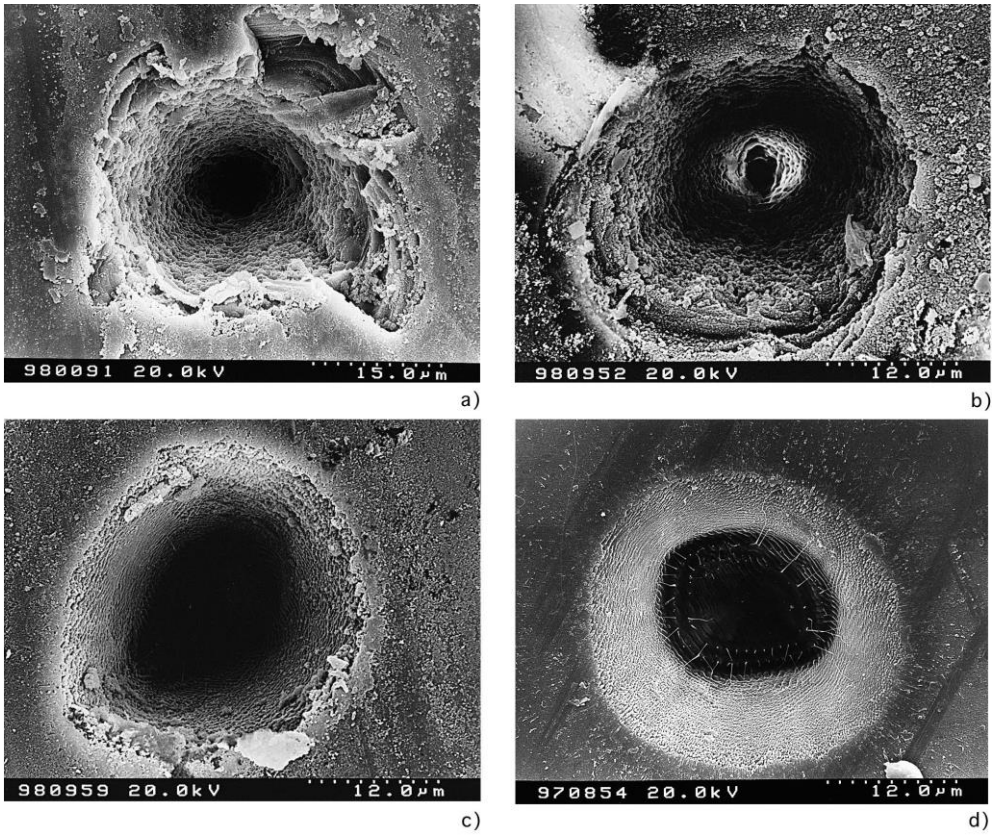

Figure 1.3 SEM micrographs of pulse laser ablated fused silica at air, (a) pulse duration 3 ps, fluence 19.9 J/cm^2, (b) pulse duration 220 fs, fluence 10.7 J/cm^2, (c) pulse duration 20 fs, fluence 11.1 J/cm^2, (d) pulse duration 5 fs, fluence 6.9 J/cm^2 [2].

Ultrafast laser-matter interaction is highly complicated and could be different for different materials, including metals, semiconductors and dielectrics. As shown in Figure 1.4, typically, the interaction between ultrafast laser pulses and electron is much faster than the thermal relaxation process between electron and lattice, so that laser heating of electrons is the essential process for laser pulse energy deposition into the material. For semiconductors and dielectrics, due to the lack of free electrons in the conduction band, there will be free electron excitation before the sufficient number of electrons can be heated.

The thermal equilibrium between electron and lattice can be achieved in the picosecond regime, through electron-lattice coupling. When the ablation critical condition has been satisfied, the ablated material starts to be ejected from the base material, and this ejection process can last to the nanosecond range. Due to the localized thermal process of electrons, fast energy transfers in the material and continuous material ejection, thermal diffusion in the base material is significantly inhibited and the heat affected zones are greatly reduced, which enables high-precision processing of materials.

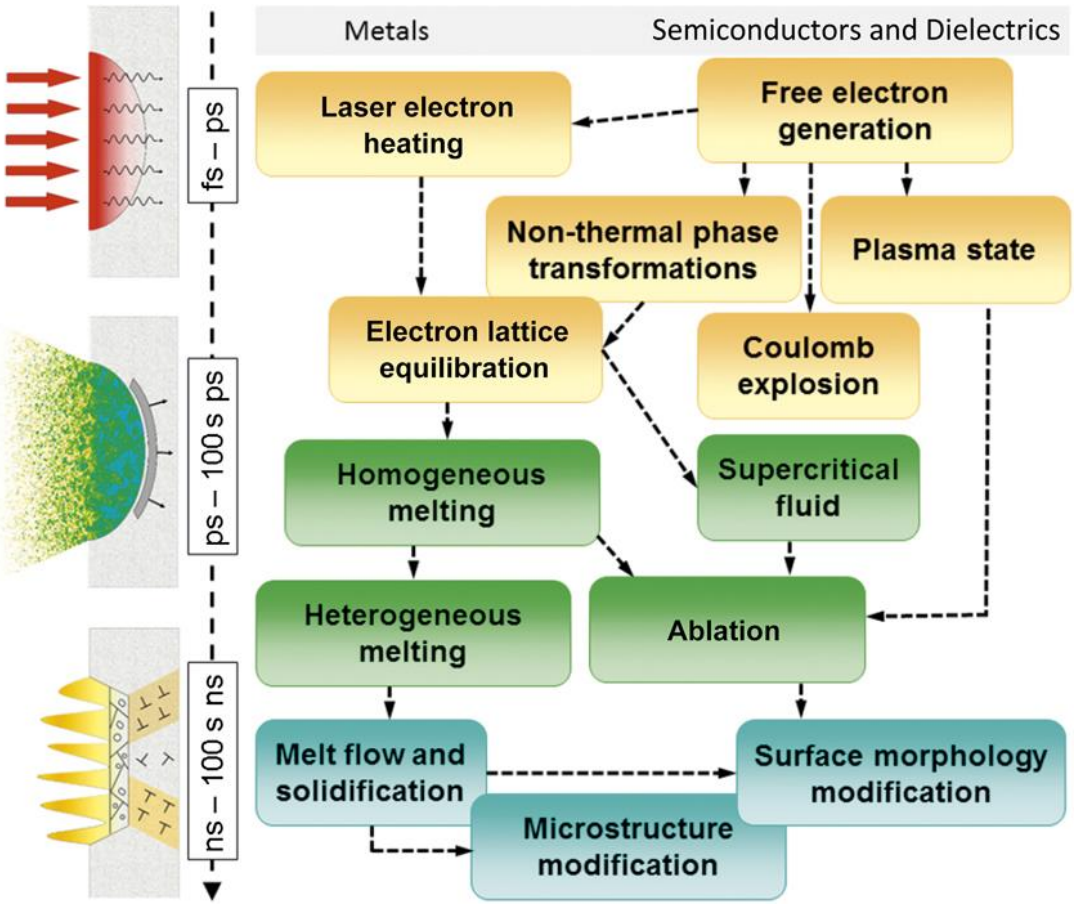

Figure 1.4 Typical pathways of energy dissipation and phase transformations following the excitation of a material by an ultrafast laser pulse. Note: ns, nanosecond; ps, picosecond; fs, femtosecond [4].

Within the ultrafast laser pulse duration, extremely high laser intensity can be obtained, typically above the magnitude of TW/cm^2. This is particularly important for dielectric materials because free electron has to be excited before efficient laser energy deposition on the material can happen. Due to the wide bandgap of dielectrics, electrons cannot be excited through linear absorption of laser energy in visible and NIR wavelengths. When the laser intensity is sufficiently high, photoionization can be triggered to deposit laser energy in dielectrics. Since it is much more easily to achieve high laser intensity, ultrafast laser pulses can be taken advantages to process transparent materials (dielectrics) and fabricate a variety of optical components, such as waveguides, couplers, Bragg gratings, and micro-/nano-channels for microfluidic application in micro-total analysis systems (μ-TAS). For better application of ultrafast laser in micromachining of dielectric materials, it is important to understand the underlying multi-physical processes during laser-material interaction.

Numerous experimental and numerical studies have been devoted to investigating the physical processes, however, they are still not clearly understood due to the complicated multi-physical process and interrelation between different mechanisms. Therefore, it is necessary to conduct further investigation on the fundamental physics during ultrafast laser-material interaction to improve the applicability of ultrafast lasers in precise micro-/nano-machining. Major ablation mechanisms, electronic excitation, numerical modeling approaches and micro-drilling in silica glass will be reviewed in the following sections.

1.2 Laser ablation mechanisms

Laser ablation refers to disintegration and ejection of material under laser irradiation. Highly localized ablation can be induced by ultrafast laser pulses, due to the ultrafast excitation and rapid removal of material, as shown in Figure 1.5. Due to ultrashort period for energy dissipation inside the material, thermal diffusion can be minimized, so that high-precision micro-/nano-scale structures can be induced in the material and the heat-affected zone is limited within nanometer to micrometer. Ablation can happen with different mechanisms, depending on the material and laser conditions (pulse duration, wavelength, energy, and polarization, etc.). Due to the thermal nature of laser-material interaction, thermal ablation is the dominant process responsible for material removal. Meanwhile, non-thermal ablation should be considered when non-thermal processes (at low temperature) are important during material disintegration.

1.2.1 Thermal ablation

With ultrafast laser pulse irradiation, large amount of energy is absorbed by electrons. Material will undergo thermal non-equilibrium states, with continuous energy transfer between electron and lattice. When sufficient energy has been gained inside the lattice, atoms and ions will be able to overcome the energy barriers and escape from the material. This material removal process by high energy deposition and high temperature is termed as thermal ablation. Several thermal ablation mechanisms have been discussed, including phase explosion [5], critical-point phase separation [6], fragmentation [5], and vaporization [5]. With different mechanisms, the material will undergo different

thermodynamical processes and the ejected material can be characterized with dissimilar density, temperature, size and shape. The conditions when ablation can be induced, and the characteristics in different mechanisms are provided as follows.

1.2.1.1 Phase explosion

Normal boiling can be induced in liquid at relatively low speed of heating process, and heterogeneous evaporation happens in the substance with bubble nucleation from surfaces, impurities and grain boundaries. On the contrary, if the heating process is too fast for the liquid to relax to the binodal curve, the liquid will be superheated with temperature higher than the boiling point, and no longer follow the thermodynamic path as in normal boiling. Ultrafast laser interaction with material is such a fast heating process leading to formation of superheated liquid, which will relax along isentropes intersecting with the binodal curve between the triple and critical points, as shown in Figure 1.6 (b). When the material enters the metastable liquid region under binodal curve, it undergoes fluctuation in density, leading to the nucleation of gas bubbles. The liquid experiences homogeneous bubble nucleation, and explodes with the expansion of gas bubbles, resulting in a mixture of liquid droplets and vapors. This process is called phase explosion or explosive boiling. The occurrence of phase explosion can follow different thermodynamical paths for longer pulses, and the material expansion can happen during the heating process, but not necessarily during cooling as in femtosecond laser pulses. The material ejection in phase explosion is demonstrated in Figure 1.5 (region II), where homogeneous ablation happens

under the irradiation of ultrafast laser pulse, and mixture of liquid droplets and small clusters can be clearly observed in the ablation plume.

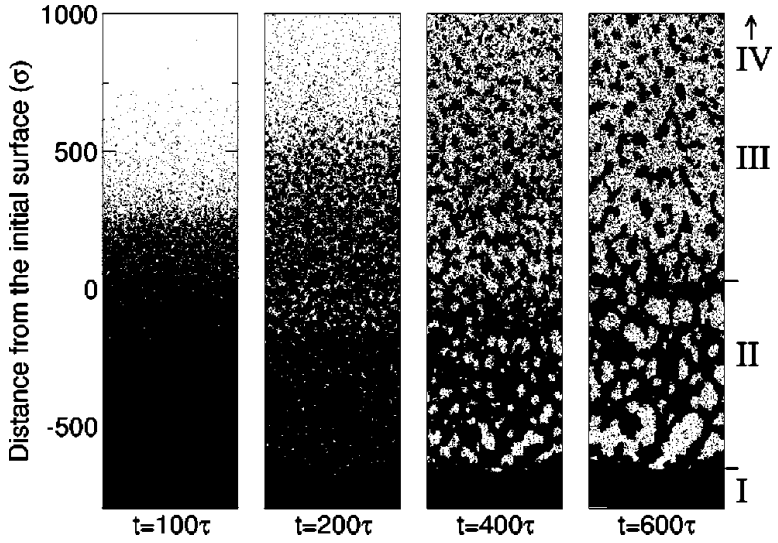

Figure 1.5 Atomic configuration at different time for laser ablation simulation with 100 fs pulse at fluence equal to 2.8 times of threshold. Roman numerals identify different regions of the target. Region IV is the gaseous region (out of the range of the laser snapshot) [5].

1.2.1.2 Critical-point phase separation (CPPS)

After the initial laser heating and the generation of hot plasma, but before phase separation, the material is heated well above the vapor-liquid critical temperature and expanded nearly adiabatically. When the adiabatic cooling path arrives close to the critical point, due to the thermodynamic instability, the material experiences phase separation via spinodal decomposition. This process is termed as CPPS [6]. Different from phase explosion, where simultaneous bubble nucleation occurs in the superheated liquid, CPPS results in phase separation when the matter is adiabatically cooled through the critical point with the formation of a bubble and droplet transition layer.

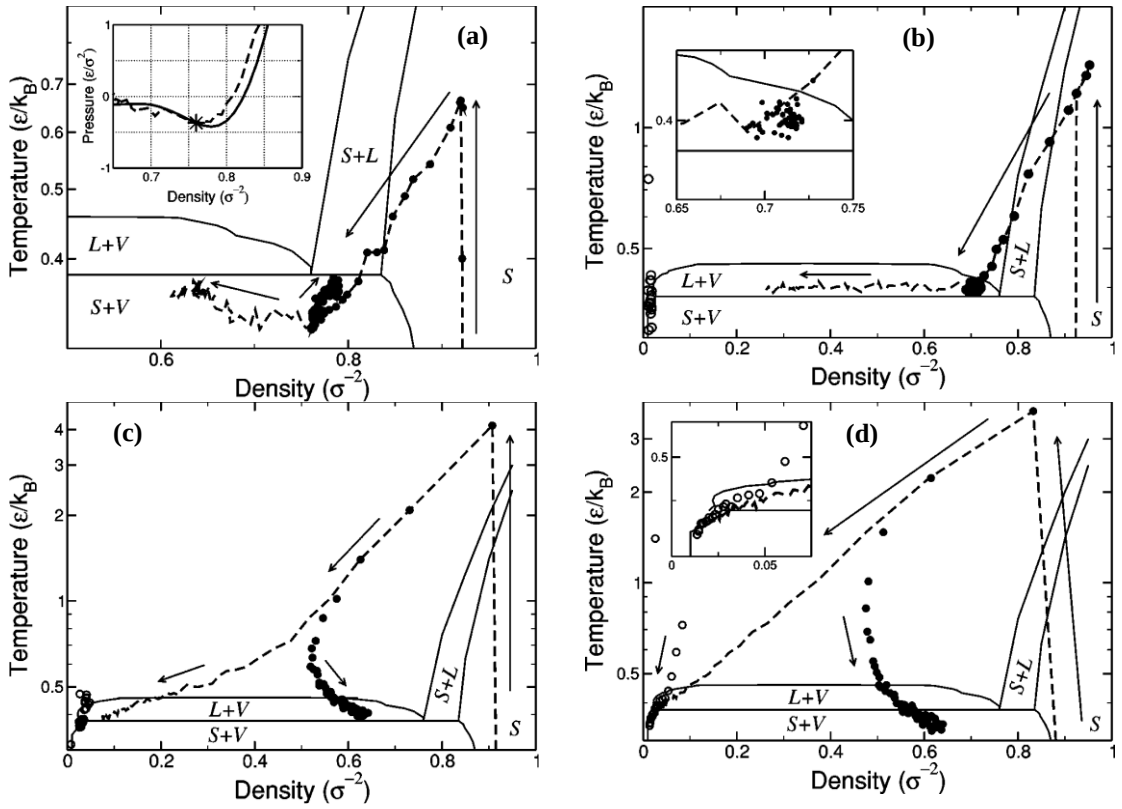

Figure 1.6 Thermodynamical evolution in the material for different ablation mechanisms, including (a) spallation (region I), (b) phase explosion (region II), (c) fragmentation (region III), (d) vaporization (region IV) [5].

1.2.1.3 Fragmentation

Fragmentation [7] is similar to the process of CPPS in that the rapidly heated material by ultrafast laser pulses undergoes expansion at large strain rates and phase separation during relaxation (cooling). The occurrence of void nucleation, development and phase separation in fragmentation is completed before entering the binodal curve, so that material has been decomposed when the material reaches the metastable region, as shown in Figure 1.6 (c). Fragmentation depends on both the relaxation isentrope and the

strain rate. The contribution of the fragmentation becomes more important than phase explosion with increasing laser energy absorption in the material.

1.2.1.4 Vaporization

For high incident laser energy, the surface layer of the material can be completely atomized, and the whole layer rapidly becomes gas due to the early phase separation of gas from the base material. As shown in Figure 1.6 (d), the cooling and expansion of this branch basically follows the ideal-gas isentropes, indicating the occurrence of vaporization process. With high energy exceeding the material cohesive energy, the topmost layers of material will undergo complete dissociation. Few large-size clusters can be found in this part of the plume, instead, monomers, such as ions, electrons, and neutron atoms will be the major composition. The contribution of the ablation from vaporization is much less than phase explosion and fragmentation.

1.2.2 Non-thermal ablation

Non-thermal ablation is defined to be distinguished from thermal ablation since the dominating driving force is non-thermal processes, including electronic or mechanical processes. Non-thermal ablation is generally observed with low laser pulse energy, where the absorbed energy is not sufficient to generate dense plasma (thermal ablation).

1.2.2.1 Coulomb explosion

Intense ultrafast laser pulse induces strong ionization at the material surface. The emission of electrons from the surface will leave a high concentration of positive charge.

Coulomb explosion originates from these net charge and unbalanced electric forces on the surface layer, which is able to pull out the ions with repulsive Coulomb forces [8,9]. The amount of uncompensated charge will be neutralized by charge losses through ion ejection (Coulomb explosion) or electron transportation from the bulk. The threshold condition to induce Coulomb explosion is the critical electrostatic force to overcome the local mechanical strength. Due to the high mobility of electrons in metals, the strong electric field after electron emission is not easy to form, so that Coulomb explosion is less likely to happen in metals than in dielectrics.

1.2.2.2 Spallation

There is another non-thermal ablation mechanism, spallation, induced by mechanical stress instead of electrical processes. The reason why spallation has been identified as non-thermal ablation is originated from its mechanical nature, following the terminology of mechanical breakdown of material in solid phase, although this process is thermal-assisted spallation in liquid phase. As shown in Figure 1.6 (a), the driving force of the material decomposition in spallation is the tensile stress induced by the ultrahigh shock wave under the thermal confinement condition. Occurrence of spallation is featured by void nucleation, growth, coalescence and disintegration of a whole layer of material, which cannot be atomized or further decomposed.

Spallation is proposed to be the dominant ablation mechanism with low laser energy. With rapid heating of material, there will be shock wave generation inside the material. This shock wave will propagate and form tensile wave when it reaches and reflects from

surfaces. Spallation will be triggered when the tensile wave reflected from the surface is able to overcome the material bonding or tensile strength.

Although different ablation mechanisms can dominate at different range of laser pulse energy, generally, these ablation mechanisms could happen simultaneously. The contribution from different ablation mechanisms are denoted in different colors in Figure 1.7. It can be clearly observed that spallation is the dominant ablation mechanism at relatively low laser fluences. With the increase of laser fluence (150 eV/A), phase explosion and fragmentation become the dominant ablation mechanisms. The reduction of spallation is resulted from the weakening or vanishing of tensile wave by the recoil pressure. With further increase of fluence, significant increase of fragmentation can be observed and becomes the dominant ablation mechanism at high laser fluence. Also, due to the increasingly heating of the top layer material, vaporization can be induced, and the contribution increases with laser fluences. Phase explosion, as shown in Figure 1.7, provides similar contribution of ablation at different conditions, and its requirement of heating is slightly lower than fragmentation. Therefore, it can be expected that phase explosion can be largely transformed to fragmentation. The relative contribution of different ablation mechanisms indicates the interrelation and transition between different mechanisms. This observation indicates that phase explosion and the mechanisms at higher temperature should account for most of the ablation, and non-thermal ablation (spallation) becomes less important at increasing laser fluences.

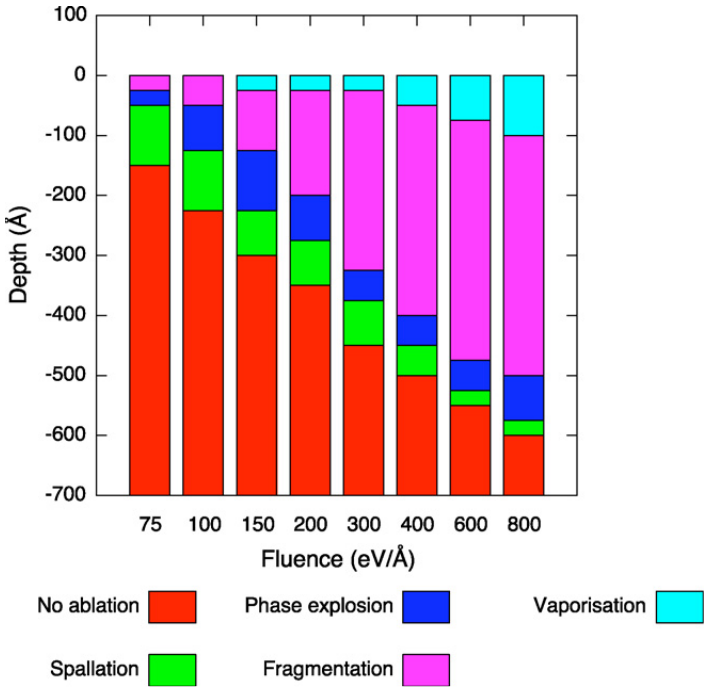

Figure 1.7 Contribution of ablation from different mechanisms for 200 fs laser pulses at various fluences [10].

1.3 Electron excitation in dielectric materials

Due to the absence of electrons on the conduction band, the interaction between dielectric materials with laser pulses is different from metals and semiconductors. For visible and near infrared lasers, since the bandgap in dielectric materials (fused silica, 9.0 eV) is much higher than the single photon energy, linear absorption (inverse Bremsstrahlung) is inhibited. With high laser intensities, there will be sufficient density of photons to enable multiphoton ionization (MPI), where valence-band electrons (VBE) can absorb multiple photons simultaneously and be excited to conduction-band electrons (CBE), as shown in Figure 1.8 (a). These conduction-band electrons (CBE) can absorb photons through linear absorption (Figure 1.8 (b)) and kinetic energy can be increased by

continuous photon absorption. When the energy of CBE is high enough, impact ionization (II) can be triggered through CBE collision with another VBE (Figure 1.8 (c)). During the early stage of laser pulse interaction (first half pulse), MPI process is the dominant ionization process to provide seeding electrons for II. In the late stage of laser pulse, usually after tens of femtosecond, II will become the dominant process due to its higher energy absorption efficiency. When the laser intensity is further higher, tunneling ionization (TI) can be introduced, in which the bandgap or potential barrier can be distorted significantly to facilitate the ionization from VBE to CBE. TI is essentially similar to MPI, referring to interaction between VBE and multiple photons simultaneously.

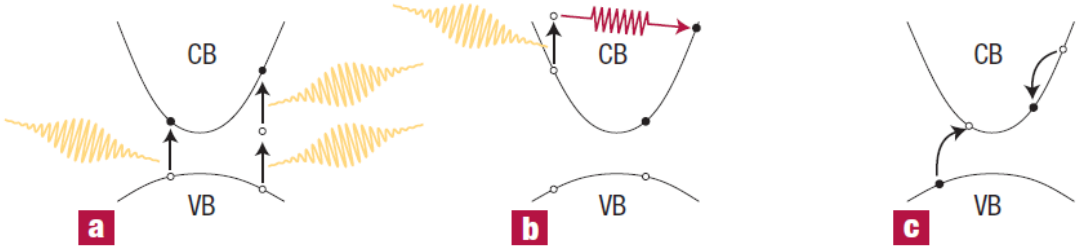

Figure 1.8 Electron excitation process laser-induced excitation of dielectric materials (a) multiphoton ionization, (b) free-carrier absorption, and (c) impact ionization [11].

1.4 Numerical modeling for ultrafast laser-material interaction

Ultrafast laser-matter interaction is a highly complicated process and involving multiple physics, which cannot be fully understood through experiments. In addition, experiments are limited by available experimental techniques and high costs. Alternatively, numerical modeling is a great tool to understand the underlying physics. Numerous theoretical works have been devoted to the study of ultrafast laser-material interaction,

from continuum scale to atomic scale, focusing on different mechanisms under different conditions.

1.4.1 Two-temperature model

Among the numerical methods for ultrafast laser-material interaction, two-temperature model (TTM) has been most widely used to describe laser energy absorption in the material and the energy transportation within the material. Due to the much shorter laser-matter interaction time than the thermal relaxation (tens of ps) between electron and lattice, two nonlinear differential equations are coupled to describe the temperature evolution in electron and lattice and the energy transfer between two systems. The initial form of TTM was proposed by [12], which does not consider the thermal non-equilibrium state in electron upon rapid laser energy deposition. This makes TTM being not suitable for ultrafast laser pulse shorter than 100 fs. To remedy this issue, a hyperbolic TTM has been developed in [13,14], which can be applied for shorter pulse within 100 fs. Phase transition has been further included in [15] to describe the dynamics of solid-liquid interface during ultrafast laser melting and ablation. To consider the dynamic removal of ablated material, the dynamics of material ejection has been incorporated in TTM as well [15]. Further improvement was introduced in [16] to consider the effects of non-equilibrium electron transport and electron drifting in TTM. TTM has high computational efficiency and sufficient capability in capturing the major thermal processes in materials under ultrafast laser pulse irradiation. However, it cannot be used to predict non-thermal

process, material decomposition process and particle ejection dynamics, therefore, it is not suitable for studies of detailed laser-matter interaction and ablation mechanisms.

1.4.2 Hydrodynamic model

To consider plasma ejection, laser plasma interaction, and thermomechanical processes, Hydrodynamic (HD) model is a good alternative for TTM to demonstrate more comprehensive responses in the material under ultrafast laser pulse irradiation. Conservation of mass, momentum and energy are coupled to describe plasma generation, dynamics and interaction with laser pulse [17,18]. Initially, most HD models only describe the plume behavior, so electron-lattice non equilibrium, hot electron emission and resultant early stage plasma generation, which are very important for femtosecond laser ablation, have been neglected. To address this, TTM has been incorporated into HD model in [19] to consider thermal non-equilibrium of electron and lattice. Hot electron emission process and the electron transport inside the material have been further considered in HD simulation [20]. A comprehensive 2D-HD model has been developed in [21] considering photoelectric emission, hot electron emission, electron transport, early-stage plasma, and late-stage plume plasma. Compared to TTM, HD model has much higher capability in description of the plasma dynamics, however, it is still limited in the frame of continuum modeling. Meanwhile, equation of state (EOS) has to be coupled with HD model to describe the material properties in a wide range of temperature, density and pressure, so that how well the HD can perform relies on the accuracy of the EOS. Generally, during the development of EOS, many assumptions have to be made, especially for extreme

conditions (extremely high temperature and pressure). Furthermore, HD as a continuum model cannot reflect microscopic ablation processes, phase change and structural modification under laser induced shock wave. Molecular dynamics (MD) model, as atomistic simulation, can compensate the incapability from continuum modeling, and provide much more information in atomic scale regarding ablation mechanisms, phase transition, particle formation, ejection, relaxation, as well as morphology of ablation crater in different materials.

1.4.3 Molecular dynamics

Molecular dynamics (MD) simulation demonstrates thermal and non-thermal behaviors in the material under different conditions, revealing detailed behaviors in atomic scale infeasible for continuum models, including phase transition, nanoparticle formation, distribution, and trajectory. The atomistic motion is universally governed by the Newton's second law, and the atomic trajectories are predicted through integration of the equation of motion. The atomic interaction (force) is obtained through predefined interatomic potential, and no other assumptions need to be made, such as critical ablation conditions (temperature and pressure). Lattice parameters have been intrinsically represented through the lattice structure and potential, including heat capacity, thermal conductivity, elastic modulus as well as their dependence on other properties. However, MD simulation cannot be directly used to describe ultrafast laser material interaction because the electron thermal behaviors cannot be inherently predicted. To address this issue, modification has to be introduced and different methods have been attempted to study different materials and focus on different

physics. The scheme of TTM-MD combined approach has been proposed in [22]. Electron thermal responses are described in the electron equation as the original form in TTM, including laser energy absorption, electron thermal diffusion, and energy coupling with lattice. The counterpart lattice equation is replaced by the atomistic governing equation of motion. The electron-lattice thermal coupling is represented by external force in the motion equation. Alternatively, electron-lattice energy transfer can be introduced through velocity rescaling in atoms, so that lattice heating can be achieved through direct velocity scaling not from the acceleration by adding external interatomic forces. Both methods satisfy the energy conservation law and have been evidenced to be equivalent to each other. To better describe the electron dynamics, Monte Carlo (MC) has been incorporated in MD simulation to study laser interaction with semiconductors and metals [23,24].

All these attempts aim to incorporate the electron behavior into classical MD simulation to investigate ultrafast laser material interaction. MD simulation is flexible in that only the knowledge of material structure and interatomic potential are required to conduct the simulation, no thermal and mechanical properties need to be assumed. However, in order to improve the suitability of interatomic potential to specific physical and chemical phenomena, comprehensive validation and comparison should be performed before the final selection of interatomic potential.

1.4.4 Plasma model

Material ablation and plasma thermodynamics can be described with TTM, HD, and MD, however, during ultrafast laser pulse interaction with semiconductor and

dielectrics, electronic dynamics has to be introduced to account for electron excitation and transportation. Several numerical approaches have been attempted to describe electronic dynamics. Single rate equation (SRE) has been derived from Fokker-Planck equation by [25] and used widely to describe ultrafast laser excitation and ablation in dielectric material. Photoionization and impact ionization have been considered as the dominant mechanisms during CBE excitation. An exponential decay term [26,27] has been further considered to represent the relaxation of CBE through self-trapping and recombination, and the life time of CBE has been determined as the pulse delay time beyond which no reduction of the optical breakdown threshold can be observed under double-pulse irradiation. Electronic transportation and energy diffusion [28] have been proposed to be influential for energy redistribution inside the material. The SRE has been doubted to be oversimplified in that impact ionization is only considered to be proportional to the number density of CBE, and the role of kinetic energy on the ionization rate has been neglected. Seeding electrons with low kinetic energy are generated by photoionization, and the occurrence of impact ionization requires sufficient electron kinetic energy gained through intra-band absorption, and this progressive absorption process has been assumed as an instant process in SRE.

Multiple rate equation (MRE) consisting a couple of rate equations were further developed in [29,30] to account for distribution of electrons on discrete energy levels in the conduction band (CB), and particle transportation on different energy levels. As shown in Figure 1.9, electrons on the bottom level of energy in the CB will be first generated through photoionization, and electrons at low energy levels will absorb photon energy to jump to higher energy levels. With sequential photon energy absorption, sufficient kinetic

energy over the bandgap can be obtained by the electron and able to trigger the impact ionization. With the excitation of another CBE from the valence band (VB), both electrons will fall back to the bottom level of CB and process to next impact ionization cycle. The MRE has been further improved in [31] by incorporating laser beam propagation inside the material. The originally simplified one photon sequential intra-band absorption has been replaced by Drude plasma absorption to enhance the capability of MRE in description of dielectric material ablation at various laser wavelengths, pulse durations and bandgaps.

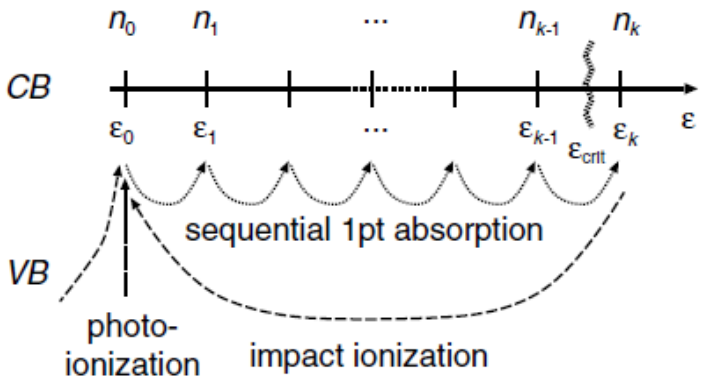

Figure 1.9 Illustration of the processes providing changes in the density and the energy, respectively, of free electrons in the conduction band of a dielectric [29,30].

Despite these improvements, plasma model itself is still limited in the description of laser ablation in dielectric materials. First, plasma model generally relies on the number density of electrons to describe the material modification, where a critical number density is usually assumed to determine the breakdown of material and no thermal behavior has been considered for electrons in thermal ablation processes. Second, plasma model only demonstrates the electron behavior and neglect the lattice behavior, where material decomposition and ejection mainly happen. Therefore, plasma model should be further

combined with a thermal model. Among the aforementioned models, TTM is computationally efficient and has sufficient capability to describe thermal behavior during laser material interaction. This combined model has been presented in [32,33] and temperature-based criteria have been employed to capture the material decomposition in dielectric materials.

1.5 Ultrafast laser micromachining of dielectric materials

The industrial demand for processing dielectric materials is increasing rapidly, such as the cutting, drilling, and marking of glass, diamond, sapphire, etc. However, processing dielectric materials is challenging for traditional manufacturing methods due to the material's high brittleness and hardness. Specifically, for microchannel fabrication, there will be inevitable cracks and high side-wall roughness with mechanical drilling. In addition, the minimum channel size is determined by the mechanical tools and the reduction of tool size to micro-level remains demanding. Furthermore, the stability of mechanical processing is difficult to guarantee due to the hard contact between samples and tools.

It is also very difficult for long-pulse laser processing because of the transparency of dielectric materials in the visible and near-infrared wavelength range. Nonlinear absorption is required to excite free electrons inside the material, however, the ultrahigh laser intensity required for nonlinear absorption is not easy to achieve by long-pulse lasers.

Ultrafast lasers have high enough laser intensity to trigger multiphoton ionization, which enables the processing of dielectric materials even with long wavelength. Due to its advantages in small heat affected zone, high precision, and high flexibility, it has great

potential in high-precision micromachining of dielectric materials, such as the fabrication of micro-fluidic devices [34], waveguides [35], micro-sensors [36], etc.

1.5.1 Hybrid processing

Numerous efforts have been devoted to the application of hybrid processing. A widely used method is the femtosecond laser irradiation and chemical etching (FLICE). FLICE combines permanent structural modification in silica glass with laser pulses irradiation and chemical etching of the irradiated material using hydrofluoric acid (HF) or KOH solutions [37–39]. This method is based on the selectivity of the chemical etching process on laser-treated region, so that the irradiated material will be removed with much higher rates than other material. Extensive experimental studies have been conducted on the implementation and improvement of material processing in this regard.

Several studies [40–42] performed three-dimensional microfabrication in silica glass with the two-step laser-assisted etching process, which allows 3D structures fabrication inside silica glass with microscale size, high aspect ratio and great flexibility. Hybrid fabrication of glass has been applied [37,43] for the integration of microchannels and waveguides for functionality such as biophotonic sensors. The etching rate of silica has been demonstrated [44] to have correlation to the morphology of the laser modified regions. Efficient etching of microstructures cannot be obtained without the formation of self-ordered (linear polarization) and disordered (circular polarization) nanostructures [44]. It has been evidenced in [38] that KOH has better selectivity over HF to elongate the microchannels in fused silica. The chemical etching process has been further improved [39]

by combining two etching agents, HF and KOH, taking advantage of the high etching rate of HF and high selectivity of KOH. This method has been proposed to improve the capability of FLICE in fabricating complicated microstructures that are infeasible by using single-agent etching. Pulse shaping has been applied [45] to improve the controllability of the structures. The etching rate using double-pulse irradiation (energy ratio 1:1) is 37 times higher than single pulse at the same total energy.

The fabrication of microstructures in silica glass using FLICE has advantages, such as high channel aspect ratios, great structural complexity and well-controlled structure quality. However, several disadvantages should be considered. The chemical etching process could take a long time (several hours), which significantly reduces the overall processing speeds and efficiency. Meanwhile, the selective etching process cannot be fully maintained because the unmodified material is also soluble in the etching solution. Furthermore, the chemical etching solutions are harmful for human health and environment due to their toxicity and corrosivity.

1.5.2 Direct processing

More recently, direct laser drilling of glass without post processing has been widely investigated and proposed in pursuit of high-speed processing in silica glass. Several key factors should be controlled during the drilling process, namely, drilling geometry, operation environment, and laser conditions, which includes but not limited to laser pulse durations, pulse energy, wavelengths, repetition rates, beam spatial and temporal

distributions, etc. The influence of these factors on the resultant microchannel drilling are provided as follows.

1.5.2.1 Drilling geometry

Due to the transparency of silica glass and highly localized structural modification under nonlinear laser absorption, the machining of glass is not limited to exterior-to-interior processes, therefore allowing for more flexible geometries and complicated internal structures.

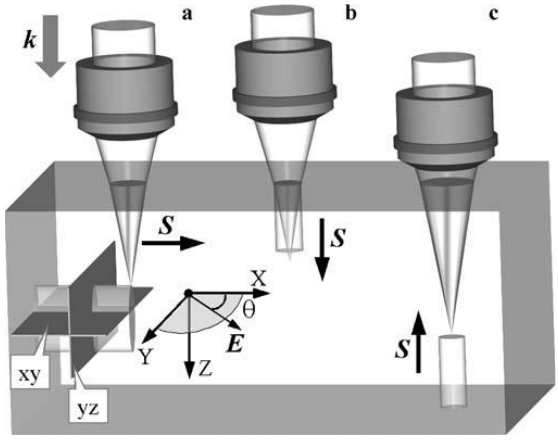

Figure 1.10 Schematic diagram of the femtosecond laser-induced modification in glass samples, (a) transverse writing geometry, (b) top-to-bottom writing geometry, and (c) bottom-to-top writing geometry [44].

As shown in Figure 1.10, the general geometries of laser modification inside glass include transverse writing with focused beam inside material, downwards writing with focused beam on the front surface, and upwards writing with focused beam on the back surface. Transverse writing is particularly useful for waveguide writing inside glass, however, not feasible for drilling process due to the noncircular cross section on the focal

spot. Upwards drilling from the back surface has been proposed to increase the length and structural quality of the drilled channels. Compared with drilling from the front surface, machining from the rear surface can eliminate the shape effects of front surface ablation, where the laser energy deposition and distribution on the material surface can be significantly affected by material ablation from preceding laser pulses. In addition, drilling from the rear surface helps to weaken the interaction between laser pulse and the formation of early plasma, which could be relatively strong due to hot electron emission and ionization of air in normal atmosphere condition. In some most recent studies [46–49] working on laser drilling in silica glass, rear-surface drilling has been more frequently used than front-side drilling, in pursuit of high aspect-ratio of the microchannel in glass.

There are still limitations on application of rear-surface drilling. It has been argued in [50] that this method is not applicable to multilayer samples or samples with non-transparent interlayer. Also, the thickness of samples cannot exceed the working distance of the focusing objective. However, as the microchannel drilling is for transparent silica glass, and the normal length of drilling is within several millimeters, the application of rear-surface drilling in silica glass should not be challenged.

1.5.2.2 Operation environment

In general, ultrafast laser ablation of materials can be conducted in air or vacuum conditions. For drilling, particularly from the rear surface, it has been proposed that immersing the rear surface in distilled water can help to minimize the blocking and

redeposition of ablation materials. Different operation environments for laser drilling have been compared in previous experimental works.

X. Zhao and Y. C. Shin [49] comprehensively studied femtosecond laser drilling in fused silica from rear surface in air and water. The advantage of drilling from rear surface is that the generated early plasma is much weaker than from the front surface, so the expansion of the plume plasma is less impeded by the early plasma formation. For drilling in air, higher pulse energy results in the increase of the channel depth and diameter. With the increase of pulse energy, the thermal effects are more pronounced than relatively low pulse energy, so that microcracks can be more noticeable around the channel. The increase of side wall roughness can be also observed, mainly due to the redeposition of material ejection when the channel became deeper. On the contrary, for drilling in water, the channel depth drops dramatically with increase of pulse energy. The reduction of drilling in water is mainly due to strong water ionization with the increase of laser pulse energy. The dense plasma in water will impede the expansion of plume plasma as well as the water flow inside the channels. Meanwhile, drilling in water will help to increase the smoothness of the side walls, because particles can be more dissolved in water instead of being redeposited onto the side walls.

B. Xia *et al*. [51] investigated the superiority of vacuum condition in the ultradeep microchannel drilling in PMMA. Efficient energy propagation with the absence of air ionization and easy ejection of ablation particles are demonstrated in vacuum drilling process. The vacuum condition helps to extend the depth of the channel (Figure 1.11 (a)) while maintaining similar channel diameter with increasing pulse number. Saturation has

been observed in both aspect ratios and channel depths with increasing pulse energy and ambient pressure, respectively. From Figure 1.11 (b) and (c), bending at the end of drilled channel can be observed only in air, which could be attributed to the unstable formation of filament in air condition as well as the interference of the laser beam propagation by the scattering and deflection of the nanoparticle ejection trapped inside the drilled channel.

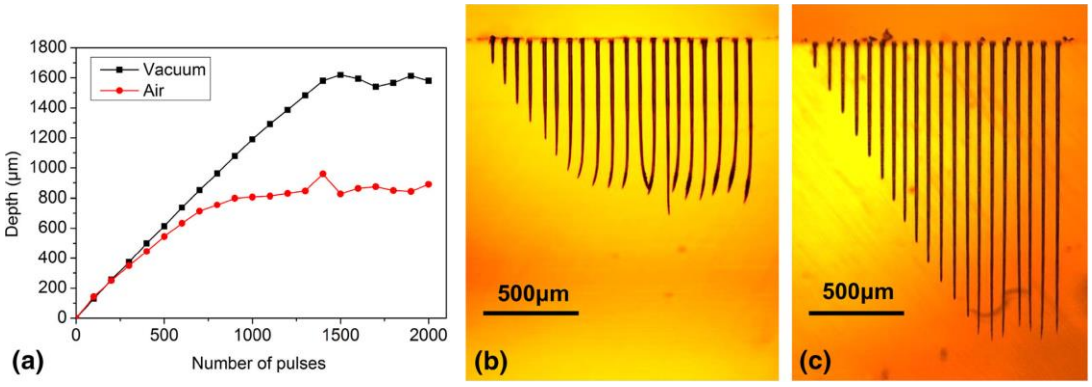

Figure 1.11 Development of (a) micro channel depth with the pulse number, and micro channel shape (b) in air and (c) in vacuum [51].

1.5.2.3 Laser conditions

L. Jiang *et al.* [52] studied the influential factors on laser induced microchannel drilling in air, including wavelengths (680nm-800nm), pulse energy, and pulse number, as shown in Figure 1.12. The increase of channel depths and aspect ratios with shorter wavelength is attributed to higher density of seeding carriers from MPI. With the increase of pulse energy, the channel depth increases monotonously until certain saturation value, while the aspect ratio experiences a peak and then decreases due to the increased channel diameter. Double pulse ablation displays its superiority in laser drilling with enhanced

channel depths at a pulse delay of 200fs. A proper range of 100-300 fs helps to raise the channel depth as well as the aspect ratio to 1.3-1.4 times higher.

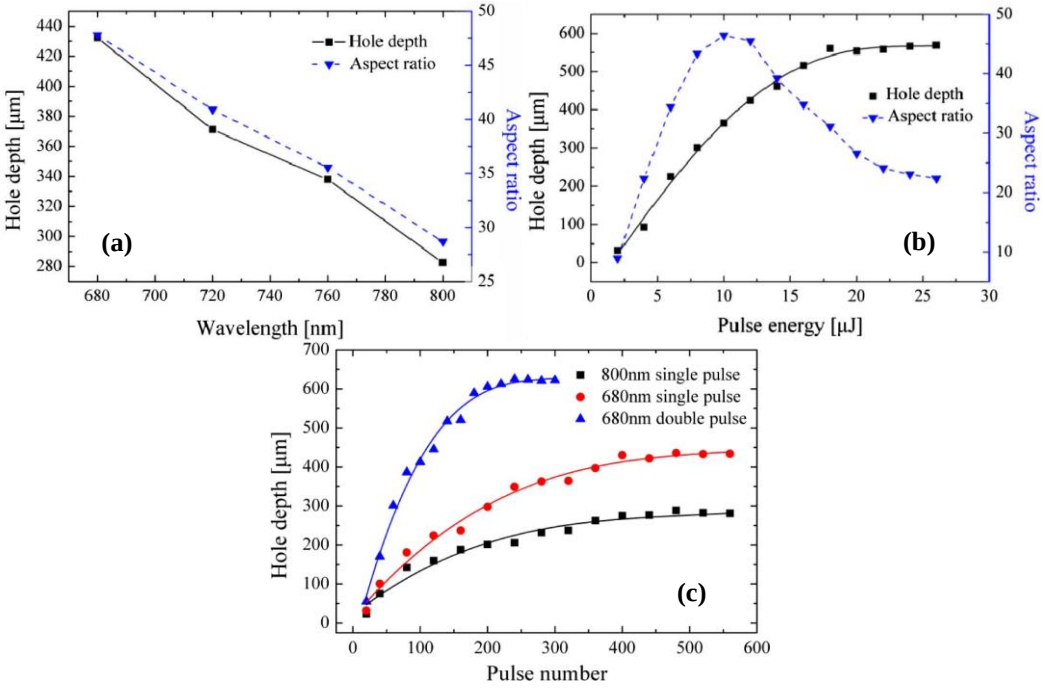

Figure 1.12 Channel depth and aspect ratio as a function of (a) laser wavelength, (b) pulse energy, and (c) pulse number [52].

S. Karimelahi, L. Abolghasemi, and P. R. Herman [47] reported rapid fabrication of microchannels in silica glass with Gaussian beam in IR and green light at varying scan speeds and repetition rates. Figure 1.13 shows top and side view images of laser modification formed for the case of rear-surface drilling at various scan speeds, and repetition rates for both IR and green wavelengths at similar pulse energy. For IR lasers, channels can be drilled through the 1 mm thickness at all the scan speeds (10-100 μm/s) at 200 kHz, while for 400 kHz the channel depths are shortened and broken into segments varying in hundreds of microns. As for 1 MHz, only random and non-uniform shaped

channels can be generated and there are cracks around the channel entrance. The major reason for this deterioration should be attributed to stronger thermal accumulation with shortened pulse interval at high repetition rates, which can be evidenced by the formation of large heat affected zone (HAZ) surrounding the channel entrance and molten material within the channel to discontinue the channel tracks. For green lasers, uniform drilling channels can be observed for 200 kHz, and better channels than IR lasers can be drilled at 400 kHz. For 1 MHz, however, due to the enhanced thermal accumulation effect, the formation of HAZ impedes the formation of straight and uniform channels drilled in the material.

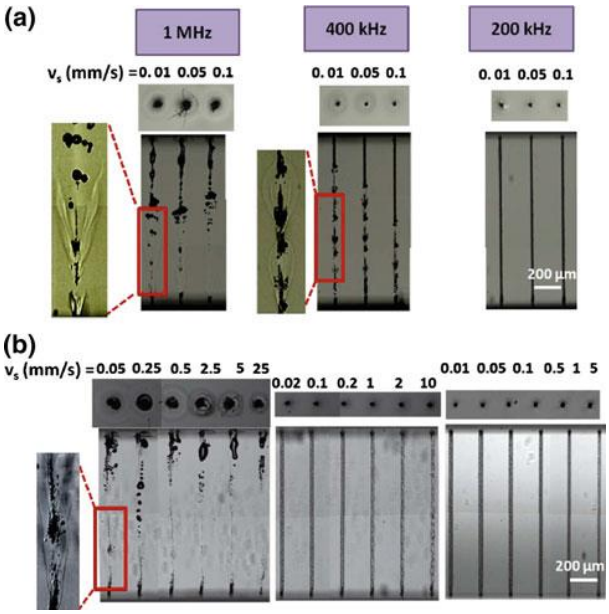

Figure 1.13 Optical microscope images of top and side views of laser ablation tracks formed by the dynamics focal scanning in the up direction at the indicated scanning velocities (v_s) and laser repetition rates from 200 kHz to 1 MHz for pulse energies of (a) 13 µJ at 1064 nm and (b) 12 µJ at 532 nm. The inset images show stronger HAZ formation effects with increasing repetition rate [47].

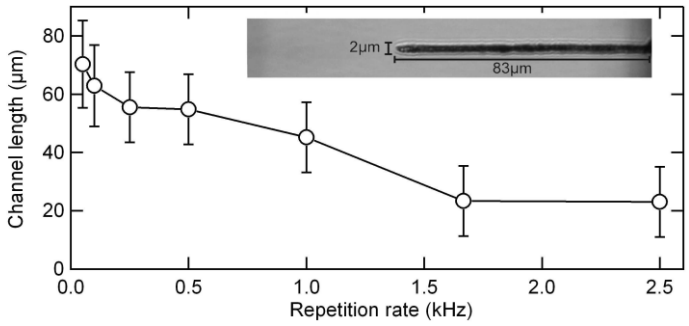

Figure 1.14 Dependence of channel length on repetition rate fabricated with Bessel beam laser pulses [53].

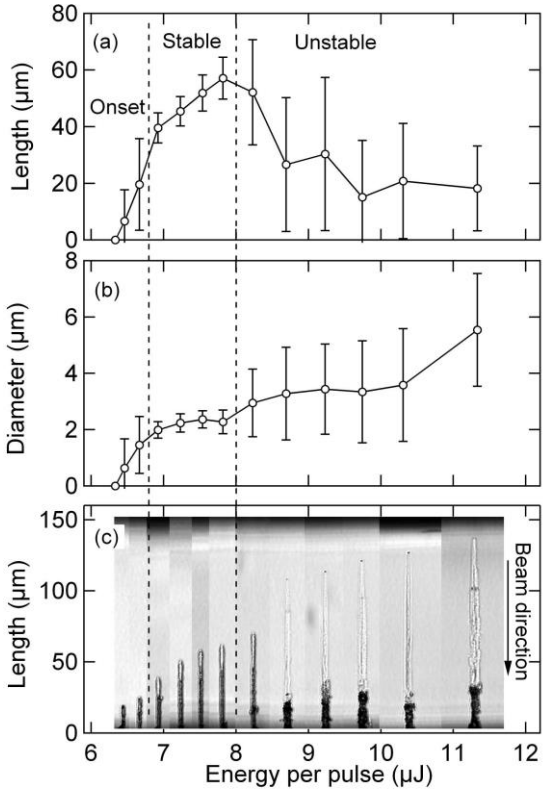

Figure 1.15 Variation of (a) channel length, (b) mean channel diameter and (c) microscopy images of typical structures as a function of pulse energy at repetition rate of 100 Hz [53].

With higher pulse energy, the thermal accumulation effect can be more pronounced, and the less smooth side walls around the channel can be generated, as observed in [49]. Therefore, lower pulse energy is preferable with increasing repetition rates to alleviate high energy deposition.

M. K. Bhuyan *et al.* [53] used Bessel beams to study the influence of laser pulse energy and repetition rates on microchannel drilling in silica glass. The influence of laser repetition rates can be observed in Figure 1.14. The channel length deceases from ~70 μm to ~20 μm while maintaining stable channel diameter when repetition rates are increased from 50 Hz to 2.5 kHz. This observation indicates the impedance of efficient material removal by reduced time between successive laser pulses. As for the influence of pulse energy shown in Figure 1.15, the diameter increases continuously with higher pulse energy, while the channel length only increases until 8 μJ and starts to decrease with further increase of pulse energy. Compared with [47], lower pulse energy and much lower repetition rates can be used for Bessel beams to achieve stable and well-controlled channel drilling in glass [53].

1.5.2.4 Pulse shaping

Typically, laser beams have Gaussian shapes in the spatial distribution, and an ellipsoidal focal volume can be obtained when focused by a lens (Figure 1.16 (a)). The axial confocal length is determined by the focusing geometry (numerical aperture) known as the Rayleigh length. Bessel beam, referred to the non-diffracting beam, can be obtained through beam spatial shaping by an axicon. The intersection angle between the conical

wave and the optical axis, denoted as alpha in Figure 1.16 (b), characterizes the length of Bessel beam. The confocal length with Bessel beam can be greatly increased compared to Gaussian beam. Based on this feature, using Bessel beam has been proposed to enable high-throughput and high-aspect-ratio microchannel fabrication in silica for applications of microfluidic devices and biosensors.

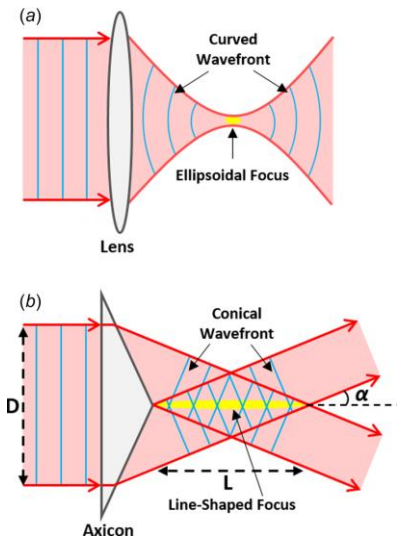

Figure 1.16 Comparison of focusing geometry and intensity distribution between (a) Gaussian and (b) Bessel beams [54].

Several studies [50,53,55,56] used Bessel beams to fabricate high-aspect-ratio microchannels in silica glass. Z. Wang *et al.* [57] manipulated the laser pulses through temporal and spatial shaping with double-pulse Bessel beam. FLICE method has been also applied to improve the length and aspect ratio of the channels. The etching depth can be enhanced by 13 times at the optimal pulse delay between double pulses, while the depth only doubles by increasing the pulse number from1 to 2000, as shown in Figure 1.17. The maximum aspect ratio of microchannel using double pulses reaches about 23:1, which is

around ten times of that with single pulse. The different structural changes induced by single and double pulse can be attributed to the localized control of electron dynamics by the temporally shaped femtosecond laser Bessel beams.

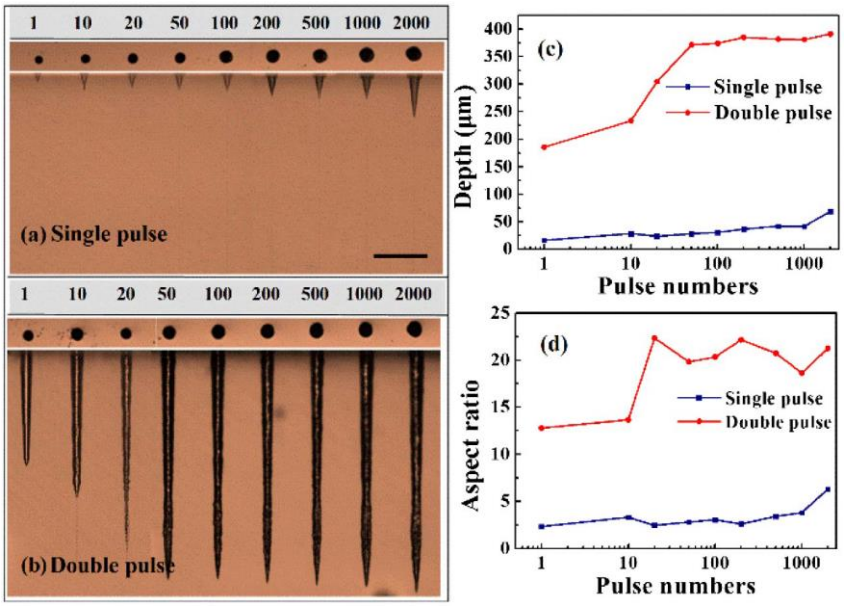

Figure 1.17 Optical transmission microscopy images of microchannel morphology evolution after etching by using Bessel beam pulses pre-irradiation at various pulse number and pulse energy of 20 μJ for (a) single pulse and (b) double pulse train with pulse delay of 10 ps, (c) channel depth and (d) aspect ratio [57].

Double-pulse drilling has been mentioned above and the superiority to single pulse has been demonstrated in [48,57]. Bessel beam can be categorized in spatial shaping of laser beam and double pulse method can be classified as temporal shaping of laser beam. The aforementioned double-pulse method mainly relies on the temporal separation of single pulse into two branches with similar features (wavelengths and pulse durations).

There are some other experimental attempts regarding temporal manipulation of laser interaction with silica glass.

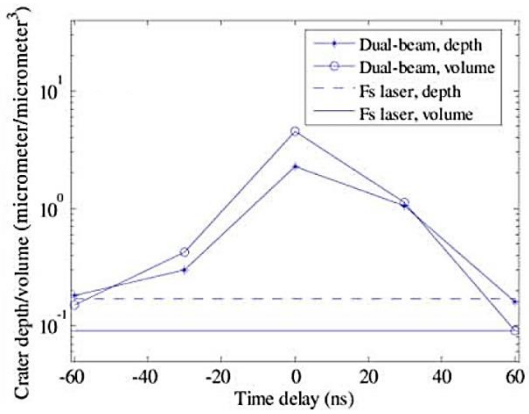

Figure 1.18 Experimental results of crater depth from different pulse manipulation with various pulse delays [58].

C. Lin *et al.* [58] investigated the micromachining of fused silica through double-pulse method combining femtosecond (120 fs, 800 nm) and nanosecond (30 ns, 355 nm) laser pulses with different delays ranging from -60 ns to +60 ns. This method is intended to improve the material removal rate through ns pulses. Femtosecond laser pulses are applied to excite the dielectric material and absorb the laser energy from ns laser pulses. The fluence of the ns pulses can be below the damage threshold. Five cases are compared with respect to different delay time, in which only the delay within 30 ns can be treated as effective. The 60 ns is too long for the ns pulse to interact with the electrons generated by the fs pulse. As shown in Figure 1.18, when ns pulse is applied before the fs pulse (negative delay time), material removal is not improved significantly, while when the two pulses are fully overlapped, maximum ablation depth can be obtained. No ablation can be seen for all

cases if the fluence of the fs pulse is reduced to be lower than the threshold, no matter how high the fluence of the ns pulse is (within the studied range).

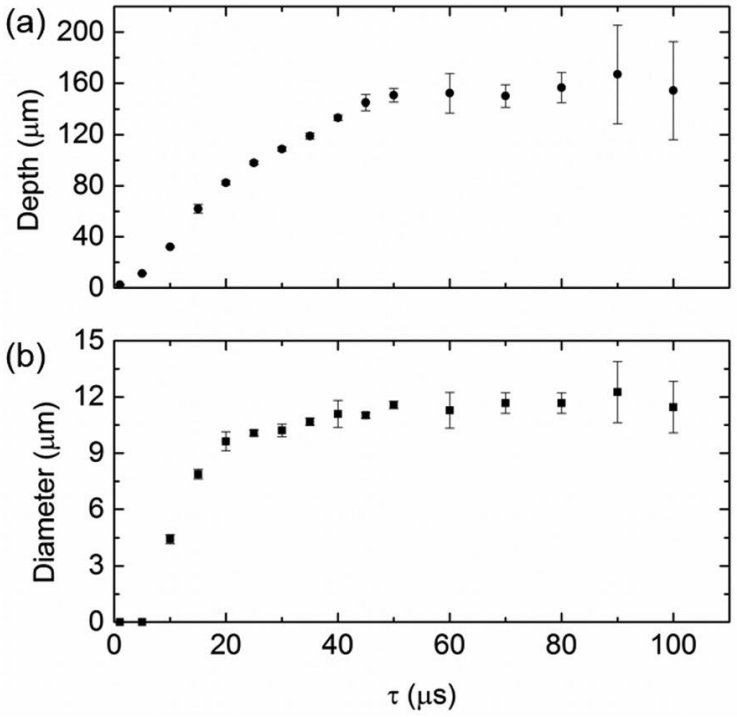

Figure 1.19 Dependence of (a) depth and (b) diameter of drilled channels on the time interval between femtosecond laser pulse and fiber laser [59].

Y. Ito *et al.* [59] proposed the combination of femtosecond laser pulses (210 fs) and fiber laser pulses (105 μs) to drill glass from the front surface. The long-pulse laser is applied after a single shot of femtosecond laser pulse. The efficiency of this method can be as high as 5000 times higher than femtosecond laser drilling. Also, the damage and micro-cracks around the channel in femtosecond laser drilling can be eliminated due to much weaker shock waves. As shown in Figure 1.19, the depth and diameter of the channel increases as the pulse delay increases, and saturated at 50 μs and 20 μs, respectively. This saturation of depth can be attributed to thermal diffusion after femtosecond laser pulse

irradiation, and dissipation of filament, which can be completed in the time scale of 100 μs. Similarly, without pre-irradiation of femtosecond laser pulses, the long-pulse laser cannot induce noticeable modification in the material. However, in pursuit of the drilling efficiency, without repeated laser pulse irradiation, the final length of the drilled channels would not be very long, and the channels are generally tapered.

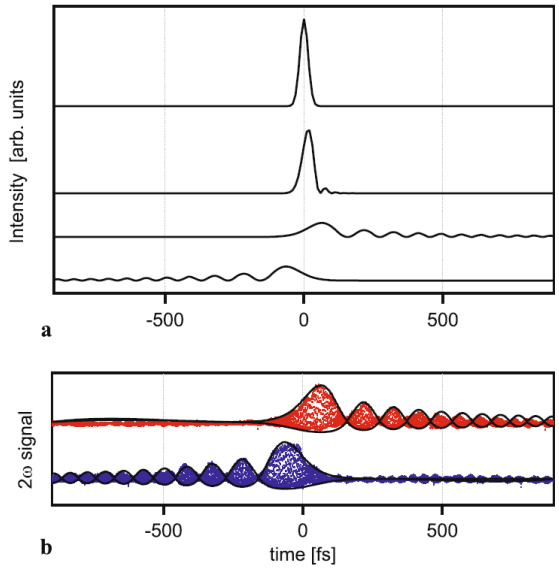

Figure 1.20 (a) Calculated temporal intensity envelopes of pulses for different third order dispersions, 0 fs^3, $25\times10^3 fs^3$, 6×10^5 fs^3, and -6×10^5 fs^3, and (b) cross correlations of unmodulated and modulated pulses, black lines: calculated envelope [60].

L. Englert et al. [60,61] employed temporally asymmetric femtosecond laser pulses in material processing. This method is proposed to decouple and control photon and impact ionization in time. Third-order dispersion, which depends on both the direction and the magnitude, is introduced for phase modulation, as shown in Figure 1.20. Positive (negative) phase modulation makes high-intensity part arrives before (after) low-intensity part and

higher phase change makes the pulse shape distort more. The modulated pulse helps to reduce the channel diameter significantly, as shown in Figure 1.21 (a).

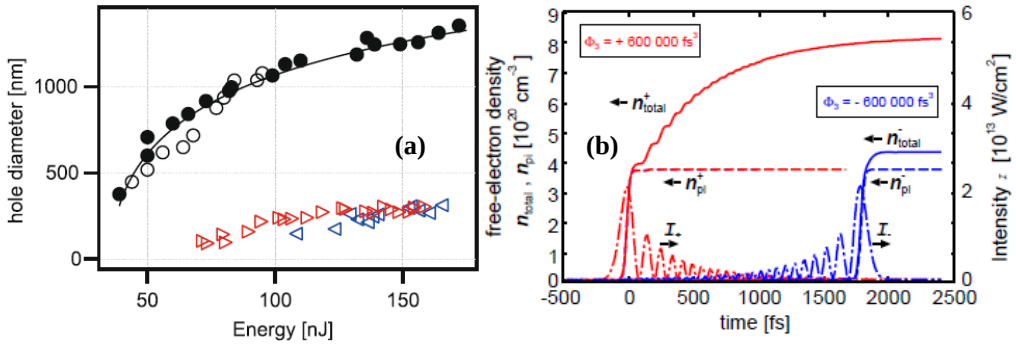

Figure 1.21 (a) Diameters of ablation structures for fused silica at zero (dot), positive (red right triangular) and negative (blue left triangular) modulated pulses and (b) transient free electron density at positive and negative modulated pulses [61].

These observations can be explained through the decoupled ionization from photoionization and impact ionization processes. As confirmed in Figure 1.21 (b), the high intensity at the head of the shaped pulse with positive phase changes excited free electrons through multiphoton ionization (MPI). The following low-intensity part is still able to further heat the material and facilitate impact ionization, therefore achieve large number density until the pulse end. By contrast, if negative phase changes are applied, the leading low-intensity part cannot be efficiently absorbed by the material and the generation of free electrons is dominated by the MPI at the pulse tail. For both cases, the initial excited electrons are highly localized due to MPI, so that the ablation diameters are much smaller.

In summary, numerous improvements have been proposed for the drilling of silica. In general, rear-surface drilling is superior to front-surface drilling due to weaker early plasma shielding and easier expansion of plume plasma. Vacuum condition is better than

air condition with absence of air ionization and impedance on plasma ejection. Water can facilitate dissolving of ablated material and enhance ultimate drilling length only at relatively low laser fluence, but becomes worse than air for high pulse energy. Ultrafast pulse laser drilling at relatively low pulse energy is preferable for high quality drilling with less heat affected zones and weaker shock waves. The interior structure can be also deteriorated by increasing repetition rates due to enhanced energy deposition and impedance on the material ejection from the channel. Optimal drilling process can be obtained at moderate scan speeds. Bessel beams with much longer confocal length can shorten the time of material processing, however, the pulse energy for Bessel beam is much higher than Gaussian beam due to the spatially more uniform energy distribution in longer path. Combination of two pulses with same or different pulse duration can significantly increase the material removal efficiency based on control of the electron dynamics during laser material interaction, however, the experimental setup for double-pulse irradiation or phase modulation is more complicated. The advantages of different methods can be combined to satisfy various demands in industrial and research applications.

1.6 Research Objectives

The main objective of this research is to understand the dominating physical mechanisms during ultrafast laser pulse interaction with dielectric materials and the micro-drilling process. Material decomposition mechanisms and plasma dynamics will be studied through numerical simulations and experiments. Based on the understanding of laser-

material interaction processes, micro drilling of fused silica will be investigated. The specific objectives include:

1. Investigation of material decomposition mechanisms, thermal and non-thermal ablation processes, laser-induced structural deformation: molecular dynamics simulation will be performed incorporating plasma model and two-temperature model to study the material decomposition processes and analyze the structural deformation under laser-induced shock waves.

2. Investigation of dielectric material excitation, thermal relaxation and ablation processes under ultrafast laser pulse irradiation: a plasma model will be combined with two-temperature model to understand the electronic and thermal processes in dielectric materials and study the ablation rates at different laser conditions.

3. Investigation of material plume plasma dynamics, including nanoparticle generation, evolution, expansion, and distribution at the irradiation of ultrafast laser pulses: molecular dynamics simulation and time-resolved measurements of plasma dynamics will be carried out.

4. Investigation of ultrafast laser micromachining process in dielectric materials: micro-drilling process will be studied at different laser conditions and the fundamental mechanisms for laser-based drilling will be investigated.

1.7 Thesis Outline

Chapter 1 presents the background and motivation, literature review on ablation mechanisms, modeling methods, laser-based micromachining of dielectric materials, and research objectives.

Chapter 2 introduces the experimental setups and measurement methods in this study. Shadowgraph imaging is applied for measurement of plume plasma dynamics during dielectric material surface ablation and drilling process.

Chapter 3 provides the details of numerical modeling in this research. A single rate equation is used in the plasma model to describe the electronic excitation, and relaxation processes. Two-temperature model describes the temperature evolution and energy transfer in electron and lattice. Molecular dynamics simulation demonstrates thermal, mechanical and structural responses inside the material. Combination of these models will provide comprehensive description of dominant physical processes in material decomposition and plasma evolution.

Chapter 4 illustrates the dominating ablation mechanisms with molecular dynamics simulation incorporated with two-temperature model and plasma model. Thermal and mechanical ablation mechanisms are investigated in metal and dielectrics. The critical conditions for the occurrence of phase explosion and spallation are determined and the ablation criteria are proposed accordingly. Plasma dynamics is comprehensively studied based on simulations and time-resolved fluorescence and shadowgraph imaging of laser-induced plasma.

Chapter 5 characterizes the variation of ablation depth at different laser pulse energy, pulse durations, focusing geometry, pulse numbers and repetition rates. Plasma model is combined with two-temperature model to account for the dominant mechanisms during ultrafast laser pulse interaction with dielectric materials.

Chapter 6 demonstrates microchannel drilling by ultrafast laser at different laser pulse energy and drilling speeds and studies their impacts on channel length, diameter, aspect ratio, geometry, and side-wall quality. Beam propagation model is developed to describe the drilling process and the dominating mechanism of channel self-termination is proposed and validated.

Chapter 7 summarizes the conclusions of this study and future works.

CHAPTER TWO

EXPERIMENTAL METHODS

This chapter presents the setups for different experiments, including femtosecond laser ablation of fused silica, femtosecond laser drilling of fused silica, and fluorescence/shadowgraph imaging of plasma dynamics for surface ablation.

2.1 Ultrafast laser ablation

The schematic of the experimental setup for femtosecond laser ablation of fused silica is shown in Figure 2.1.

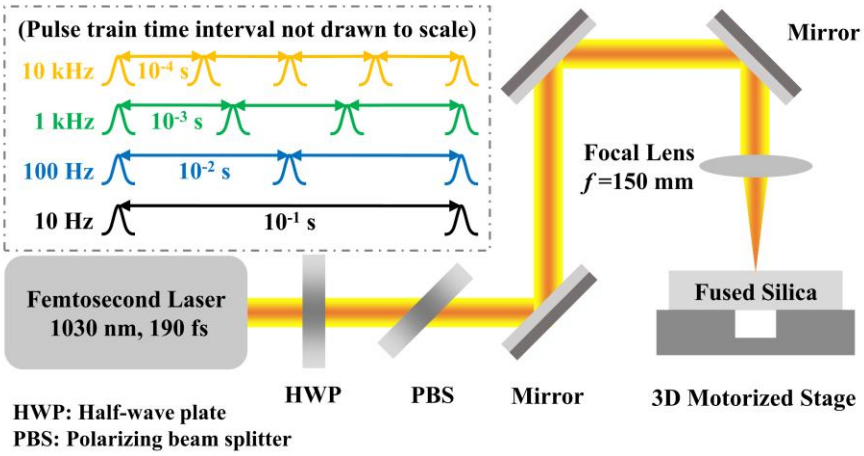

Figure 2.1 Experimental setup for femtosecond laser ablation of fused silica.

A Yb:KGW femtosecond laser source (Pharos, Light Conversion) is employed to deliver linearly polarized laser beam at the wavelength of 1030 nm and the pulse duration (full width at half maximum) of 190 fs. The laser beam is focused (f =150 mm) on the sample surface at normal incidence. The pulse energy is adjusted by a half-wave plate and a polarized beam splitter. Fused silica samples (TOSOH-ES, thickness 2 mm) are mounted

on a three-dimensional motorized stage to accurately control the position of each ablation spot. The experiments are performed in both single- and multi-pulse modes. The ablation craters are quantitatively characterized by a laser scanning confocal microscope (Olympus LEXT OLS 4000). Laser pulse repetition rate is varied in the range of 10 Hz-10 kHz (pulse time intervals of 10^{-1}-10^{-4}s) to study its influence on ablation.

2.2 Ultrafast laser drilling

The schematic of the experimental setup for femtosecond laser drilling of fused silica is essentially similar to that for ablation, as shown in Figure 2.2. The focal lens (f=150 mm) is replaced by a microscope objective (10X) with a numerical aperture of NA=0.30 to facilitate focusing the laser beam onto the sample rear surface and conducting upwards drilling process.

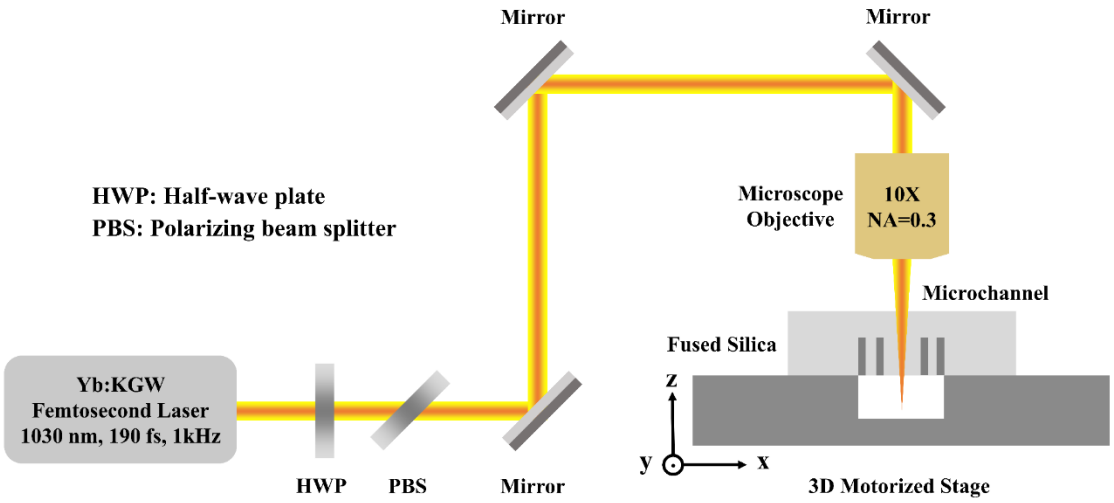

Figure 2.2 Experimental setup for femtosecond laser drilling of fused silica.

The experimental setup is schematically demonstrated in Figure 2.2. A Yb:KGW femtosecond laser source (Pharos by Light Conversion) is employed to deliver linearly

polarized laser beam at 1030 nm wavelength, 190 fs pulse duration (full width at half maximum) and 1 kilohertz (kHz) repetition rate. The incident beam radius measured at $1/e^2$ is ~2.5 mm. The pulse energy is adjusted by a half-wave plate and a polarized beam splitter. Fused silica (Corning 7980, thickness 2.5 mm) is selected as the drilling sample for its high transparency in optics applications. The channels are drilled in air, with each channel at a fresh region to avoid contamination from material redeposition. For rear-side drilling, the laser beam is initially focused beneath the rear surface (at normal incidence) by a 10X (NA=0.3) microscope objective and moved upwards until the focal spot is above the front surface. Samples are mounted on a 3D motorized stage to provide accurate control of channel position and drilling speed. After drilling, the length and diameter of the channels are measured by optical microscope from the side view. To examine the channel sidewall quality, the samples are cut through the channel cross section and characterized by a laser scanning confocal microscope (Olympus LEXT OLS 4000).

2.3 Plasma measurement

In order to measure the plasma ejection dynamics upon laser ablation in fused silica, we take fluorescence and shadowgraph images by ICMOS camera. The setup of surface ablation is essentially same as that in section 2.1. For fluorescence measurement, the fluorescence of the generated plasma is directly imaged into the ICMOS camera, as shown in Figure 2.3. For shadowgraph measurement, the reflective mirror is replaced by a beam splitter. As shown in Figure 2.4, the laser beam can be partly reflected as the pump pulse to ablate the material, and the part pass through the beam splitter will be taken as the probe

pulse. A second-harmonic generation (SHG) is used to halve the wavelength of laser beam to make the probe beam in the visible spectrum. Two mirrors mounted on a motorized translational stage are used to adjust the time interval between pump and probe beam. The generated plasma from the pump beam will be illuminated by the probe beam, and the shadowgraph will be imaged in the ICMOS camera.

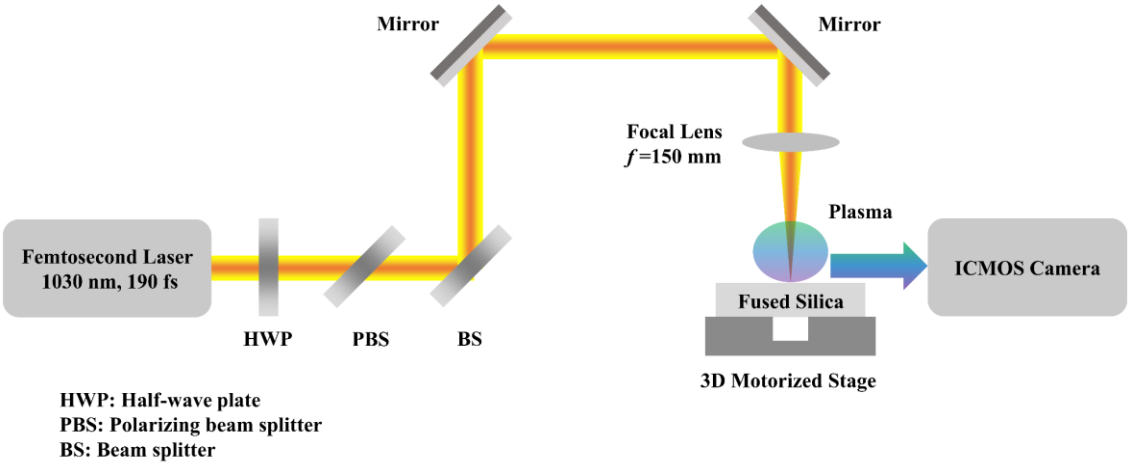

Figure 2.3 Experimental setup of fluorescence imaging of fused silica plasma.

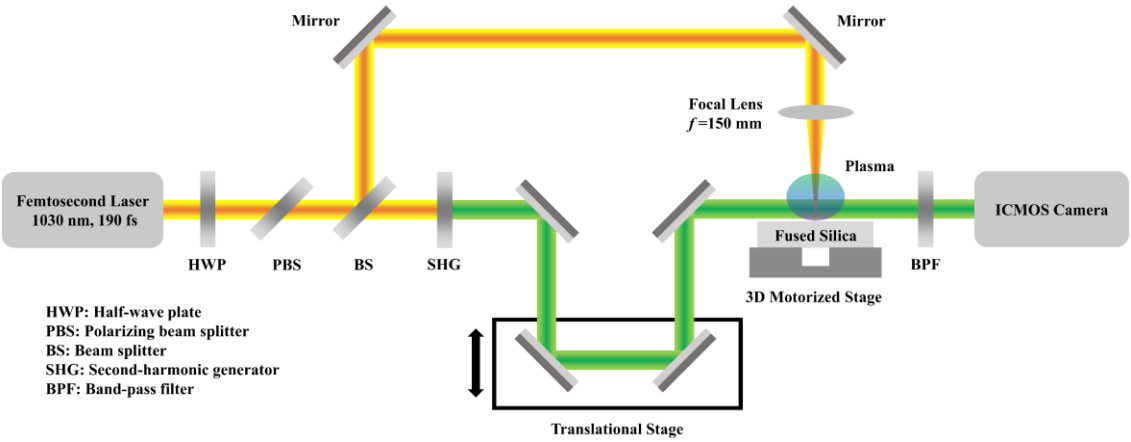

Figure 2.4 Experimental setup of shadowgraph imaging of fused silica plasma.

CHAPTER THREE

NUMERICAL MODELING

This chapter presents the numerical modeling methods in description of ultrafast laser interaction with dielectric materials. Plasma model accounts for the electronic dynamics during laser irradiation of dielectric materials, including electron photoionization, impaction ionization, and relaxation. Two-temperature model (TTM) describes the thermal responses inside the materials, incorporating laser energy absorption, energy transfer between electron and lattice, and thermal diffusion. Molecular dynamics (MD) simulation is responsible for investigation of thermal and non-thermal phenomena in atomic scale, such as ablation mechanisms, plasma generation and expansion. To study different behaviours upon ultrafast laser irradiation, these models can be combined in different approaches. Thermal and electronic processes can be captured through combination of plasma model and two temperature model. MD model can be further incorporated to investigate the material responses in atomic scale. The laser interaction with metals has been also studied, with combination of TTM and MD simulation.

3.1 Two-temperature model (TTM)

A physics-based one-dimensional numerical model has been developed to describe the dynamic process of ultrafast laser-induced ablation (ULIA) by a single pulse in vacuum, as shown in Figure 3.1 (shown in two-dimensional to better illustrate the physics). The sample surface is located at z = 0, and the incident laser radiation travels along the +z direction, perpendicularly to the material surface. The laser energy is first absorbed by free

electrons, and then transferred to the lattice through electron-phonon (lattice) coupling. When the temperature of the lattice is higher than the temperature criterion, ablation can be initiated, forming an ablated crater. Free expansion of ablated material is expected in vacuum so that material redeposition is not considered in this model. Despite the ultrafast non-thermal feature of ULIA, residual thermal energy cannot be fully eliminated so that a HAZ is formed in sub-micrometer scale. Based on this numerical model, dynamic process of ablation, dimension of the ablation crater and the HAZ can be predicted.

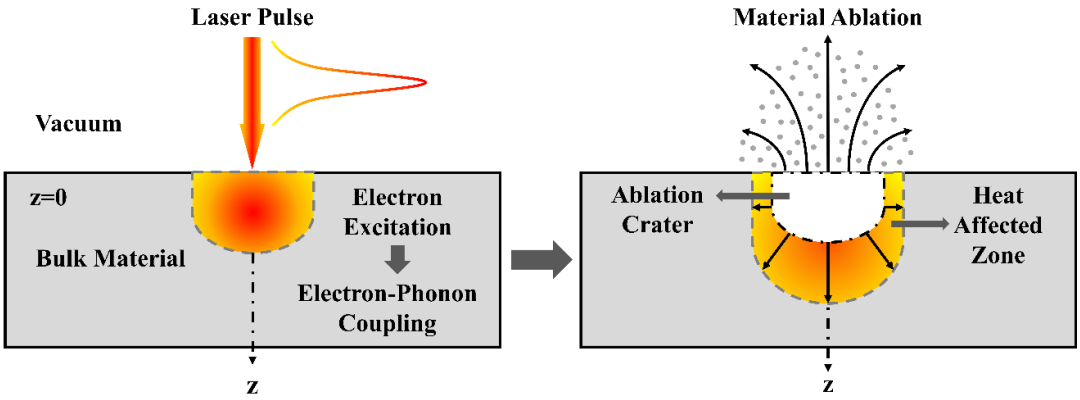

Figure 3.1 Schematic illustration of ULIA.

3.1.1 Temperature evolution

Due to the much faster thermal responses in electrons than lattices, electrons are responsible for the absorption of laser pulse energy, and the temperature can be raised up drastically to be much higher than the lattice temperature. Electron thermal energy is continuously transferred to lattice through electron-phonon coupling, and the thermal equilibrium between electron and lattice can be achieved well after the termination of laser

pulse. Two nonlinear differential equations in the TTM have been incorporated to describe the temperature evolution in electron and lattice, respectively [12],

$$\frac{\partial}{\partial t}\left(C_e T_e\right) = \nabla \cdot \left(K_e \nabla T_e\right) - G\left(T_e - T_l\right) - S \tag{3.1}$$

$$\frac{\partial}{\partial t}\left(C_l T_l\right) = \nabla \cdot \left(K_l \nabla T_l\right) + G\left(T_e - T_l\right) \tag{3.2}$$

where t is the time, G the electron-phonon coupling factor, S the laser source term, C_e/C_l and K_e/K_l the volumetric heat capacities and thermal conductivities of electron and lattice, respectively. To capture the temperature dependency of material thermal properties, the quotidian equation of state (QEOS) model [62] is adopted to calculate the volumetric energy of electron and lattice within a wide range of temperature, and the material thermal properties can be determined as $C_{e/l} = \partial E_{e/l} / \partial T_{e/l}$ and $K_e = C_e v_F^2 / \left(3\upsilon_e\right)$, where $E_{e/l}$ is the volumetric energy of electron and lattice, v_F the fermi velocity, and υ_e the electron collision frequency, predicted by the Lee-More plasma model [63]. The thermal diffusion in lattice can be neglected due to the much smaller K_l compared to K_e. The electron-phonon coupling factor G is calculated as $G = C_e / \tau_r$ [64], where τ_r is the mean energy exchange time between electron and lattice, which can be determined as $\tau_r = \left(m_i / 2m_e\right) / \upsilon_e$ [64], where m_i is the ion mass, and m_e the electron mass. The latent heat for melting and vaporization is ignored here because its contribution to temperature variation is negligible during ULIA.

3.1.2 Laser beam profile and propagation

By assuming both temporal and spatial Gaussian distribution of the pulse, the laser intensity can be described as,

$$I(t,z) = I_0(1-R)\left(\frac{w_0}{w(z)}\right)^2 \exp\left(-4\ln 2\frac{(t-2\tau_p)^2}{\tau_p^2}\right) \tag{3.3}$$

where I_0 is the incident laser intensity, R is the surface reflectivity, τ_p is the full width at half maximum (FWHM) pulse duration, w_0 is the beam waist size, and $w(z)$ is the radius of the beam spot with a distance of z from the waist given as,

$$w(z) = w_0\sqrt{1+\left(\frac{z}{z_R}\right)^2} \tag{3.4}$$

$$z_R = \frac{\pi w_0^2}{\lambda} \tag{3.5}$$

where z_R is the Rayleigh range, and λ is the laser wavelength.

Laser intensity attenuation along with penetration can be expressed differently for dielectric material and metals, with Eq. (3.6) and (3.7), respectively, in the given forms as in [18,65],

$$\frac{\partial I(t,z)}{\partial z} = -\left[\alpha + \delta_N I(t,z)^{N-1} E_g\right] I(t,z) \tag{3.6}$$

$$\frac{\partial I(t,z)}{\partial z} = -\alpha I(t,z) \tag{3.7}$$

where α is the absorption coefficient, δ_N is the cross section for multiphoton ionization with N photons, E_g is the bandgap of the dielectric material. Apart from laser energy used for electron heating, the other portion is consumed to overcome the band gap for inter-band excitation.

3.1.3 Optical properties

The optical properties of the material including the surface reflectivity and the absorption coefficient are calculated based on the Drude theory [66]. The complex dielectric function of the plasma is given as,

$$\varepsilon_r(\omega) = \varepsilon_1(\omega) + i\varepsilon_2(\omega) = 1 + (\varepsilon_g - 1)\left(1 - \frac{n_e}{n_v}\right) - \frac{\omega_p^2}{\omega^2 + i\omega/\tau_e} \tag{3.8}$$

where ε_g is the dielectric function of the unexcited material, n_v is the valence band electron density, ω is the laser frequency, τ_e is the free electron collision time, ε_1 and ε_2 are the real and imaginary parts of the complex dielectric function, respectively, and ω_p is the plasma frequency, which is given as,

$$\omega_p = \left(\frac{n_e e^2}{\varepsilon_0 m_e}\right)^{1/2} \tag{3.9}$$

where ε_0 is the vacuum permittivity, and m_e is the mass of electron.

For low electronic temperature ($T_e < T_F$, T_F is the Fermi temperature), material can be treated as solid or liquid status, the electronic collision frequency can be expressed as the sum of the electron-electron and electron-phonon collision frequencies [67],

$$\upsilon_e = \upsilon_{e-e} + \upsilon_{e-p} \tag{3.10}$$

$$\upsilon_{e-e} = \frac{A_T T_e^2}{\hbar T_F} \tag{3.11}$$

$$\upsilon_{e-p} = 2k_s \frac{e^2 k_B T_i}{\hbar^2 v_F} \tag{3.12}$$

where T_e and T_i are the temperature of electron and lattice, v_F is the Fermi velocity, A_T and k_s are constants, e is the electron charge, kB is the Boltzmann constant, $\hbar$ is the reduced Planck constant.

At high electron temperature ($T_e \gg T_F$), υ_e is approximated by the electronic collision frequency in plasma, which is the sum of electron-neutral and electron-ion collision frequencies [63,68],

$$\upsilon_e = \upsilon_{e-n} + \upsilon_{e-i} \tag{3.13}$$

$$\upsilon_{e-n} = 2\times10^{-7} n_n T_e^{1/2} \tag{3.14}$$

$$\upsilon_{e-i} = \frac{2\sqrt{2}\pi\left(Z^*\right)^2 n_e e^4 \ln\Lambda}{3\sqrt{m_e}\left(k_B T_e\right)^{3/2}\left[1+\exp\left(-\mu/k_B T\right)\right]F_{1/2}} \tag{3.15}$$

where n_n and n_e are the neutral and electron number density, Z^* is the ionization state, μ is the chemical potential, m_e is the electron mass, $F_{1/2}$ is the Fermi-Dirac integrals, $\ln\Lambda$ is the Coulomb logarithm given by,

$$\ln\Lambda = \frac{1}{2}\ln\left(1+b_{\max}^2/b_{\min}^2\right) \tag{3.16}$$

where b_{max} and b_{min} are upper and lower cutoffs on the impact parameter for Coulomb scattering, approximated as,

$$b_{\max} = \left[\frac{4\pi n_e e^2}{k_B\left(T_e^2+T_F^2\right)^{1/2}} + \frac{4\pi n_i\left(eZ^*\right)^2}{k_B T_i}\right]^{-1/2} \tag{3.17}$$

$$b_{\min} = \max\left[\frac{Z^* e^2}{k_B T_e}, \frac{\hbar}{\left(m_e k_B T_e\right)^{1/2}}\right] \tag{3.18}$$

where n_i is the ion number density.

In the transition region of electron temperature between these two regimes, the electronic collision frequency can be estimated by the harmonic mean as,

$$\upsilon_e^{-1} = \left(\upsilon_{e-e} + \upsilon_{e-p}\right)^{-1} + \left(\upsilon_{e-n} + \upsilon_{e-i}\right)^{-1} \tag{3.19}$$

In addition, an upper cutoff υ_c should be introduced to ensure greater electron mean free path than the ion sphere radius,

$$\upsilon_e < \upsilon_c = v_e / r_0 \tag{3.20}$$

where r_0 is the ion sphere radius, taken as $r_0 = \left(3/4\pi n_i\right)^{1/3}$, and v_e is the characteristic electron velocity, calculated as $v_e = \left(v_F^2 + k_B T_e / m_e\right)^{1/2}$.

Based on the real (ε_1) and imaginary (ε_2) part of the complex dielectric function, the real (n) and imaginary (κ) parts of the refractive index can be determined as,

$$n = \sqrt{\frac{\varepsilon_1 + \sqrt{\varepsilon_1^2 + \varepsilon_2^2}}{2}} \tag{3.21}$$

$$\kappa = \sqrt{\frac{-\varepsilon_1 + \sqrt{\varepsilon_1^2 + \varepsilon_2^2}}{2}} \tag{3.22}$$

The surface reflectivity R and absorption coefficient α can be further obtained from the Fresnel equations [69],

$$R = \frac{(n-1)^2 + \kappa^2}{(n+1)^2 + \kappa^2} \tag{3.23}$$

$$\alpha = \frac{2\omega\kappa}{c} \tag{3.24}$$

3.1.4 Initial and boundary conditions

The initial electron and lattice temperatures are set to be room temperature (300 K), and non-flux boundary conditions are applied due to the ultrafast period of ablation processes,

$$T_e\left(z,t=0\right)=T_l\left(z,t=0\right)=300\text{K} \tag{3.25}$$

$$\left.\frac{\partial T_{e/l}}{\partial z}\right|_{surface}=\left.\frac{\partial T_{e/l}}{\partial z}\right|_{bottom}=0 \tag{3.26}$$

The simulation domain is set to be large enough so that the description of non-flux boundary at the bottom will not be challenged.

3.2 Plasma model

Dielectric materials are initially transparent to visible and near-infrared laser due to lack of electrons in the conduction band, like metals and semiconductors. For ultrafast laser, sufficiently high laser intensity can be achieved so that the valence band electrons (VBEs) are able to be excited to the conduction band through multiphoton ionization (MPI). These ionized conduction band electrons (CBEs) will further absorb laser energy, and be able to ionize VBEs through impact ionization (II) when the kinetic energy of the CBEs is high enough to overcome the bandgap. This dual-mechanism electron excitation process will continue to increase the number density of CBEs, and the dielectric materials will behave like metallic materials when sufficient number of CBEs have been excited. Continuous heating of the CBEs and electron-phonon coupling will lead to lattice heating, breakdown,

and decomposition. The dynamics of CBE excitation and relaxation can be modeled through single-rate equation (SRE) as follows,

$$\frac{\partial n_e}{\partial t} = \left(\frac{n_v - n_e}{n_v} \right) \left[\alpha_{II} I n_e + \delta_N I^N \right] - \frac{n_e}{\tau_r} \tag{3.27}$$

where n_e is the free electron number density, n_v is the initial valence band electron number density, t is the time, α_{II} is the impact ionization coefficient and τ_r is the CBE lifetime. Free electron excitation from valence band to conduction band is considered to be dominated by the processes of MPI and II. The loss of free electrons can be resulted from self-trapping, recombination, and relaxation.

The formation of self-trapping excitons (STEs) has been considered to be an important channel for the relaxation of the excited CBEs in dielectrics, especially for fused silica, where fast self-trapping can be observed within as short as ~150 fs. The relaxation of these metastable STEs cannot be completed earlier than tens of ps, and the characteristic lifetime has been experimentally estimated as ~ 34 ps [70]. The STEs, which are situated ~ 6 eV below the conduction band, can be also re-excited to CBEs through photoionization (PI) [71–73] and II [74]. To account for the dynamics of STE, generation and degeneration (relaxation) of CBEs and STEs can be modeled through single-rate equations (SREs) as follows,

$$\frac{\partial n_e}{\partial t} = S_e - L_e \tag{3.28}$$

$$\frac{\partial n_s}{\partial t} = S_s - L_s \tag{3.29}$$

where n_e is the CBE number density, n_s is the STE number density, t is the time, S_e, L_e, S_s, and L_s are the generation and loss terms of CBE and STE, respectively, which can be determined as follows,

$$S_e = \frac{n_v - n_e - n_s}{n_v}\psi_g + \frac{n_s}{n_a}\psi_s \tag{3.30}$$

$$L_e = S_s = \frac{n_e}{\tau_r} \tag{3.31}$$

$$L_s = \frac{n_s}{n_a}\psi_s + \frac{n_s}{\tau_s} \tag{3.32}$$

where n_v is the initial valence band electron number density, n_a is the atom number density, ψ_g and ψ_s are the excitation rate of valence band electron and STE, τ_r and τ_s are the relaxation lifetime of CBE and STE, respectively.

PI and II processes have been considered as the dominant mechanisms in the ionization of dielectric materials at irradiation of ultrafast laser pulses, as well as in the re-excitation of STEs to CBEs. The excitation rate of VBE and STE can be written as follows,

$$\psi_g = \left(\psi_{PI} + n_e\psi_{II}\right)\Big|_{U_g} \tag{3.33}$$

$$\psi_s = \left(\psi_{PI} + n_s\psi_{II}\right)\Big|_{U_s} \tag{3.34}$$

where ψ_{PI}, ψ_{AI} represent the rates of photoionization and avalanche (impact) ionization, U_g, U_s are the bandgap for valence band electron and STE, respectively.

The PI is highly sensitive to laser intensity due to the nonlinear absorption (optical) process. PI has been widely simplified as the multiphoton ionization (MPI) process in the SRE, whereas the tunneling ionization (TI) process can dominate with ultrahigh laser intensity. Instead of the MPI approximation, the photoionization rate predicted by Keldysh theory [75] can be adopted to consider the transition between MPI and TI,

$$\psi_{PI} = \frac{2\omega}{9\pi}\left(\frac{\omega m^*}{\hbar\gamma_1}\right)^{3/2} Q(\gamma, x)\exp\left[-\pi\langle x+1\rangle\frac{K(\gamma_1)-E(\gamma_1)}{E(\gamma_2)}\right] \tag{3.35}$$

where ω is the laser frequency, $m^* = m_e/2$ is the electron reduced mass, $\hbar$ is the reduced Planck constant, $\gamma = \omega\sqrt{m^*U}/eE_l$ is the Keldysh parameter for the bandgap U and the laser electric field E_l, e is the electron charge, γ_1 and γ_2 are determined as $\gamma_1 = \gamma/\sqrt{1+\gamma^2}$ and $\gamma_2 = \gamma_1/\gamma$, $\langle x\rangle$ denotes the integer part of the number x, K and E are the complete elliptic integrals of the first and second kind, respectively. The function $Q(\gamma, x)$ is given as,

$$Q(\gamma, x) = \sqrt{\frac{\pi}{2K(\gamma_2)}}\sum_{n=0}^{\infty}\exp\left[-\pi n\frac{K(\gamma_1)-E(\gamma_1)}{E(\gamma_2)}\right]\cdot\Phi\left[\pi\sqrt{\frac{2\langle x+1\rangle-2x+n}{2K(\gamma_2)E(\gamma_2)}}\right] \tag{3.36}$$

where $\Phi(z) = \int_0^z \exp\left(y^2 - z^2\right)dy$, and $x = \tilde{U}/\hbar\omega$. $\tilde{U}$ is the effective bandgap, given as,

$$\tilde{U} = \frac{2U}{\pi\gamma_1}E(\gamma_2) \tag{3.37}$$

For high frequency and low intensity (electric field) laser ($\gamma \gg 1$), the photoionization based on Keldysh formulation can be reduced to the MPI approximation, whereas for low frequency and high intensity laser ($\gamma \ll 1$), the TI process turns to be the dominating process.

The generation of CBEs from photoionization (PI) process is providing seeding electrons to trigger the impact ionization (II) process when sufficient kinetic energy has been achieved by the CBEs to overcome the ionization potential, so that further CBEs can be excited from the valence band.

The II rate can be estimated as [68,74,76],

$$\psi_{II} = \int \nu_0(\varepsilon) F_e(\varepsilon)\, d\varepsilon \tag{3.38}$$

where ε is the electron energy, $F_e(\varepsilon)$ is the electron energy distribution function, and $\nu_0(\varepsilon) = \alpha_0(\varepsilon/\Delta - 1)^2$ for $\varepsilon > \Delta$, and zero for $\varepsilon < \Delta$ [76]. The rate constant α_0 is taken as 1.5 fs^{-1} for fused silica [68]. Δ represents the threshold energy for impact ionization, which is estimated as $\Delta = (1+2\mu)\tilde{U}/(1+\mu)$ [31], where μ is ratio between the electron and hole mass, taken as unity if equal mass has been assumed for electron and hole. Assuming a Fermi distribution for the electrons in the conduction band, and a density of state $g(\varepsilon) = (1/2\pi^2)(2m_e/\hbar^2)^{3/2}\sqrt{\varepsilon}$, the electron energy distribution function is given as [74],

$$F_e(\varepsilon) = \frac{3}{2}\left(\frac{\varepsilon}{E_F^3}\right)^{1/2} f_F(\varepsilon) \tag{3.39}$$

where $f_F(\varepsilon)$ is the Fermi distribution function, and E_F is the Fermi energy,

$$E_F = \frac{\hbar^2 (3\pi^2 n_e)^{2/3}}{2m_e} \tag{3.40}$$

3.3 Molecular dynamics

3.3.1 Governing equations

In MD model, the atomic motion is universally governed by the Newton's second law, and the atomic trajectories are predicted through integration of the equation of motion. Different interatomic interaction in different materials are determined through the specified potential, and no other assumptions need to be made, such as critical ablation conditions (temperature and pressure), and no parameters need to be specified in the lattice, such as

heat capacity, thermal conductivity, elastic modulus, and their dependence on other properties.

The combined continuum-atomistic model TTM-MD [77,78] is given as follows,

$$\frac{\partial}{\partial t}\left(C_e T_e\right) = \nabla \cdot \left(K_e \nabla T_e\right) - G\left(T_e - T_l\right) + S \tag{3.41}$$

$$m_i \frac{d^2 \mathbf{r}_i}{dt^2} = \mathbf{F}_i + \gamma_i m_i \mathbf{v}_i^T \tag{3.42}$$

where Eq. (3.41) keeps the same form as Eq. (3.1) in TTM to describe the thermal response in electron, and Eq. (3.42) is used in replace of Eq. (3.2) to represent lattice behavior in atomic level.

In Eq. (3.42), m_i and $\mathbf{r}_i$ are the mass and position of the ith atom, $\mathbf{F}_i$ is the total force acting on the ith atom due to its interaction with surrounding atoms, the second term on the right hand side in the form of external force represents the thermal energy through electron-phonon coupling as that in Eq. (3.2), and γ_i is the coefficient to represent the strength of this thermal energy coupling. For a computational cell in the simulation domain, this coupling coefficient is treated to be identical for each atom in the cell, given as,

$$\gamma_i = \frac{GV\left(T_e - T_l\right)}{\sum_{i=1}^{N} m_i \left(\mathbf{v}_i^T\right)^2} = \frac{GV\left(T_e - T_l\right)}{3k_B N T_l} \tag{3.43}$$

where N and V are the number of atoms and volume within a computational cell, k_B is the Boltzmann constant, and $\mathbf{v}_i^T$ is the thermal velocity of the ith atom, which should be distinguished from the absolute velocity $\mathbf{v}_i$ for the contribution to thermal kinetic energy in that,

$$\mathbf{v}_i^T = \mathbf{v}_i - \mathbf{v}^c \tag{3.44}$$

where $\mathbf{v}^c$ is the center of mass velocity in the collection of atoms in the computational cell, calculated in the form of,

$$\mathbf{v}^c = \sum_{i=1}^{N} \left(m_i \mathbf{v}_i \right) \Big/ \sum_{i=1}^{N} m_i \tag{3.45}$$

Thermodynamic properties are calculated based on the thermal velocity, and lattice temperature is defined as,

$$T_l = \frac{1}{3k_B N} \sum_{i=1}^{N} m_i \left(\mathbf{v}_i^T \right)^2 \tag{3.46}$$

Pressure, as the most important quantity in study of the mechanical response, can be calculated based on the virial theorem [79] given as,

$$P = \frac{N k_B T_l}{V} + \frac{1}{6V} \left\langle \sum_{i=1}^{N} \sum_{j \neq i}^{N} \mathbf{F}_{ij} \cdot \mathbf{r}_{ij} \right\rangle \tag{3.47}$$

where $\mathbf{F}_{ij}$ and $\mathbf{r}_{ij}$ is the interatomic force and distance between the *i*th and *j*th atom.

The thermal diffusion equation of electron in TTM (Eq. (3.41)) is solved by implicit finite difference method to maintain the unconditional stability in numerical calculation. The application of the implicit scheme could be computationally more efficient compared to the explicit scheme in solving this equation, where multiple sub-steps need to be applied within one MD time step to maintain the numerical stability based on the von Neumann stability criterion [80,81]. The atomic equation of motion is integrated through the Velocity-Verlet algorithm based on the large-scale atomic/molecular massively parallel simulator (LAMMPS) [82]. The unit cells in MD simulation domain is defined based on the finite difference discretization in TTM, and the cell-based electron temperature in TTM is related with the lattice temperature, which is defined as the average thermal kinetic energy for the collection of atoms in the corresponding MD cell, as given by Eq. (3.46).

During thermalization of lattice, the simulation domain in the MD part will change due to thermal expansion and material decomposition, which are considered in the TTM part by activating (deactivating) new (existed) cells. The criterion to determine the simulation cell activation (deactivation) is based on the atom number, and the critical value is taken as 10 percent of the average atom number in a cell in the initial MD domain, as suggested in [81]. Within the deactivated cells, the electron-phonon thermal coupling will be terminated to avoid the influence from unphysically fluctuated lattice temperature, and dynamics of atoms will follow the original MD equation of motion without the external force term. In addition, along with atomic motion, the number (density) of atoms in the unit cell will change, and the variation should affect the local thermal properties, such as thermal conductivity and heat capacity, which are dependent on material density [79]. To account for this effect, the electron thermal properties are scaled by the ratio of number (density) of atoms in the corresponding MD cells to that in the initial system. This consideration is especially important when gas bubble and vacuum space form between material layers, where the electron thermal diffusion should be neglected.

This TTM-MD combined model is developed to explore the interaction between ultrafast laser and metals. As for study of ultrafast laser interaction with dielectric materials (fused silica), the plasma model (SRE) needs to be further combined in TTM-MD model to account for electronic dynamics.

3.3.2 Interatomic potential

In study of metals, taking copper as example, embedded-atom-method (EAM) [83] potential by [84] has been adopted to describe the interatomic interaction due to its high accuracy in describing thermal and mechanical properties for Cu [85]. The potential energy of the *i*th atom is expressed as,

$$E_i = F_\alpha\left(\sum_{i\neq j}\rho_\beta\left(r_{ij}\right)\right)+\frac{1}{2}\sum_{i\neq j}\phi_{\alpha\beta}\left(r_{ij}\right) \tag{3.48}$$

Where r_{ij} is the distance between atom *i* and *j*, $\phi_{\alpha\beta}$ is a pair-wide potential function, ρ_β is the contribution to the electron charge density from atom *j* of type β at the location of atom *i*, and *F* is an embedding function that represents the energy required to place atom *i* of type α into the electron cloud.

As for dielectric material, taking fused silica as example, CHIK [86] potential has been adopted to describe interatomic interaction due to its high accuracy in predicting structural and mechanical properties for fused silica [87],

$$U_{CHIK}\left(r_{ij}\right)=\begin{cases} a_{ij}r_{ij}^2+b_{ij}r_{ij}+c_{ij} & r_{ij}\le r_{ij}^0 \\ q_iq_j/4\pi\varepsilon_0 r_{ij}+A_{ij}e^{-B_{ij}r_{ij}}-C_{ij}/r_{ij}^6 & r_{ij}^0<r_{ij}\le r_c \\ q_iq_j/4\pi\varepsilon_0 r_{ij} & r_{ij}>r_c \end{cases} \tag{3.49}$$

where *U* is the potential, *A*, *B*, *C* are Buckingham parameters, *q* is the atomic charge, *r* is the interatomic distance between atom *i*, *j*, and ε_0 is the vacuum permittivity.

The major drawback of Buckingham potential is the unphysical attraction between particles for small distances. This issue can be addressed by adding a higher order short-range Lennard-Jones term as in [88,89] or by replacing the original potential with a simple

second-order polynomial within a small distance [87,90]. In this work, a simple second-order polynomial is adopted to describe the interatomic interaction for Si-Si, Si-O and O-O pairs, as in Eq. (3.49) (a), where r_0 is the cutoff distance to apply the corrected function, and a, b, c are the second-order polynomial coefficients, which were determined to maintain the continuity of potential energy and forces with the original potentials at the cutoff distances. The atomic charges are $q_{\mathrm{Si}} = 1.910418$ and $q_{\mathrm{o}} = -0.955209$ taken from CHIK potential [86] and the Buckingham and second-order polynomial coefficients are summarized in Table 1. The unphysical attractions for small distances by the original Buckingham potential and correction by the harmonic functions are displayed in Figure 3.2 with solid and dash-dot lines, respectively.

Table 3.1 CHIK potential parameters used to model fused silica [87].

	Si-Si	Si-O	O-O
A (eV)	3150.462646	27029.419922	659.595398
B (Å^{-1})	2.851451	5.158606	2.590066
C (eV·Å^6)	626.751953	148.099091	26.836679
r^0 (Å)	2.5	1.4	1.4
a (eV·Å^{-2})	5.007362	42.332470	25.495271
b (eV·Å^{-1})	-33.982995	-122.912422	-108.165674
c (eV)	65.599395	75.225002	122.435286

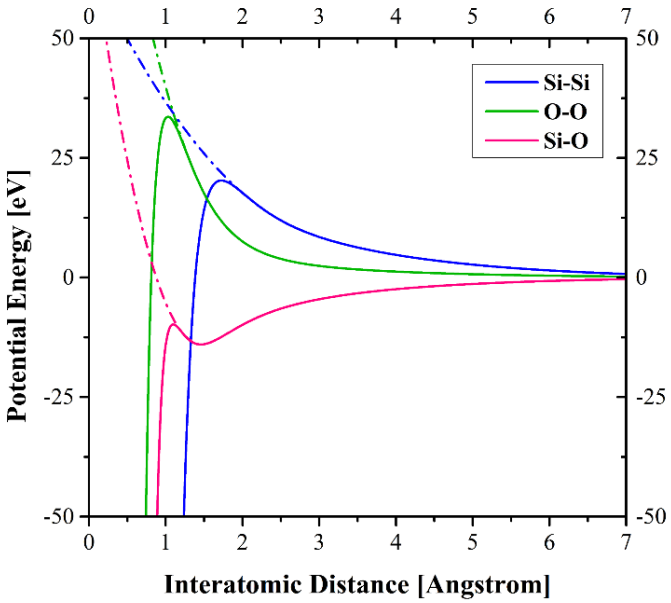

Figure 3.2 CHIK potential for pair interactions. The original Buckingham potential and its unphysical region for small distance is represented by the solid lines. The second-order polynomial modifications are represented by the dash-dot lines.

In order to calculate the electrostatic interactions with low computational cost, the Wolf method [91] can be adopted alternatively to the Ewald summation [92]. The original Coulombic potential can be truncated and shifted in the following form,

$$U_{wolf}\left(r_{ij}\right)=\frac{q_i q_j}{4\pi\varepsilon_0}\left(\frac{1}{r_{ij}}-\frac{1}{r_w^0}+\frac{r_{ij}-r_w^0}{r_w^0}\right), \qquad r_{ij}\le r_w^0 \tag{3.50}$$

where r_w^0 is the cutoff distance for electrostatic interaction, taken as 10.17 Å. The potential energy and force are smoothed to zero approaching r_w^0. This method has been validated to be a good alternative to Ewald summation for silica glass on studies of shock wave impact [87,93].

To create the characteristic structure of fused silica with disordered network of tetrahedra where each silicon is shared by four oxygen atoms, the general method in molecular dynamics simulation starts with beta-cristobalite crystal whose density is close to 2.2 g/cm^3 (typical density of fused silica in experiments [87,93]). This initial configuration is heated to 8000 K in the canonical ensemble (NVT) and equilibrated for 100 ps to diminish the initial crystal structure. The system is then cooled down to the room temperature (300 K) at the rate of 10 K/ps. The final stage of simulation is running in isothermal-isobaric ensemble (NPT) to release the internal stress at 300 K, and final density is obtained to be 2.203 g/cm^3, which matches well with the experimental density of 2.2 g/cm^3.

CHAPTER FOUR

ULTRAFAST LASER-INDUCED ABLATION MECHANISMS

In this chapter, based on MD simulations, ablation mechanism will be investigated for both metals and dielectric materials, focusing on spallation (non-thermal ablation) and phase explosion (thermal ablation). Nanoparticle formation and dynamics will be also investigated.

4.1 Ablation in metals

The MD simulation domain has been built up for copper into a face-centered-cubic (fcc) crystal in the direction of (1 0 0), with dimensions of around 1 μm by 10.8 nm by 10.8 nm (3000 by 30 by 30 unit cells with lattice parameter as 3.615 angstrom), consisting of over 10 million atoms. The selection of lateral size is balanced between computational cost and statistical stability. The lateral size in this study should be sufficiently large to avoid the influence on thermal and mechanical responses [94]. Free boundary has been applied on the top and bottom surfaces perpendicular to the laser beam propagation direction to allow material free movement after laser pulse irradiation, while periodic boundary has been applied on the lateral direction to represent much greater laser beam spot size compared to the lateral size in MD system.

The simulation domain has been discretized along (1 0 0) into unified cells with grid size of 1 nm. The selection of grid size as 1 nm is able to provide accurate description for temperature profile, especially under strong electron temperature gradient, as well as sufficient atoms (around 10000 per cell in the initial system) to represent local thermal and

mechanical properties. Prior to the irradiation of laser pulse, the MD system is equilibrated at 300 K and the internal stress is released by adjusting the simulation domain size. The simulation period after equilibration extends up to 500 ps, which is long enough for the observation of major thermal and mechanical responses.

Single-shot pulse with wavelength of 800 nm and pulse duration (FWHM) of 100 fs has been applied onto the metallic target. Wide range (0.08-5.0 J/cm^2) of laser (absorbed) fluence has been used to reveal the major mechanisms with different strength of heating in the sample.

4.1.1 Phase explosion

At moderate and high laser fluence, phase explosion (PE) or explosive boiling has been proposed to be the dominating mechanism of material decomposition. Phase explosion is featured with homogeneous nucleation and rapid decomposition of material into vapor and liquid droplets mixture. Thermal criterion can be applied to determine the occurrence of phase explosion, and 0.9 T_{cr} (critical temperature) has been widely used as the threshold temperature T_{PE}. Other values of threshold temperature have been proposed as well, such as 0.8 T_{cr} [95], and the difference could be attributed to the different methods how T_{PE} and T_{cr} have been determined. The method proposed in [96] has been used in this work to determine T_{PE}. MD simulation has been done in the isothermal-isobaric ensemble (NPT), with fixed pressure and selected temperature. The abrupt increase in the system volume reveals the fast phase transformation from overheated liquid to vapor, indicating the corresponding temperature as the T_{PE} under the given pressure. Similar to melting

temperature, T_{PE} can be raised with increasing pressure, and quasi-linear dependence can be observed. The onset of phase explosion is accompanied with relaxation of pressure close to 0 GPa [97], so that the measured T_{PE} at 0 GPa can be used as a constant criterion, instead of a variable one, to characterize phase explosion. As for the determination of critical temperature, the method proposed in [98] can be applied. With a series of canonical (NVT) simulation, isotherms on the *p*-*v* phase diagram can be obtained, and the critical temperature can be determined thereafter. The threshold temperature of phase explosion at 0 GPa and the critical temperature for copper with the employed EAM potential have been measured to be 5980 K and 6700 K, respectively, yielding T_{PE} to be 0.89 T_{cr}, matching well with the widely used thermal criterion. The critical temperature with the EAM potential is within the range of reported value (5400-9000K) [99,100], and the critical density ~2.2 g/cm^3 agrees well with the observation in [95]. Taken 5980 K as the threshold temperature, the threshold fluence for phase explosion with single laser shot can be therefore determined. The evolution of lattice temperature at laser fluence of 0.24, 0.26 and 0.28 J/cm^2 is shown in Figure 4.1 (a)-(c). The upper limit of the colorbar is set as constant value (6000 K) to facilitate the direct observation of phase explosion. Lattice temperature over T_{PE} can be observed in Figure 4.1 (a), so that 0.24 J/cm^2 can be treated as the threshold fluence for phase explosion. At laser fluence of 0.26 and 0.28 J/cm^2, as shown in Figure 4.1 (b) and (c), greater region with dark red color indicates overheating of material higher than T_{PE}, and faster expansion and increasing number of atomization reveals stronger material decomposition.

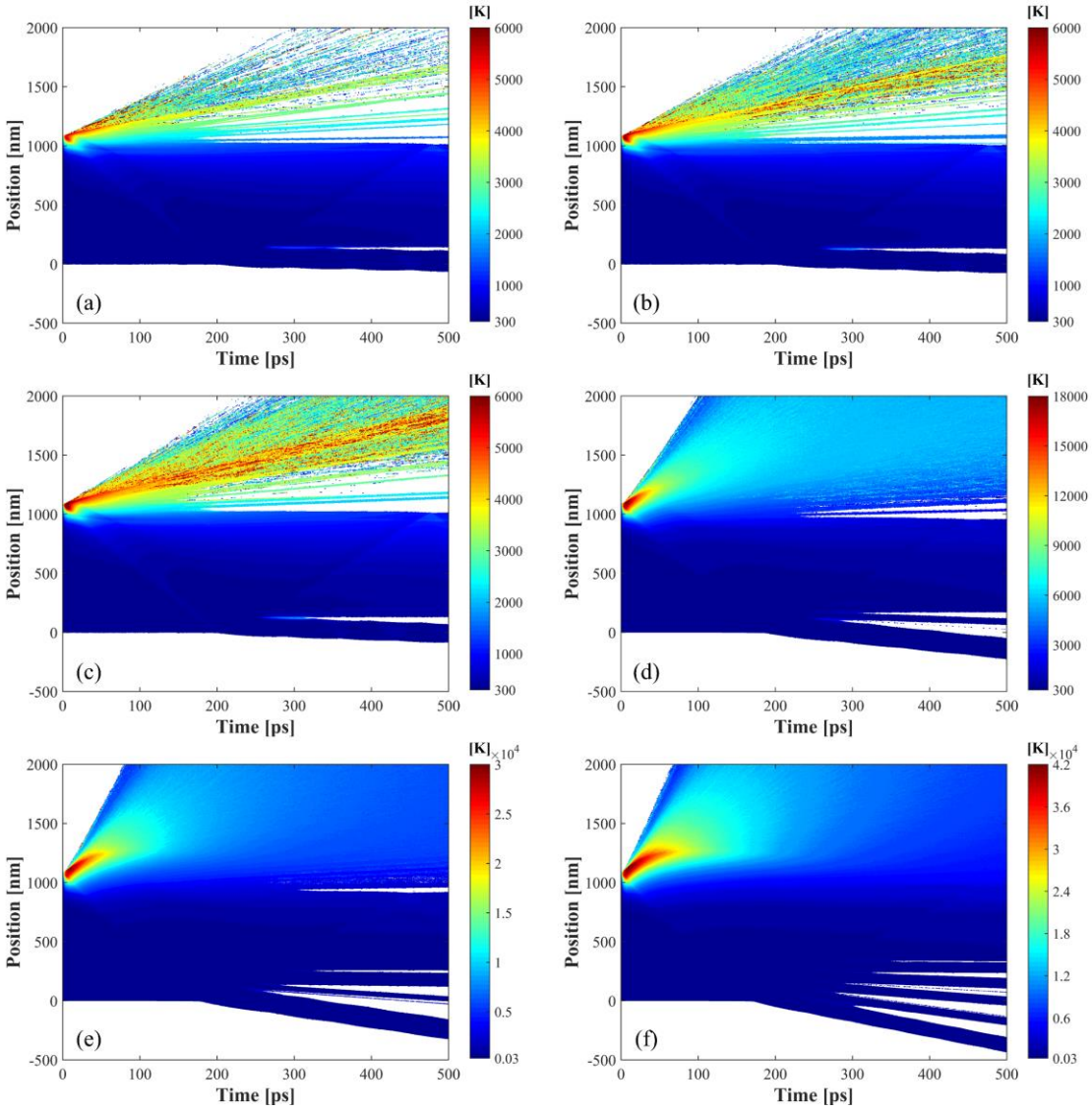

Figure 4.1 Evolution of lattice temperature in copper with femtosecond laser single pulse at (a) 0.24 J/cm^2, (b) 0.26 J/cm^2, (c) 0.28 J/cm^2, (d) 1.0 J/cm^2, (e) 2.0 J/cm^2, and (f) 3.5 J/cm^2.

In the regime of phase explosion, material decomposed through spallation can be observed as well. As shown in Figure 4.1, beneath the continuous spatial distribution of vapor and liquid mixture, discrete large-size nanoparticles with vacuum space in between

should be ejected by spallation. The coexistence of phase explosion and spallation (thermal and non-thermal ablation) can be observed for a wide range of laser fluence over 0.24 J/cm^2. With much higher laser fluence (1.0 J/cm^2) shown in Figure 4.1 (d), phase explosion has already become the dominating ablation mechanism, and when the laser fluence is raised up to 3.5 J/cm^2 in Figure 4.1 (f), no clear sign of vacuum gap can be seen in the plume, indicating negligible contribution from spallation. The reduced mechanical decomposition at high laser fluence could be attributed to the weakened rarefaction wave with fast material expansion as well as enhanced recoil pressure. When the material has been superheated to ultrahigh level above 15000 K, the critical point phase separation (CPPS) could play an important role in thermal ablation. The underlying physics of CPPS is similar to phase explosion, both with homogeneous nucleation and fast material decomposition, but the detailed thermodynamic trajectory in phase transformation could be different. In addition, superheating of material with higher threshold temperature than phase explosion has to be satisfied.

4.1.2 Spallation

Spallation is mechanical decomposition resulted from ultrafast laser-induced shock wave propagation in the material, and the underlying mechanism as well as the critical condition are of great interest in this work. Single and multiple spallation can be observed in the ablation plume, featured by discrete distribution of ejected large-size clusters away from the material. Spallation, as has been mentioned, can happen in the metal micro-size films on both the front and rear sides. On the front side, where the material has been

thermalized and melted, the decomposition of material is initiated by the arrival of the tensile stress carried by the rarefaction wave. Based on this, the front-side spallation should be characterized as thermal-assisted mechanical decomposition, resulted from interplay of thermal and mechanical effects induced by ultrafast laser. The requirement of material heating is much lower than T_{PE}, but still above the regime of melting, otherwise the local tensile strength cannot be effectively reduced below the magnitude of pressure wave. Given that the material has not been overheated above T_{PE}, the absence of rarefaction wave will not bring about ejection of large-size nanoparticles, but limited number of particles evaporated from the surface. On the rear side, weakening of material is much lower due to thermal effects, and phase transformation from solid to liquid cannot be observed, so that the rear-side spallation should be identified as (pure) mechanical disintegration. The nature of spallation should be related to mechanical response in the material under tension at ultrahigh strain rate (10^9-10^{11}s^{-1}). To capture the occurrence of spallation and reveal the underlying mechanism, the study of ultrafast laser-induced spallation has been coupled with separate MD tensile test to obtain the tensile strength, which is tabulated with wide range of temperature and strain rate, selected as the most influential quantities. There has also been the measurement of spall strength in the flyer-plate or piston-driven shock wave, however, not preferable for our current study. On one hand, the dynamic properties, such as temperature, strain rate, and spall strength, are measurable but not directly and precisely controllable. On the other hand, the generation of shock wave needs large simulation domain, which will increase the computational cost significantly. Both these two concerns make the direct tensile test on supercell preferable for buildup of reference tensile strength.

During the TTM-MD simulation, temperature and strain rates will be measured on each grid, and the local tensile strength can be obtained based on the separately measured table. The local tensile strength will be compared with the local pressure, and the dimensionless quantity tension factor can be calculated as the quotient between the pressure and tensile strength. As has been mentioned, our proposition for the onset condition of spallation is the tension factor to be greater than unity, indicating higher magnitude of pressure than the local tensile strength. The local strain rate is calculated based on the equation given as [85],

$$\dot{\varepsilon} = \left(\frac{\partial u}{\partial x} + \frac{u}{\rho} \frac{\partial \rho}{\partial x} \right)_t \tag{4.1}$$

where u is center of mass velocity along the x-axis, and ρ is the material density.

Based on the proposed method to monitor the spallation events, the threshold laser fluence can be determined as 0.1 J/cm^2 and 0.22 J/cm^2 for front-side and rear-side spallation, and contour plots of lattice temperature, pressure and tension factor are shown in Figure 4.2 and Figure 4.3, respectively. As has been mentioned, discrete (single or multiple) distribution of nanoparticle ejection can be observed in both front and rear-side spallation. With the increase of laser fluence, the temperature at the surface increases from ~2700 K to ~5500 K, however, the peak temperature in both cases cannot reach the threshold temperature of phase explosion, so that the sparse distribution of small-size particles in Figure 4.1 should be attributed to surface evaporation. The characteristic temperature on the interface of spallation is much lower (below 2000 K) compared with thermal ablation (phase explosion), so that it could be classified into non-thermal ablation.

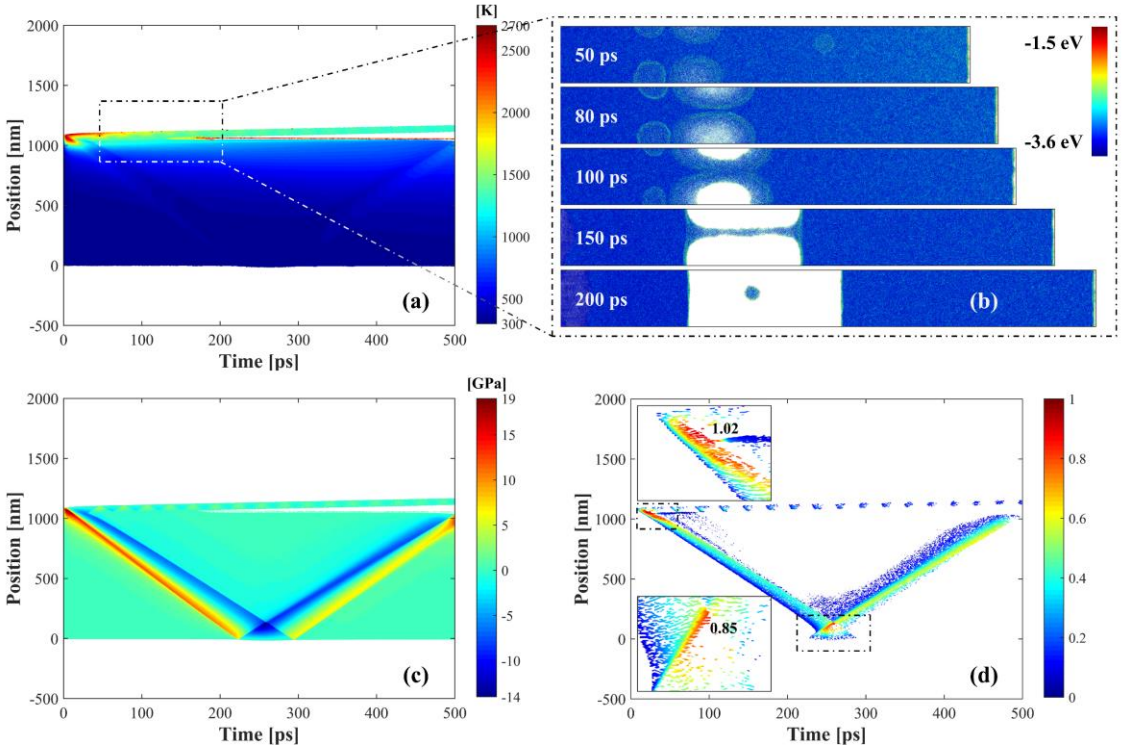

Figure 4.2 Evolution of (a) lattice temperature, (b) atomic configuration, (c) pressure, and (d) tension factor in copper with femtosecond laser single pulse at 0.1 J/cm^2. The atoms in (b) is colored according to the potential energy.

There is another non-thermal ablation mechanism as Coulomb explosion [101], where particle ejection is driven by the formation of considerably strong electric field near the surface. Coulomb explosion is not considered in this work because its less importance in the formation of plume plasma for metallic materials, compared with the generation of early stage plasma [21,102]. The enhancement of pressure wave magnitude is also apparent, especially the compressive (positive) part. On the occurrence of spallation, the shock wave propagation would be disrupted and split into two waves (treated as secondary shock induced by spallation) travelling towards opposite directions. These phenomena can be

clearly seen in the pressure contour plots on for spallation on both sides, and the secondary pressure waves are trapped in the detached layers with long-time short-range propagation. The secondary shock wave is stronger on the rear side, because the strength depends on the peak value prior to the spallation, which is much higher on the rear side (solid) than the front side (liquid).

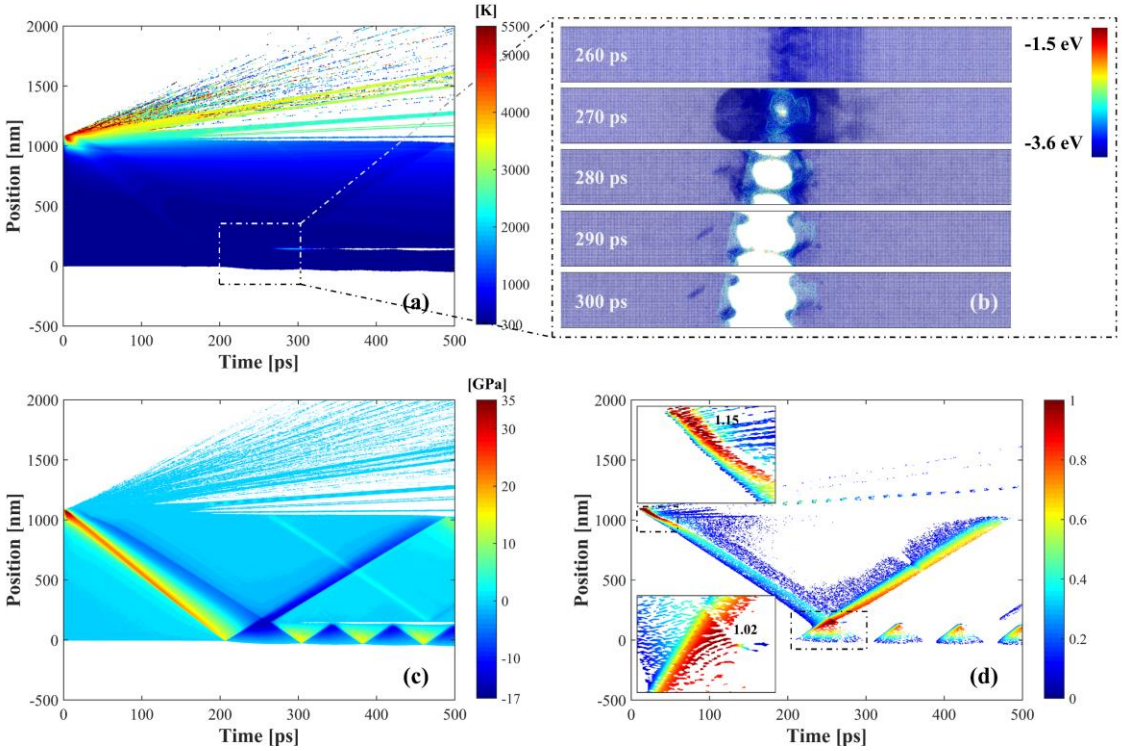

Figure 4.3 Evolution of (a) lattice temperature, (b) atomic configuration, (c) pressure, and (d) tension factor in copper with femtosecond laser single pulse at 0.22 J/cm^2. The atoms in (b) is colored according to the potential energy.

The distribution of tension factor provides a more direct way to monitor the spall events and the validate the proposed spallation criterion. The two regions with high tension factor are shown in the zoom-in windows together with the local peak value. In the case of

front-side spallation, the condition of mechanical decomposition has been satisfied, and the local peak tension factor on the front side is 1.02 (>1.0). The satisfaction of the spallation condition has been located between 21 ps and 22 ps, which is much earlier than the detachment of the spalled layer from the base material. The local peak tension factor on the rear side is 0.85, still far away from the requirement for the onset of spallation. As for the case of rear-side spallation, the proposed condition can be satisfied on both sides, and the tension factor on the front side reach up to 1.15, indicating the material under super-tension if the pressure wave is stronger than the threshold. If the peak value of tension factor could be greater than 1.0, it is highly possible that there will be multiple spallation, happening either simultaneously or sequentially, around the peak value, because the tension factor could surpass the threshold (1.0) in a wide region rather than a single position. The occurrence of spallation is not an instant process, including void (gas bubble) nucleation, growth and coalescence, so that there can be noticed certain time delay in tens of picosecond scale between the initiation of spallation (appearance of high tension factor) and completion of material detachment. The position where spallation can happen is in certain distance away from the surface, which is mainly because the development of strong enough tensile stress in the rarefaction wave or the rear-side reflected tensile wave cannot be formed instantly but in a long enough period in time or distance in space. This is the reason why spallation is accompanied with large-size nanoparticle ejection, and smaller clusters can be obtained with increasing laser fluence. Therefore, the ejected material layer, especially on the rear side, is limited in a relative thick range over tens of nanometer, unless the local material strength can be effectively reduced through enhanced temperature.

Detailed process of spallation has been shown in Figure 4.2 (b) and Figure 4.3 (b) to facilitate the comparison between front-side and rear-side spallation. In Figure 4.2 (b), void generation and development can be clearly seen, and there forms a liquid bridge when the void has been elongated and the front-side material is ready to be detach from the sample. Along with the separation of material, a liquid spherical nanoparticle has been formed and left in the gap space. Similar spallation process can be observed in Figure 4.3 (b) for rear-side spallation in solid phase as well, however, the spallation process on the rear side is much shorter (50 ps) than that on the front side (over 100 ps). In addition, the resultant surface roughness in the remaining material is much smaller on the front side than the rear side. These differences are mainly because of the different phases where spallation happens. On the rear side, spallation happens in solid phase, so that the ultimate tensile strain is smaller than the liquid phase on the front side, resulting in faster material breakdown. Also, during and after the material rupture, there is no material flow to flatten the newly formed surface in solid phase as what happens on the front side in liquid phase.

4.1.3 Spall strength

In this work, the determination of tensile (spall) strength is of great importance, otherwise, the tension factor cannot be calculated, and the occurrence of spallation can only be characterized by the spall strength, which can be largely affected by the temperature and the strain rate when the spallation is initiated. In that case, it will be difficult to achieve a universal criterion to define the spallation event, because the spall strength could deviate from each other among different studies employing different simulation method, spallation

condition, and interatomic potential, etc. In this section, our measured tensile strength will be compared with measurement through spallation imposed through collision-based shock wave [85], and its dependence on temperature will be discussed with comparison to several theoretical descriptions in previous studies. Validity of the linear acoustic approximation in the measurement of spall strength will be discussed as well.

Our measurement results of tensile strength for copper with various strain rate (10^9-10^{11}/s) at different temperature are shown in Figure 4.4 (a). The spall strength in [85] has been measured through the flyer plate-target method at similar strain rate (10^{10}-10^{11}/s) by controlling the velocity of flyer plate and adjusting the dimensions of the sample. Good agreement can be seen between the spall strength and our measurement of tensile strength at well-controlled strain rate and temperature, indicating the nature of spallation as tensile process at ultrahigh strain rate. In Figure 4.4 (a), it can be seen that the tensile strength follows linear decease with the increase of temperature in the solid regime below melting temperature (~1339.6 K), similar to the observation of the spall strength measurement in aluminum [103]. When the tensile strength comes into the liquid regime, continuous but much slower decrease can be observed, which could be described by the inverse exponential function. Other theoretical description and fitting function for the temperature dependence of spall strength has been proposed in previous studies [85,104,105]. The theoretical derivation based on energetic spall criterion [104] gives:

$$\sigma_{sp} = \left(6\rho^2 c^3 \gamma \dot{\varepsilon}\right)^{1/3} \tag{4.2}$$

where c is the sound speed, and γ is the surface tension, given in the form of [105]:

$$\gamma = \gamma_0 \left(1 - T_l / T_{cr}\right)^{1.25} \tag{4.3}$$

where γ_0 is the surface tension at the melting temperature.

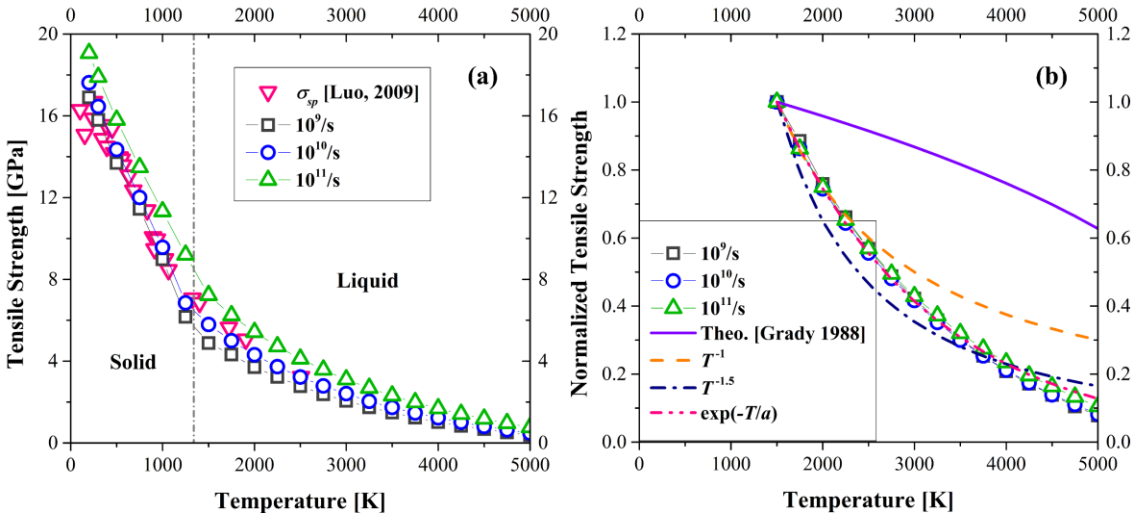

Figure 4.4 Measurement of (a) tensile strength with various strain rate at different temperature, and (b) normalized tensile strength with comparison to theoretical description and different fitting models.

Inverse power law has been proposed in [85] as $\sigma_{sp} \propto T_{sp}^{-n}$, and the exponent has been determined as ~1.0 through fitting. The aforementioned theoretical description, inverse power law and our proposed inverse exponential function has been depicted together in Figure 4.4 (b). To avoid the difference from selection of constant parameters, all the calculated results have been normalized to the value at 1500 K. The critical temperature in Eq. (4.3) is adopted by our measured value as mentioned in Section 3.2. At different strain rate, little difference can be observed in the normalized tensile strength in this wok, indicating minor/negligible dependence of the scaling law of the σ_{sp} - T_{sp} relation

on the strain rate. However, there is great differences between the theoretical description and our measurements, which can be characterized by the concave and convex function, respectively. Overestimation, especially at high temperature, in the theoretical description may lead to underestimated spallation and overestimated fracture period, which has been considered in the form given in [104,105]. The inverse power law cannot provide overall agreement with our data as favorable as the inverse exponential function. The $\sigma_{sp} \propto T_{sp}^{-1}$ relation does provide good prediction for tensile strength in the low temperature range, however, increasing deviation with temperature higher than ~2500 K. The adjusted relation as $\sigma_{sp} \propto T_{sp}^{-1.5}$, which achieves the overall least error, still cannot match with our data, indicating first underestimation and then overestimation. In comparison, our proposed fitting law as inverse exponential function is able to provide much better agreements in a wider range of temperature. The fitting parameter *a* has been adjusted to be 1700 for the best match in this case, and this inverse exponential fitting law could be further validated in studies of multiple materials.

Another method to obtain the spall strength is indirect measurement through the linear acoustic approximation [106] in the form of:

$$\sigma_{sp} = \rho c \Delta u / 2 \tag{4.4}$$

where Δu is the pullback velocity (difference between the velocity at the peak and first valley), which can be measured on the rear-side surface with respect to the incoming direction of shock wave. The linear acoustic approximation has been widely used in spall experiments [107,108] due to its convenience of application in the indirect way, however, limitation and inaccuracy has been observed in recent studies [94,106].

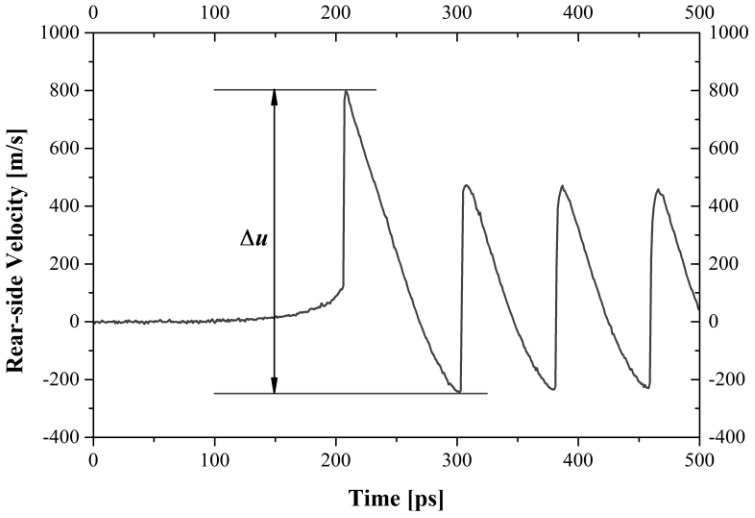

Figure 4.5 Evolution of rear-side velocity in copper with femtosecond laser single pulse at threshold fluence of rear-side spallation (0.22 J/cm^2).

Based on the measurement of pullback velocity profile in the rear-side spallation case, shown in Figure 4.5, the spall strength predicted by the linear acoustic approximation is ~22.3 GPa, which is ~38% higher than the direct measurement from the pressure profile as ~16.2 GPa. Both of these measured results agree well with the observation in spall damage simulation [106] using high target-to-flyer thickness ratio to obtain the shock loading in Taylor wave. The overestimation in the spall strength from the linear acoustic approximation could be mainly attributed to improper usage of parameters in Eq. (4.4). As reported in [106], the sound speed could be overestimated by as high as 30%-40% without consideration of its dependence on pressure. With the corrected sound speed, the accuracy in the prediction of spall strength through linear acoustic approximation can be greatly enhanced, which should be highly beneficial to future application of this simplified method.

It is of great worth to recall that our introduction of tension factor is important to unify the criterion on the occurrence of spallation, which could be largely affected by the spall temperature and strain rate, therefore making it difficult to compare among different studies. To compare with the reported study on laser-induced spallation of gold in [94], we also did the laser simulation for gold, in which the rear-side spallation strength has been measured to be ~14 GPa, 20% higher than their measured value as 11.6 GPa. Same EAM potential [109] has been applied, so that the main reason for this discrepancy should be the difference in spall temperature (not provided in [94] potentially due to different simulation settings. The contribution of strain rate in the different spall strength should be much weaker because similar value has been obtained calculated from the rear-side velocity profile. By this example, we can clearly understand that the introduction of tension factor would make more direct and convenient comparison among different studies, so as to provide universal criterion for mechanical decomposition in future studies.

4.1.4 Structural effects

So far, dominating mechanisms in ultrafast laser-induced thermal and mechanical responses, including melting, phase explosion and spallation, have been investigated based on the combined continuum-atomistic simulation. Characteristic temperature has been generally employed to represent the occurrence and development of melting and phase explosion. While in study of mechanical decomposition, dimensionless quantity, tension factor, has been introduced and universal criterion for the onset of spallation has been proposed and validated, indicating the coincidence between the occurrence of spallation

and the over-unity of tension factor. Temperature and strain rate have been considered as the most influential parameters in the determination of material strength under tension. However, further observations drive us to take other factors into account, which may challenge our proposed criterion for mechanical decomposition to certain extent. The distribution of tension factor at various laser fluence higher than the threshold value for rear-side spallation F_{sp}^{rear} (0.22 J/cm^2) is shown in Figure 4.6. With laser fluence no much higher than F_{sp}^{rear} until 0.5 J/cm^2, the peak tension factor on the rear side, as depicted in Figure 4.6 (a) and (b), are greater than 1.0, which is consistent with the spallation criterion, and there is slightly increase from 1.04 to 1.05 with the increase of laser fluence from 0.3 J/cm^2 to 0.5 J/cm^2, revealing ~5% over-tension in the solid state of material under dynamic tensile stress during the propagation of shock wave. When it comes to higher laser fluence than $\sim 3.0F_{sp}^{rear}$ (not necessarily the exact threshold value), as shown in Figure 4.6 (c) and (d), one should be able to notice that the peak tension factor drops to ~0.90 where rear-side spallation could still be observed. With continuous increase of laser fluence, recovery of the tension factor over 0.9 and further increase can be seen in Figure 4.6 (e) and (f), becoming 0.93 at 3.0 J/cm^2 and 1.00 at 5.0 J/cm^2. The appearance of decrease and reincrease in the tension factor with increase of laser fluence is of great interest, and could be mainly attributed to structural change prior to the incoming the tensile wave. As has been mentioned in Section 4.1.3, with ultrafast laser irradiation, material compression could be generated at the front surface and shock wave will form with the relaxation of pressure and propagate deep into the material. Great tensile stress on the rear-side material

will be brought about with the reflection of compressive shock wave, and when the tensile stress is greater than the local strength under tension, spallation on the rear side can be triggered. Based on this, different from pure tension loading in the measurement of tensile strength with the tensile tests, the compressive loading should make a difference in the crystal structure prior to the tensile wave in laser-induced rear-side spallation.

Figure 4.7 summarizes the peak tension factor on rear-side spallation as a function of compressive pressure. Decrease of tension factor below 1.0 cannot be observed until the compressive pressure reaches ~30 GPa. The tension factor rapidly drops with compression up to ~40 GPa, approaching ~0.85, and recovers with stronger compression towards ~50 GPa. The tension factor becomes stable with compression approaching ~70 GPa, saturating at ~0.95. This noticeable valley-shaped regime located between 30 GPa to 60 GPa in tension factor uncovers considerable material weakening and subsequent self-strengthening by increasing compression.

To elucidate the interrelation between strength variation and structural transformation, material structures are analyzed in Figure 4.7 ((a)-(d)) in context with the tension factor, where the crystal structures are captured during compression. Below compression of ~30 GPa, structural deformation is dominated by dislocation, represented by the discrete yellow cells in the main structure of FCC (Figure 4.7 (a)). With compression above 30 GPa, planar defects can be formed, introducing stacking faults. Increasing compression over ~40 GPa brings about greatly densified and intersecting stacking faults, establishing network of orthogonally oriented planar defects (Figure 4.7 (b)). When the compressive pressure is elevated above ~50 GPa, twinning faults appear and coexist with

stacking faults (Figure 4.7 (c)), and become densified with stronger compression approaching ~60 GPa (Figure 4.7 (d)), where twinning faults act as the dominant form of structural transformation.

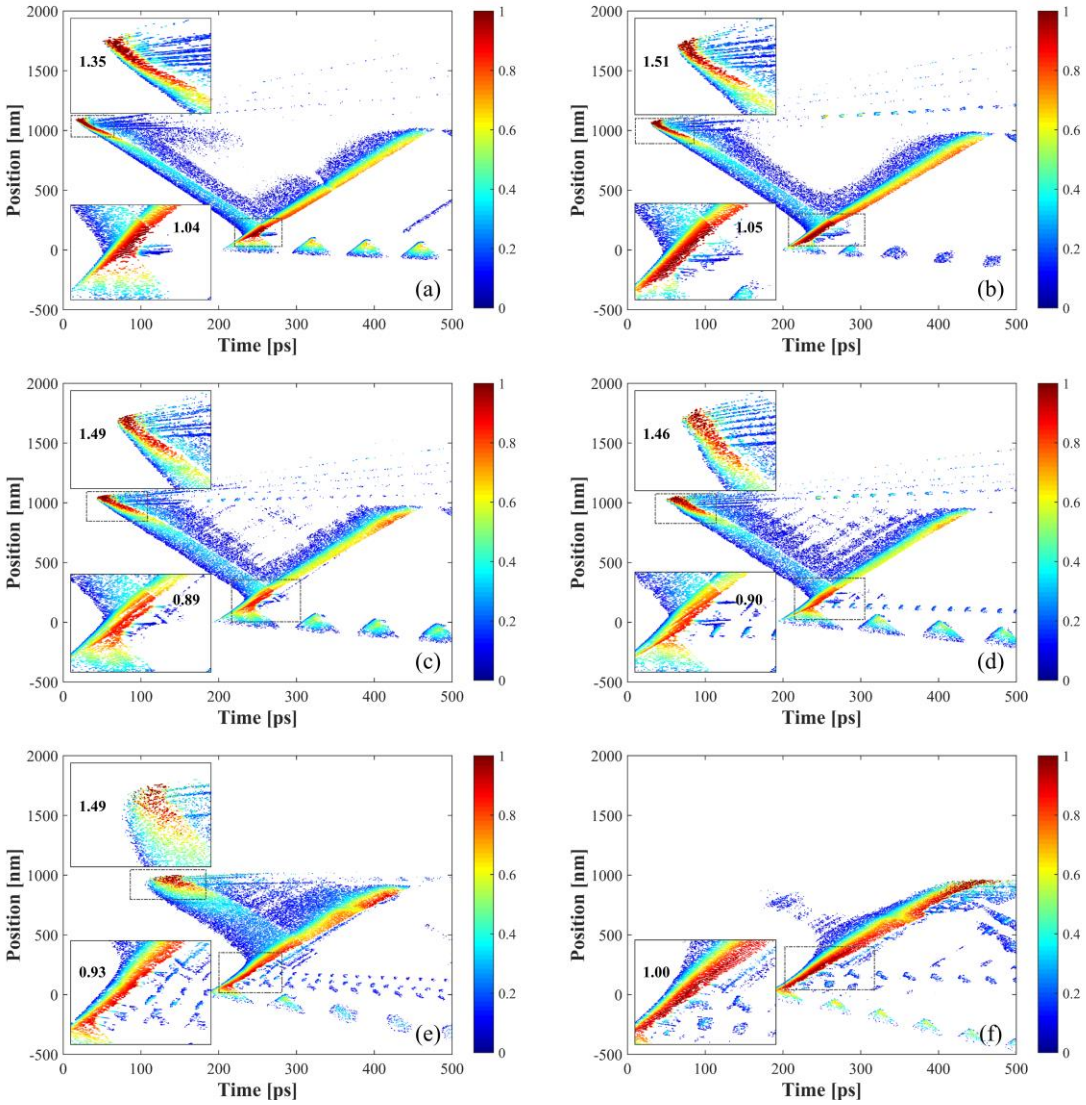

Figure 4.6 Evolution of tension factor in copper with femtosecond laser single pulse at (a) 0.3 J/cm^2, (b) 0.5 J/cm^2, (c) 0.8 J/cm^2, (d) 1.0 J/cm^2, (e) 3.0 J/cm^2, and (f) 5.0 J/cm^2.

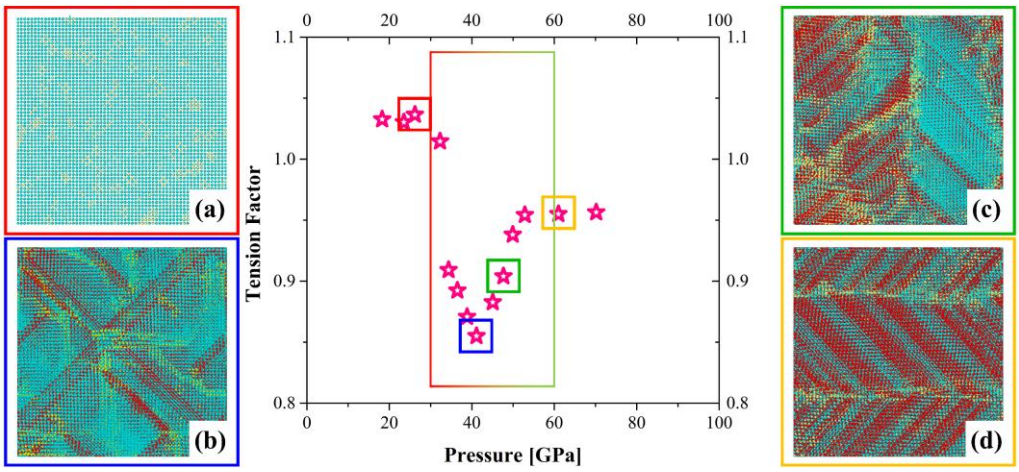

Figure 4.7 Tension factor and structural transformation as function of compressive pressure at various fluences in laser shock simulations. (a)-(d) correspond to star-marked data points enclosed by colored solid squares, depicting crystal structures in laser shock simulations at fluence of 0.5, 2.0, 3.0 and 7.5 J/cm^2, respectively. Blue, red and yellow atoms represent face centered cubic (FCC), hexagonal close packed (HCP) and body centered cubic (BCC) structures, respectively.

The evolution of structure with increasing shock compression and the dominating deformation, namely, dislocation, stacking faults and twinning faults, have quantitative agreements with previous investigations [110,111] on monocrystalline FCC structure (copper). The Hugoniot Elastic Limit (HEL) in copper determined by previous studies [110,112] (~30 GPa) has excellent agreement with the transition from elastic deformation (dislocation) to plastic deformation (stacking and twinning faults) at ~30 GPa in this work. Meanwhile, the transformation in structure from stacking faults and coexistence with twinning faults to the dominance of twinning faults, as well as the corresponding compressive pressure agree well with previous observations [110,111].

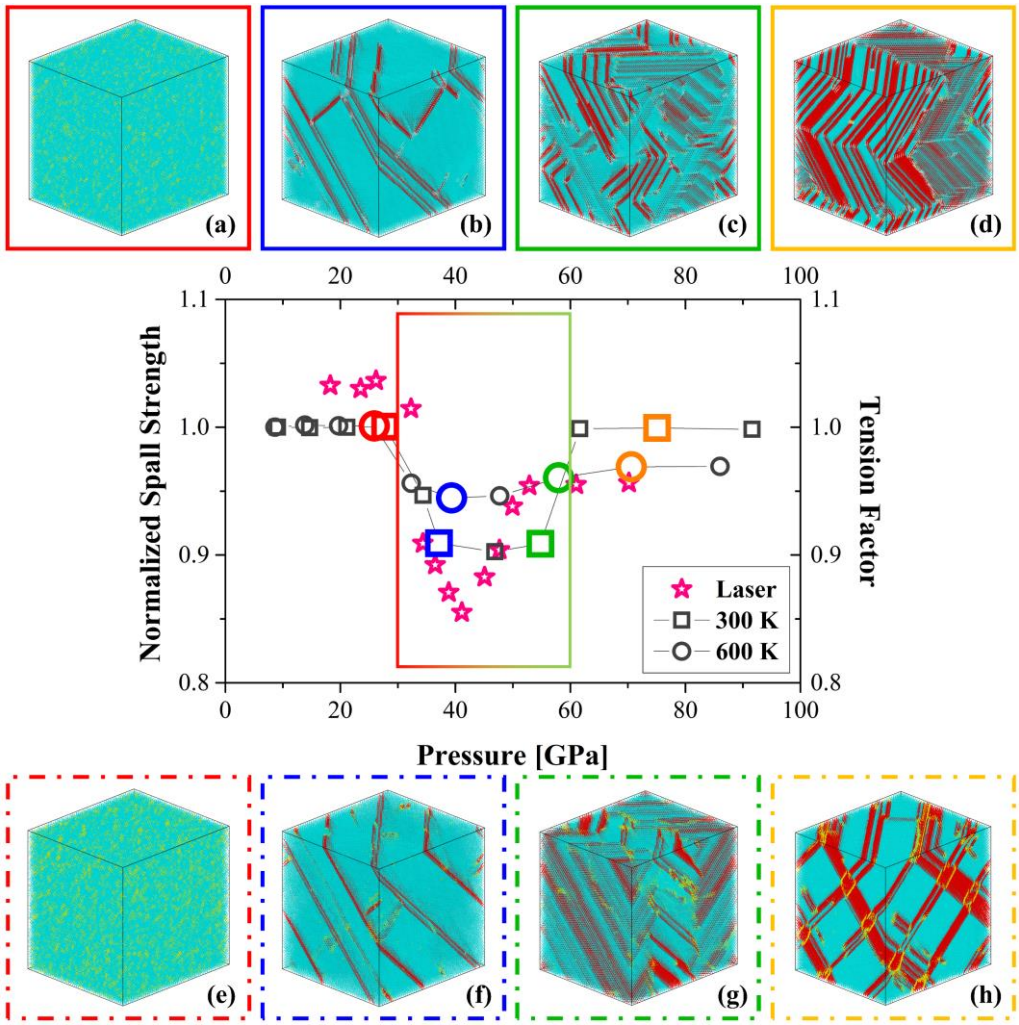

Figure 4.8 Comparison of structural transformation in correspondence to spall strength variation at different temperature in QI simulations and various fluence in laser shock simulations. (a)-(d) correspond to colored square-mark data points, depicting crystal structures in QI simulations at 300 K with compressive pressure of 28, 37, 55 and 62 GPa. (e)-(h) correspond to colored circle-mark data points, depicting crystal structures in QI simulations at 600 K with compressive pressure of 26, 40, 58 and 70 GPa.

Based on the tension factor variation and crystal structure analysis, the substantial interrelation between structural transformation and spall strength can be established as follows. Formation of elastic deformation (dislocation) below HEL introduces negligible impact on the spall strength, whereas existence of stacking faults effectuates considerable weakening of the material and diminishes the spall strength by as high as 15%. Formation of dense and intersecting stacking faults as well as generation of twinning faults at stronger compression plays a "self-healing" role in the material, and enhances the spall strength, although not to the extent as strong as material in non-defective FCC monocrystalline structure.

These results reveal that formation of stacking faults is the dominating mechanism in material weakening, while twinning can strengthen the material during spall process. This is in agreement with nanocrystalline copper [113–115], where existence of twinning provides obstacles to dislocation motion and leads to enhanced strength close to monocrystalline copper. Nevertheless, it has also been demonstrated that increasing twinning formation leads to decrease of spall strength in monocrystalline tantalum [116], which is resulted from increasing void nucleation sites near twinning boundaries. This inconsistence on the role of twinning may be in consequence of two reasons. Firstly, in terms of material strengthening, formation of twinning in this work is captured during the shock compression stage, whereas the presence of twinning and its impact on spall strength in [116] is determined during the tensile loading, which may lead to controversial conclusions on the role of twinning. According to [115], there is significantly much less twinning presence during tension than compression due to significant detwinning.

However, it is unclear whether increasing twinning by stronger shock compression leads to increasing twinning presence during tension. Secondly, the study of the twinning effects on spall strength may not be performed at same temperature and strain rate. For instance, increase of spall temperature can significantly reduce the spall strength, which may conceal possible strengthening of material by twinning. This again highlights the importance of tension factor in better understanding of the interrelation between structural transformation and spall strength, where potential impacts of temperature and strain rate can be fully excluded.

To further confirm aforementioned impacts of structural transformation on the spall strength and explore potential effects of temperature, a series of spall tests are performed in the QI method at 300 K and 600 K. The compression and tension strain rate have been selected as 10^{11}/s and 10^{10}/s, respectively, according to laser shock simulations. The spall strength calculated in the QI simulations are normalized and compared with the tension factor from laser simulations, as shown in Figure 4.8, and crystal structures ((a)-(h)) are extracted during compression at different conditions.

QI simulations provide a valley-shaped variation in the normalized spall strength with excellent agreements with that from the tension factor. The spall strength can decrease by around 10% with compression above 30 GPa, providing substantial validation on the occurrence of rear-side spallation at tension factor ~0.9 in Figure 4.6 (c) and (d). QI simulations (Figure 4.8 (a)-(d)) also provides corroborations for the structural transition from dislocation and stacking faults to coexistence with twinning faults and the dominance of twinning faults in laser-shock simulations (Figure 4.7 (a)-(d)). Quantitative

discrepancies in QI from the laser simulations can be predominantly attributed to different shock loading conditions, specifically, the simplified stress loading profile, constant strain rate and temperature in the QI simulations instead of the dynamic loading in the laser shock simulations.

Moreover, despite the similarity between 300 K and 600 K in spall strength variation, quantitative dependence on the spall temperature is captured. Compared to 300 K, the elevated minimum spall strength at 600 K indicates declined impacts from structural transformation, which can be attributed to enhanced atom mobility at higher temperature. Another noticeable discrepancy lies in the inadequate recovery of spall strength at 600 K, saturating at ~0.96, which is not as high as that at 300 K whereas in better agreement with the tension factor from laser shock simulations. This should be again attributed to the enhanced atom mobility, which limits formation of dense twinning faults, so that material "self-healing" is diminished. This restrained formation of twinning can be confirmed from structural analysis at 600 K, as shown in Figure 4.8 (g) and (h), where dense and intersecting stacking faults dominate under strong compression even beyond 60 GPa, while twinning faults are imperceptibly generated.

Tension factor serves as an easy-implemented method to exclude the impacts of temperature and strain rate, and better quantify the impacts of structural transformation on spall strength. In this regard, future investigations can be performed with consideration of different structure types (BCC [108,116], polycrystalline [117,118] and nanocrystalline [115]), crystalline orientations [116], grain size [118] and so forth.

4.2 Ablation in dielectrics

The fused silica sample in MD simulation is built up into a domain with length of 100 nm and square cross section of 10 nm by 10 nm. The selection of lateral size is balanced between computational cost and statistical stability. Free boundary condition is applied on the top surface normal to the laser beam propagation direction to allow material free movement after laser pulse irradiation, while non-reflecting boundary [119] and periodic boundary are set on the bottom and lateral direction, respectively. The simulation domain has been discretized along the length into unified cells with grid size of 1 nm. The simulation time after equilibration extends up to 120 ps, which is long enough for the observation of major thermal and mechanical responses. Single-shot laser pulse at wavelength of 800 nm and pulse duration (FWHM) of 100 fs has been applied in a wide range (3.0-10.0 J/cm^2) of laser fluence to reveal the dominant mechanisms at different regimes of laser heating.

4.2.1 Structural properties and ablation threshold

On the creation of fused silica in molecular dynamics simulation, structural properties have been assessed to confirm the characteristic structures in fused silica glass. Pair correlation function $g(r)$ and bond-angle distribution (BAD) function $p(\theta)$ are obtained to account for short to long-range structural features. Measurement of $g(r)$ for Si-Si, O-O, and Si-O pairs are shown in Figure 4.9 (a), and the location of the first peak are measured as $r_{Si\text{-}Si}$=3.17 Å, $r_{O\text{-}O}$=2.63 Å, and $r_{Si\text{-}O}$=1.63 Å, respectively. These results agree well with experimental data $r_{O\text{-}O}$=2.62-2.65 Å, $r_{Si\text{-}O}$=1.61-1.62 Å [120–122] and simulation data $r_{Si\text{-}}$

$_{Si}$=3.067-3.155 Å using other potential forms [87,90]. As for BAD measurements, the bond-angle distribution of O-Si-O and Si-O-Si angles are calculated and displayed in Figure 4.9 (b), and the peak values are located at 109° and 149°, respectively, which are also close to those reported from experiments [120–122] and simulation using other potential forms [87,90]. Good agreements in structural properties between previous studies and this work indicate proper preparation of sample material (fused silica) for the following studies of ultrafast laser-induced modifications.

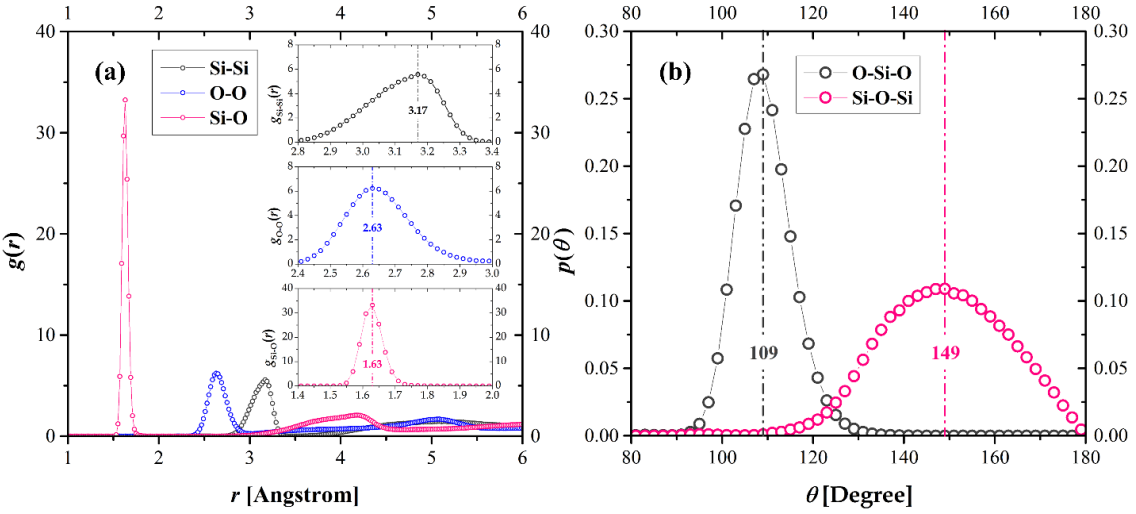

Figure 4.9 (a) Pair correlation function for Si-Si, O-O, Si-O pairs, and (b) bond-angle distribution function for O-Si-O, Si-O-Si angles in MD modeling of fused silica at 300 K.

Tensile strength as an important mechanical property can be used to further validate the material structure. Tensile strength is measured as the ultimate strength in the normal tensile test [123]. In this work, with CHIK potential, tensile strength is measured for fused silica in wide range of stain rate and temperature, which are treated as the most essential factors affecting the tensile strength. Figure 4.10 depicts the tensile strength at different

strain rates and temperature together with the literature data. Similar variation of tensile strength with temperature can be observed for different strain rates. The tensile strength follows linear decrease with the increase of temperature below 2000-2500 K, which is similar to the observation from metals [85,103]. As for higher temperature, there is faster drop of the tensile strength until ~4000 K, and much slower decrease above 4000 K.

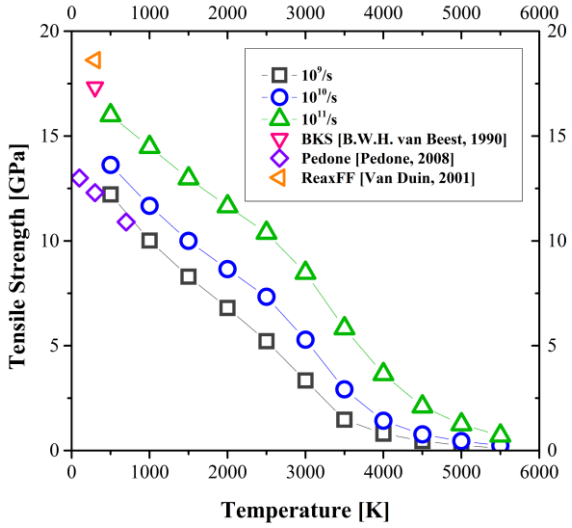

Figure 4.10 Comparison of tensile strength for fused silica using CHIK potential and other potential forms from literature at various temperature and strain rate.

Measurements of tensile strength are compared with other potential forms from the literature, namely, BKS [124], Pedone [123], and ReaxFF [125]. The depicted data from different potentials are measured at strain rate close to 10^9/s. The measurement of tensile strength in this work agrees better with Pedone potential, compared with BKS and ReaxFF [126], which predict higher strength than CHIK by 24% and 30%, respectively. Additionally, the temperature dependence of tensile strength agrees well with Pedone potential.

The dependence of tensile strength on strain rate is summarized and compared with other potential forms as well, as shown in the inserted window in Figure 4.10. All the data are normalized to the strength at 10^9/s to eliminate the differences of tensile strength from different potentials and facilitate the comparison. Similar variation with strain rate can be observed for different potential forms, with continuous increase of tensile strength at higher strain rate. Strain-rate independence of tensile strength has been observed with ReaxFF at strain rate above 10^{13}/s [125], which can be absent for other forms of potential including CHIK. However, this will not challenge the validity of observation in laser-induced thermal and mechanical responses, as the strain rate in laser modification generally does not exceed ~10^{11}/s. Despite certain differences in the tensile strength measurement between CHIK and other potential forms, similar variation of tensile strength with temperature and strain rate has been attained.

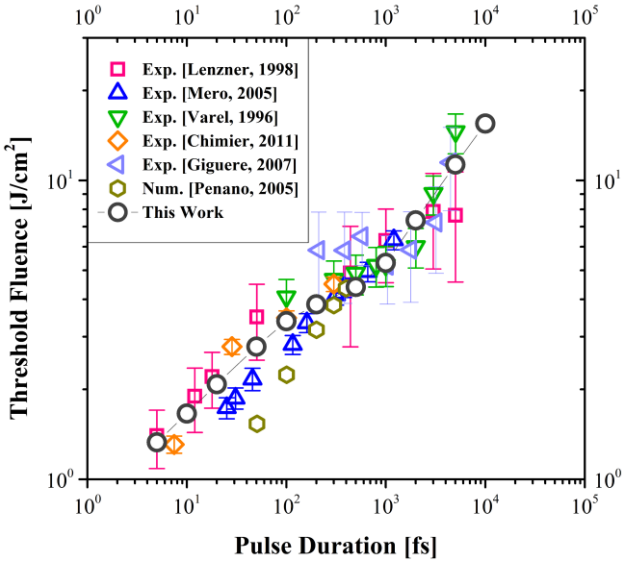

Figure 4.11 Ablation threshold fluence of fused silica with ultrafast laser irradiation at different pulse duration.

Figure 4.11 displays the ablation threshold fluence as a function of pulse duration in double-logarithmic (log-log) axis. The threshold fluence in this work is determined based on the occurrence of material breakdown in MD simulations and compared to experimental and simulation results from the literature. Good agreements can be obtained in the whole range of simulation (5 fs-10 ps), and piecewise scaling laws ($F_{th} \propto \tau_p^n$) can be applied in different regimes. In the regime below 100 fs, exponent of 0.31 can be obtained from linear fitting, while in the regime between 100 fs and 1 ps, the dependence of threshold on pulse duration fits well with an exponent of 0.19. As for the regime above 1 ps, the exponent is fitted as 0.48, which is close to 0.5, so that the scaling law of $F_{th} \propto \sqrt{\tau_p}$ can be satisfied. This scaling law for longer pulses is mainly resulted from heat diffusion, and in good agreement with previous theoretical [127] and experimental observations [25,128]. The threshold fluence for fused silica at different pulse duration has been experimentally measured by Mero *et al.* [129] and scaled with exponent of 0.33±0.01, which is in excellent agreement with simulation results in the regime below 100 fs. Christensen *et al*. [31] obtained 0.24 as the fitted exponent in the regime below 1 ps, and experimental results from Tien *et al*. [130] can be fitted with exponent of 0.23 [31], while results from Varel *et al*. [131] can be fitted to exponent of 0.11 below 1 ps. Based on these, the scaling exponent (0.19) for current simulation in the regime between 100 fs and 1 ps has fair agreement with previous observations falling between 0.11 and 0.24. Therefore, threshold fluence predicted from the SRE-TTM-MD combined model matches well with experimental and theoretical observations, indicating good capability of the numerical

model in demonstration of the dominant physical mechanisms during ultrafast laser pulse interaction with dielectric materials in wide range of pulse duration.

4.2.2 Material decomposition and phase transition

Figure 4.12 demonstrates the temporal evolution of mass density distribution for fused silica at irradiation of a single 100 fs laser pulse with increasing fluence (3.3, 3.5, 3.6, and 6.0 J/cm^2). For better visualization, atomic configurations of ablation plume are summarized in Figure 4.13, illustrating different regimes of ablation processes at different levels of fluence.

At the fluence of 3.3 J/cm^2, there is no observable material decomposition at the surface, and melting is the dominant process at this condition. As shown in Figure 4.12 (a), there is clear thermal expansion at the surface, indicated by the movement of surface. There are two stages of melting in the material with ultrafast laser pulse irradiation, including homogeneous and heterogeneous nucleation [97]. The former one refers to quasi-isochoric heating of lattice resulted from hot electrons, while the latter one is much slower, dominated by heat diffusion. Due to the much smaller thermal conductivity in fused silica than in metals, heterogeneous nucleation would play a much less significant role in the development of melting layer. After ~20 ps, as shown in Figure 4.12 (a), the surface starts to shrink back to the material, indicating the re-solidification process by surface cooling. Due to the slow pace of heat diffusion, the re-solidification process can take much longer time than the melting process. Despite the absence of material decomposition, minor

surface evaporation can be observed in Figure 4.13 (a), with sparsely distributed nanoparticles.

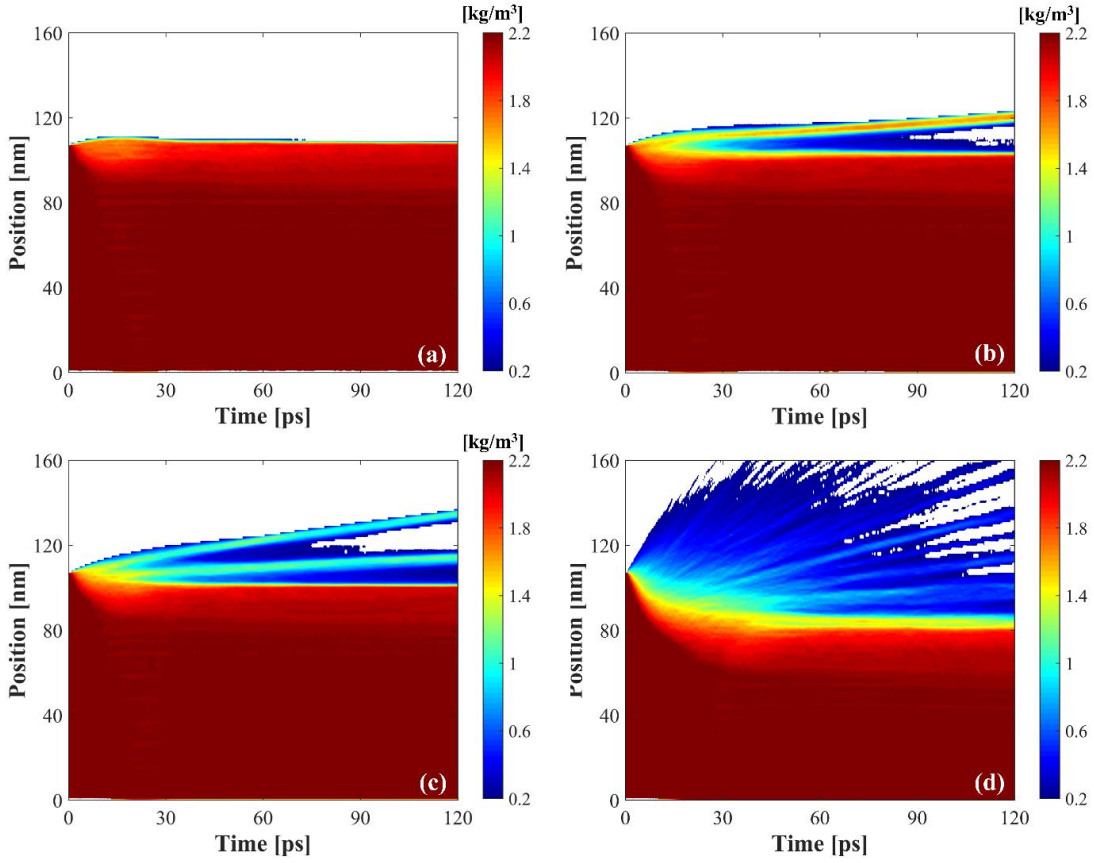

Figure 4.12 Evolution of spatial density distribution with time with 100fs laser at fluence of (a) 3.3 J/cm^2, (b) 3.5 J/cm^2, (c) 3.6 J/cm^2, (d) 6.0 J/cm^2. Spaces with density lower than 10% of the bulk material (2.2 kg/m^3) are shown as blank portions.

When the fluence is raised to 3.5 J/cm^2, material starts to be decomposed and ejected, indicating the occurrence of ablation, so that the ablation threshold fluence for 100 fs laser pulses can be determined as ~3.5 J/cm^2. As shown in Figure 4.12 (b) and (c), a whole layer of material can be ablated from the based material, indicating the occurrence

of spallation [5,7], and double-layer spallation can be observed with slightly increasing fluence (3.6 J/cm^2). Spallation is not an instant process, where material decomposition comes with void nucleation, growth and coalescence, so that there can be noticeable time delay (tens of ps) between the initiation of spallation (arrival of rarefaction wave) and eventual material disintegration. As depicted in Figure 4.13 (b) and (c), the material between the spalled layer and unablated part would be elongated during the development of gas bubble, forming a liquid bridge before the final detachment of spalled layer. Meanwhile, spallation is triggered by the tensile wave in an ultrashort period of time (a few picoseconds), so that the initiation of spallation is induced by the formation of thermal-elastic stress under the thermal confinement condition in an ultrafast process. The location where spallation happens is in certain distance away from the surface, which is mainly because the development of strong enough tensile stress in the rarefaction wave. This is the reason why spallation is accompanied with large-size clusters ejection, and smaller clusters can be obtained with increasing laser fluence. Spallation can be characterized as thermal-assisted mechanical decomposition, resulted from interplay of rapid heating and mechanical effects induced by ultrafast laser pulses. As a non-thermal ablation process, the requirement of material heating in spallation is lower than thermal ablation mechanisms, such as phase explosion [5,97,132], critical-point phase separation (CPPS) [6], fragmentation [5,7] and vaporization [5,7].

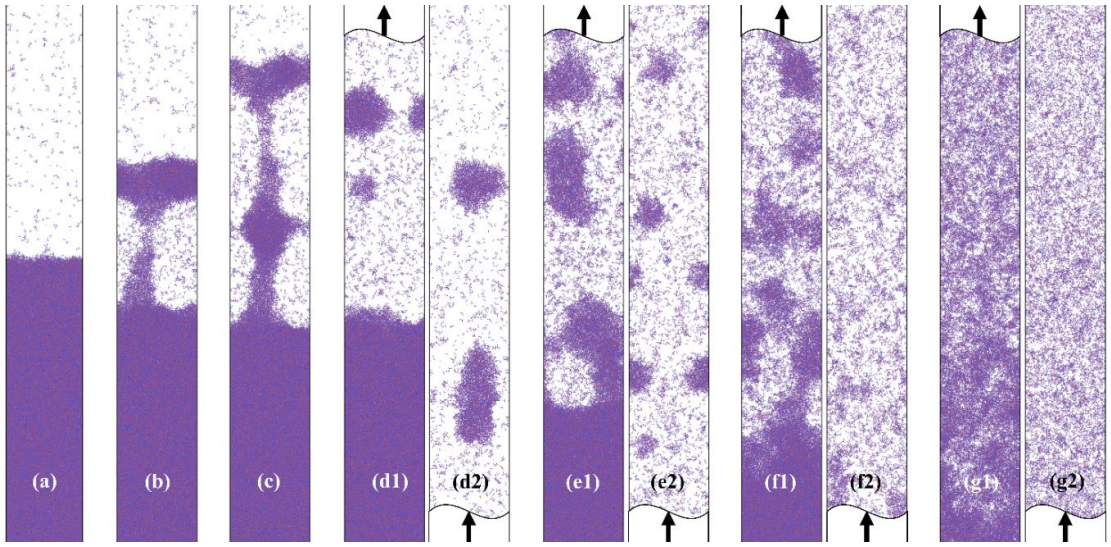

Figure 4.13 Atomic configuration of fused silica under 100 fs (FWHM) laser pulse irradiation at fluence of (a) 3.3 J/cm^2, (b) 3.5 J/cm^2, (c) 3.6 J/cm^2, (d) 4.0 J/cm^2, (e) 5.0 J/cm^2, (f) 6.0 J/cm^2, (g) 10.0 J/cm^2. (d) to (g) are segmented as two figures to represent the atomic distribution (1) close to the material surface and (2) upper part in the ablation plume plasma. Red and blue particles represent silicon and oxygen atoms, respectively.

As the laser fluence is further increased (4.0-6.0 J/cm^2), the material can be rapidly heated to temperature higher than the critical point. In this regime, thermal ablation would take over as the dominant mechanisms, covering phase explosion, CPPS, fragmentation and vaporization. The rapid heating process leads to formation of superheated liquid, which becomes metastable liquid during thermal relaxation. Due to the thermodynamic instability, the material can experience phase separation, resulting in a mixture of liquid droplets and vapors. As shown in Figure 4.12 (d) and Figure 4.13 (d)-(f), coexistence of liquid clusters and gas phase can be clearly observed in the ablation plume. Generally, due to increasing thermal effects, the liquid clusters will have sizes smaller than those in spallation. At the

fluence of 6.0 J/cm^2, transition from phase separation to vaporization becomes obvious in the ablation plume (Figure 4.13 (f)), especially in the topmost part. When the laser fluence reaches 10 J/cm^2, vaporization could play the dominant role in the generation of plume plasma. During vaporization, the material will undergo rapid heating towards temperature much higher than the critical point, and follow the ideal-gas isentropes during thermal relaxation. Under the high energy exceeding the cohesive energy, the material could experience complete dissociation, so that large- and moderate-size clusters can be barely found in the plume, instead, monomers and tiny-size nanoparticles become the dominant composition, as shown in Figure 4.13 (g).

To better understand different mechanisms of material decomposition, especially thermal ablation, detailed thermodynamic trajectories are investigated to represent material phase transition. As shown in Figure 4.14 and Figure 4.15, the evolution of material phase states is depicted in the temperature-density (T-ρ) phase diagram for selected clusters and particles at laser fluence of 4.0 and 10 J/cm^2. The critical point, binodal and spinodal curves of fused silica are determined with the method proposed in [98] including a serial simulation in canonical (NVT) ensemble to obtain isotherms on the pressure-volume (p-v) phase diagram. The critical temperature (T_c) and density (ρ_c) of fused silica based on CHIK potential have been determined as 6500 K and 0.65 g/cm^3, respectively. Fair agreements can be obtained compared with previous studies as T_c=6303 K [133], 6074 K [134], and ρ_c=0.66 g/cm^3 [135], 0.65 g/cm^3 [133,136], indicating proper determination of critical status for fused silica based on CHIK potential.

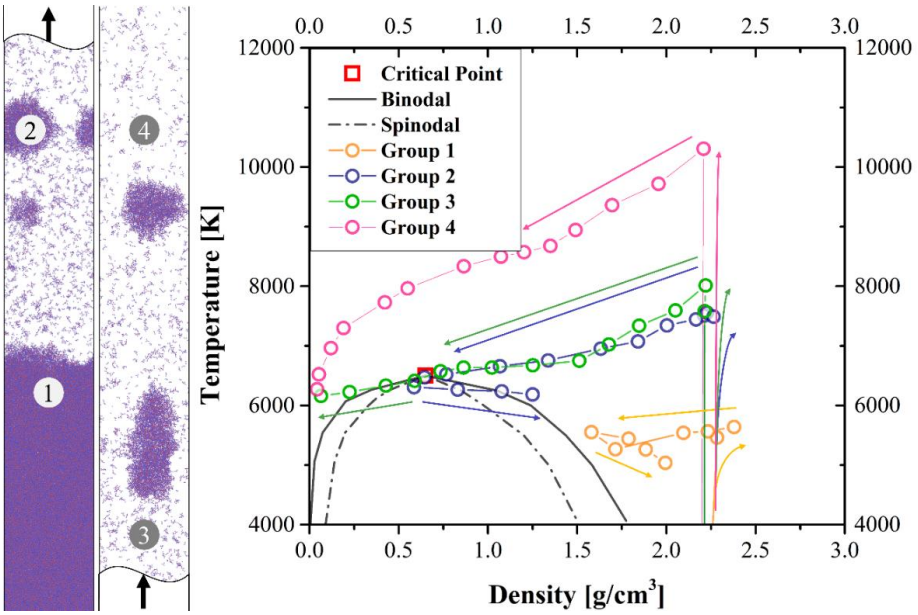

Figure 4.14 Thermodynamic trajectories of different atom groups in atomic configuration of fused silica under 100 fs (FWHM) laser pulse irradiation at fluence of 4.0 J/cm^2. Red and blue particles represent silicon and oxygen atoms, respectively.

At 4.0 J/cm^2, four atom groups are chosen as marked in Figure 4.14 along with their temperature-density evolution. For Group 1, which is close to the surface of unablated part, the material is heated to temperature below the critical point. The density can be reduced to as low as ~1.5 g/cm^3 during thermal expansion, and recovered as the material cools down, indicating the process from melting to resolidification. Group 2 and 3 represent phase separation in the ablation plume, where the local material is initially heated to temperature higher than the critical point. During the thermal relaxation process towards the critical point, there are no considerable differences in their thermodynamics trajectories. However, when the material approaches the critical point and enters the metastable zone, phase separation can be initiated under thermodynamic instability. Part of the material can

nucleate into liquid phase (Group 2), while the remaining material will continue to the gas phase (Group 3), although their initial location and thermodynamic history are close to each other. This material phase separation process represents the aforementioned CPPS. Similar phenomena can be observed in other phase separation processes (phase explosion and fragmentation), and the trajectories can follow paths slightly below or above the critical point. As for Group 4, the temperature can be raised much higher (above 10000 K) than the critical point, and the material will enter into the gas region before it can be cooled down below the critical point, representing the vaporization process.

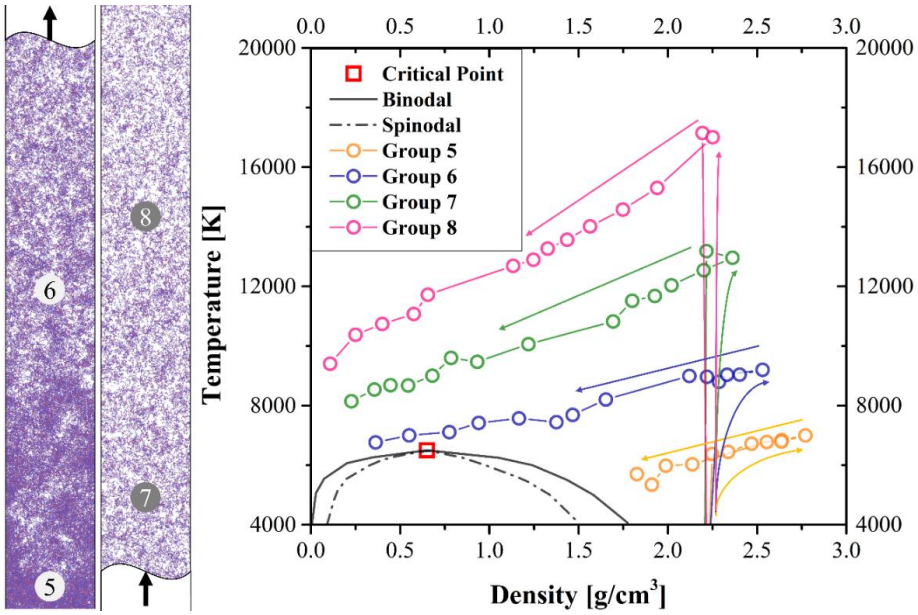

Figure 4.15 Thermodynamic trajectories of different atom groups in atomic configuration of fused silica under 100 fs (FWHM) laser pulse irradiation at fluence of 10.0 J/cm^2. Red and blue particles represent silicon and oxygen atoms, respectively.

As for 10.0 J/cm^2, four groups are selected in Figure 4.15, denoted as Group 5-8. In this regime, phase separation can be rarely observed because most of the material can

be heated to temperature much higher than the critical point and vaporization can take over as the dominant process. For Group 6-8, basically, the thermodynamics trajectories are similar, undergoing direct vaporization. For Group 5, which is close to the top of unablated material, the temperature is not raised above critical point, and the final state is close to the liquid phase. Similar to Group 1, Group 5 will undergo thermal relaxation and resolidification in a longer period. One noticeable change is that the material can be initially densified much more significantly to a density of ~2.8 g/cm^3 before thermal or mechanical relaxation, which is mainly because of the much higher compression (~30 GPa) under high fluence compared with lower fluence (<5 GPa). This densification could lead to formation of structural deformation, bond breaking and defects surrounding the ablation craters [93,137,138].

Different ablation mechanisms, including non-thermal and thermal ablation, can be captured during ultrafast laser interaction with dielectric materials (fused silica). Different mechanisms dominate in different regimes of laser fluence. At laser fluence in vicinity of the threshold, spallation is the dominant ablation process, accompanied with ejection of material layers and large clusters. With the increase of laser fluence, material will undergo thermal decomposition, dominated by phase separation processes (phase explosion, CPPS and fragmentation), introducing mixture of liquid droplets and gas phase in the plume. At even higher laser fluence, vaporization process becomes increasingly dominant. With much higher laser energy input, more material will undergo dissociation, forming tiny-size nanoparticles and monomers.

4.2.3 Spallation

It has been studied and believed that spallation occurs during ultrafast laser interaction with metals and semiconductors in a certain range of laser fluence. However, there is still no direct observation regarding the occurrence of spallation in dielectric materials under ultrafast laser pulses. Recently, there has been indirect experimental observation of spallation in dielectric materials based on optical microscope from pump-probe measurements [139–141]. In this section, based on the simulation results, detailed material responses during interaction with ultrafast laser pulse will be illustrated, and consistence with experimental observations will be demonstrated.

Based on the simulation results in Section 4.2.2 (Figure 4.12 (b) and Figure 4.13 (b)), it can be observed at laser fluence in vicinity of the threshold that large-size cluster or whole layer of material can be ejected from the sample, which is closely related to the occurrence of spallation. So far, it has been widely studied and believed that spallation occurs during ultrafast laser interaction with metals [5,7,97] and semiconductors [142] resulted from mechanical decomposition by shock wave generation and propagation. However, there is still no direct theoretical evidence to demonstrate whether and how spallation happens during ultrafast laser interaction with dielectric materials.

The occurrence of spallation is closely related to tensile stress, which is expected to surpass the local spall strength on the breakdown of material. However, it remains unexplored about the time period required for the tensile stress to overcome the material strength, and how the material strength can be affected by temperature and strain rates, etc. In addition, as an ultrafast process, laser ablation is highly complicated, making it difficult

to be well understood about the material decomposition process, especially how the spall strength competes with tensile stress on the occurrence of spallation. Therefore, a dimensionless quantity is proposed to capture the occurrence of spallation as tension factor, which is defined as the quotient between the stress and the tensile strength. The unified critical condition for spallation is the local tension factor greater than 1.0, indicating stronger tensile stress than local material strength at the instant strain rate. The calculation of tension factor is closely related to the measurements of tensile strength, which is tabulated based on separate MD tensile tests with wide range of temperature and strain rate, selected as the most influential quantities, as shown in Figure 4.10 (Section 4.2.1). There has also been the measurement of material strength in the flyer-plate [85,106] or piston-driven shock wave [115,143], however, not preferable for our current study. On one hand, the dynamic properties, such as temperature, strain rate, and spall strength, are measurable but not directly and precisely controllable. On the other hand, the generation of shock wave needs large simulation domain, which will significantly increase the computational cost. Both concerns make the direct tensile test on supercell preferable for buildup of reference tensile strength.

The distribution of tension factor provides a direct way to monitor the occurrence of spallation and to validate the proposed spallation criterion. As shown in Figure 4.16 and Figure 4.17, evolution of pressure and tension factor are depicted for laser fluence of 3.3 J/cm^2 and 3.5 J/cm^2 (threshold), respectively. Generation of rarefaction wave is close to the material surface, and the strength will develop along with propagation into the material. The maximum tension factor is marked in the tension factor distribution. As shown in

Figure 4.16 (b), at fluence of 3.3 J/cm^2 below the threshold, the generation of shock wave as well as the rarefaction wave is not strong enough to decompose local materials, which can be revealed by the tension factor (0.83) below 1.0. Based on the proposed critical condition, absence of spallation can be predicted, which is consistent with the density distribution (Figure 4.12 (a)) and atom configuration (Figure 4.13 (a)). When the laser fluence is raised to 3.5 J/cm^2, spallation has been observed to occur at the surface, as shown in Figure 4.12 (b) and Figure 4.13 (b). On one hand, increasing energy deposition at higher fluence will enhance the temperature, especially close to the surface, so that local material strength can be reduced. On the other hand, higher temperature will strengthen the shock wave, so as to increase the strength of rarefaction wave (tensile stress). Both factors drive the occurrence of spallation at this fluence, which is consistent with the satisfaction of critical condition that the maximum tension factor (1.04) is greater than 1.0. Based on this, the occurrence of spallation can be well predicted and corroborated by whether the local tension factor can surpass unity, so that the proposed tension factor and spallation criterion have been evidenced as a proper manner to monitor spallation during ultrafast laser interaction with dielectric materials.

Tension factor, as a dimensionless variable, helps to unify the spallation criterion instead of the spallation strength, which could be considerably affected by the materials, interatomic potentials, temperature and the strain rate on the occurrence of spallation. Noticeable differences can be observed when comparing spallation strength from different works, even for same material and interatomic potential. For laser simulation of gold, the spall strength is measured as ~14 GPa, which could be over 20% higher than that from [94]

as 11.6 GPa. This difference should be mainly attributed to different temperature and strain rates at the location of spallation. Though this inconsistence has been observed for metals (gold) and spallation in the solid phase, it is believed that spall strength itself provides much weaker evidence on capturing the occurrence of spallation, compared with the proposed tension factor in this study.

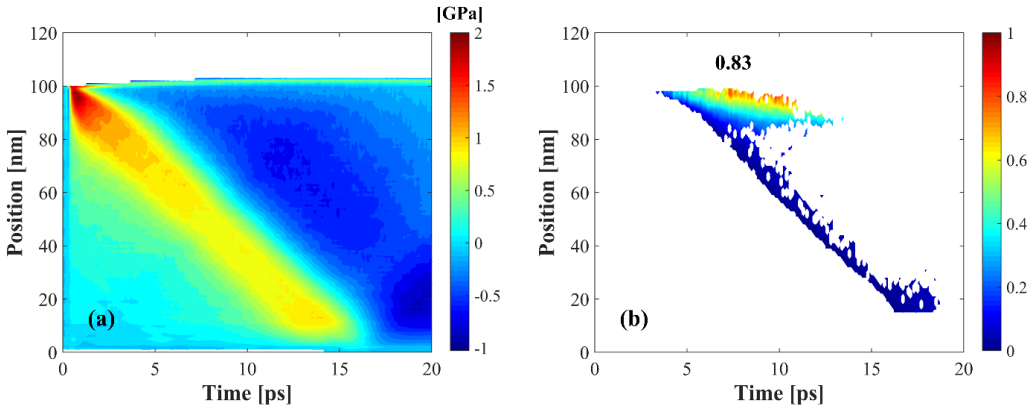

Figure 4.16 Evolution of pressure and tension factor distribution with time at laser fluence of 3.3 J/cm^2.

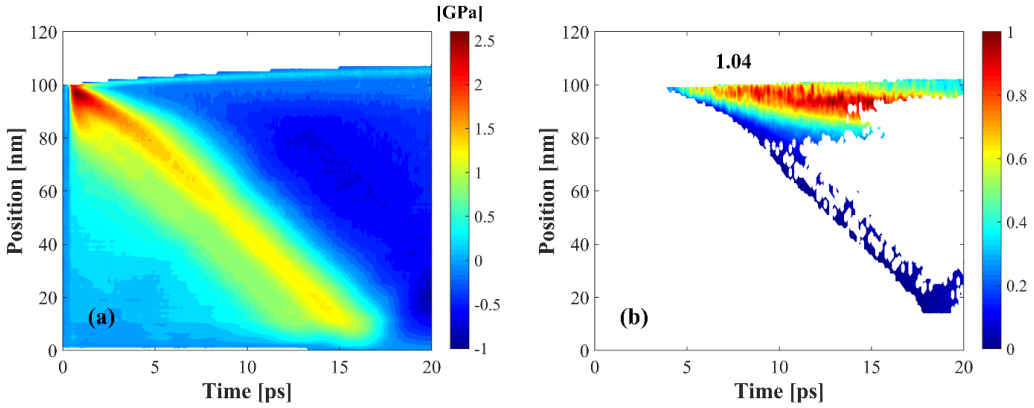

Figure 4.17 Evolution of pressure and tension factor distribution with time at laser fluence of 3.5 J/cm^2.

So far, the occurrence of spallation has been clearly demonstrated based on MD simulation, and the underlying physics of spallation has been demonstrated by monitoring of shock wave generation and propagation as well as the evolution of tension factor. Simulation results in this study can not only corroborate recent experimental observations regarding ultrafast laser ablation in dielectric materials, but more importantly, help to explore and understand the underlying physics on experimental observation about spallation in dielectric materials.

Newton rings has been observed [139,140] with femtosecond laser pump-probe method in dielectric materials, and has been attributed to ultrafast laser-induced spallation process with generation and expansion of thin shell. These indirect experimental observations can be well corroborated by MD simulation, and the ejection of thin-layer material has been clearly demonstrated during material decomposition and expansion. Our simulation results provide theoretical evidence that dielectric material can have similar thermodynamic trajectories as in metals and semiconductors at the irradiation of ultrafast laser pulses, where non-linear absorption and extensive ionization does not prevent the material cross the liquid-gas coexistence regime [139]. Meanwhile, the indirect experimental observation of spallation in dielectric materials (fused silica in [141]) can validate our simulation results on the occurrence of thermal-mechanical responses in dielectric materials.

Furthermore, the time scale of material spallation process matches fairly with experiments. As seen from the simulation (Figure 4.12 (b) and Figure 4.17), the generation of rarefaction wave and the initiation of spallation (tension factor greater than 1.0) are

located within 20 ps, while the material expansion and disintegration extends beyond 100 ps, indicating an aforementioned non-instant process during spallation. This numerically predicted time scale from MD simulation agrees well with those from experiments, where the formation of rarefaction wave is induced within tens of picoseconds, and ejection of thin shell can be completed at delays in the order of 100 ps [139]. In addition, rarefaction wave propagation has been indirectly estimated during the experiments, indicating a fluence independence speed close to the value of sound speed in the material with acceptable accuracy. This is also true during MD simulation, and the speed can be more directly and accurately predicted. As shown in Figure 4.16 and 4.17, the period of pressure wave propagation through the 100 nm-thick fused silica material is approximately ~17 ps, so that the calculated pressure wave speed is ~5.88 km/s, quite close to the experimental longitudinal sound speed (5.90 km/s) for fused silica.

Spallation, as well as Newton rings in dielectric material at ultrafast laser irradiation happens within a certain range of fluence. As demonstrated by the simulation results, the occurrence of spallation starts from the threshold fluence. Spallation and thermal ablation coexists in the ablation of dielectrics. Phase separation can be clearly observed within a certain fluence regime (3.5-5.0 J/cm^2) and thermal ablation takes over as the dominant mechanism with the increase of laser fluence. Meanwhile, spallation becomes decreasingly noticeable with the decrease of rarefaction wave due to strong recoil pressure in the plume. With more uniform distribution of small-size nanoparticles instead of large clusters, the Newton rings can be barely observed, resulted from the absence of clear and abrupt interface between liquid phase and gas phase. This is also similar to metals and

semiconductors, where coexistence of non-thermal and thermal processes, and the dominance of thermal ablation at high fluence range have been clearly demonstrated. However, as dielectric materials have much longer optical penetration depth (~100-200 nm) than metals (~10 nm) at 800 nm laser irradiation, non-linear absorption has to precede material heating, and the temperature gradient can be much lower, so that the generated thermal-elastic stress is much weaker than in non-transparent materials at similar level of surface heating.

Finally, current simulation results help to reveal unsolved phenomena during experiments. As mentioned in [140] double-layer ejection of material can be observed in the experiments, which has been suspected as fragmentation of the main ablation layer into two sub-layers. Whereas based on the simulation results from Figure 4.12 (c) and Figure 4.13 (c), it is clearly demonstrated that, on the occurrence of double-layer spallation, the two discrete spalled layers are not formed by decomposition from a thicker layer, but formed sequentially along with the propagation of rarefaction wave. This is similar to the study of spallation in metals, where multiple spallation can happen when the strength of rarefaction wave is above the threshold value. Meanwhile, based on the trajectory of spalled layer position, difference in the ejection speeds of two layers is noticeable, as discussed in the experiments [140].

Simulation in this study opens the door to theoretical evidences in ultrafast laser interaction with dielectric materials. Experiments corroborate the observations and mechanisms demonstrated in the simulation. Although the studied material is fused silica, the SRE-TTM-MD combined modeling provides a novel method to explore material

decomposition during ultrafast laser interaction with dielectric materials, especially spallation, and dynamics of material ejection processes.

4.2.4 Plasma dynamics

In this section, we combine experiments and MD simulation to study material ejection dynamics by ultrafast laser irradiation on dielectric material (fused silica), covering nanoparticles ejection velocity and direction in the ablation plume.

The direction of plasma ejection is critical to determine the process of plasma redeposition, particularly important for micromachining. To study plasma ejection direction, we use fluorescence to capture plasma shape evolution in tens of nanoseconds. Fluorescence is triggered by spontaneous photon emission in single pulse ablation on glass surface and imaged by ICMOS camera, which has an exposure time as short as 2 ns. The evolution of plasma ejection is shown in Figure 4.18 and the color of plasma can reflect the temperature and density of plasma.

In this way, we capture the plasma ejection whole process at three selected laser fluence. Great similarity can be observed for different laser fluences and the plasma florescence at high fluence is much stronger than low fluence. Also, during ejection, the central part has denser and hotter plasma than the edge, so that the kinetic energy and ejection velocity is faster. Therefore, the plasma shape becomes umbrella shape at 10 ns.

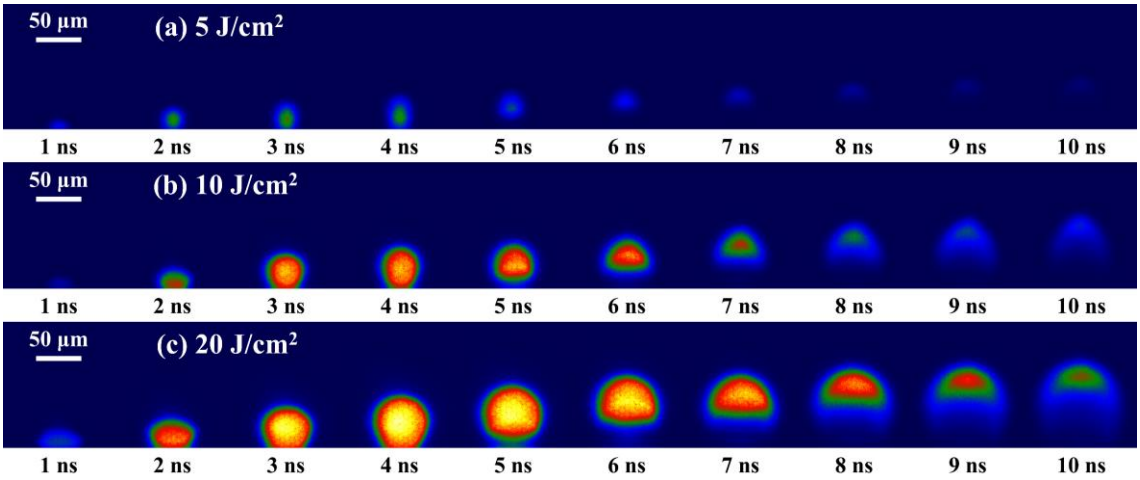

Figure 4.18 Evolution of plume plasma by fluorescence measurement. Target material: fused silica, pulse duration: 190 fs, wavelength: 1030 nm, and laser fluence: (a) 5 J/cm^2, (b) 10 J/cm^2 and (c) 20 J/cm^2.

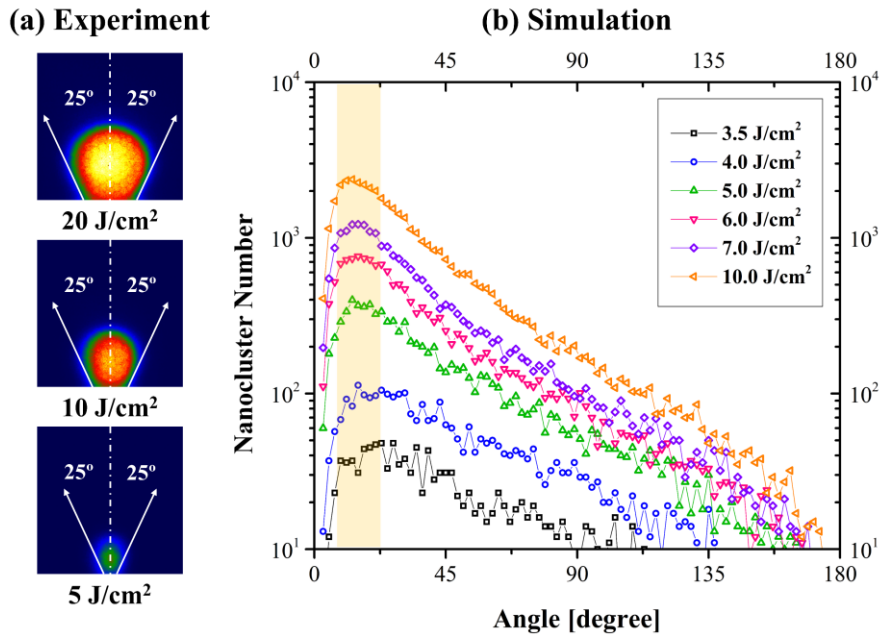

Figure 4.19 Comparison of plasma ejection angle between (a) measurements by fluorescence images and (b) prediction by MD simulation. The peak of angle spectrum is highlighted by orange color.

The ejection direction of plasma is measured from fluorescence and the statistics of nanoparticle ejection direction is plotted in Figure 4.19. The ejection direction of nanoparticle is defined as the angle between velocity vector and the normal direction of surface. The number of nanoclusters increases significantly at angle in vicinity of 20-25°, and follows approximately exponential decrease with increasing angle. This is in good agreement with measurements in fluorescence, where the majority of plasma are ejecting in the direction within 25° with respect to the normal direction. Also, it is found that the most probable direction (angle) is not significantly affected by the laser fluence. This indicates that plasma deposition process is not sensitive to laser fluence/energy.

Due to the limitation of camera exposure time, florescence cannot be used to capture early stage plasma to study ejection dynamics within nanosecond. On this aim, shadowgraph images will be used, which has a much higher temporal resolution in picosecond level.

We capture the early-stage plasma ejection at the selected laser fluences from hundreds of picoseconds to 4 ns to demonstrate the ejection process from just above surface to a well-developed hemispheric shape, as shown in Figure 4.20. Great similarity can be observed for different laser fluences as well and the plasma ejection at high fluence is much faster than low fluence due to higher temperature.

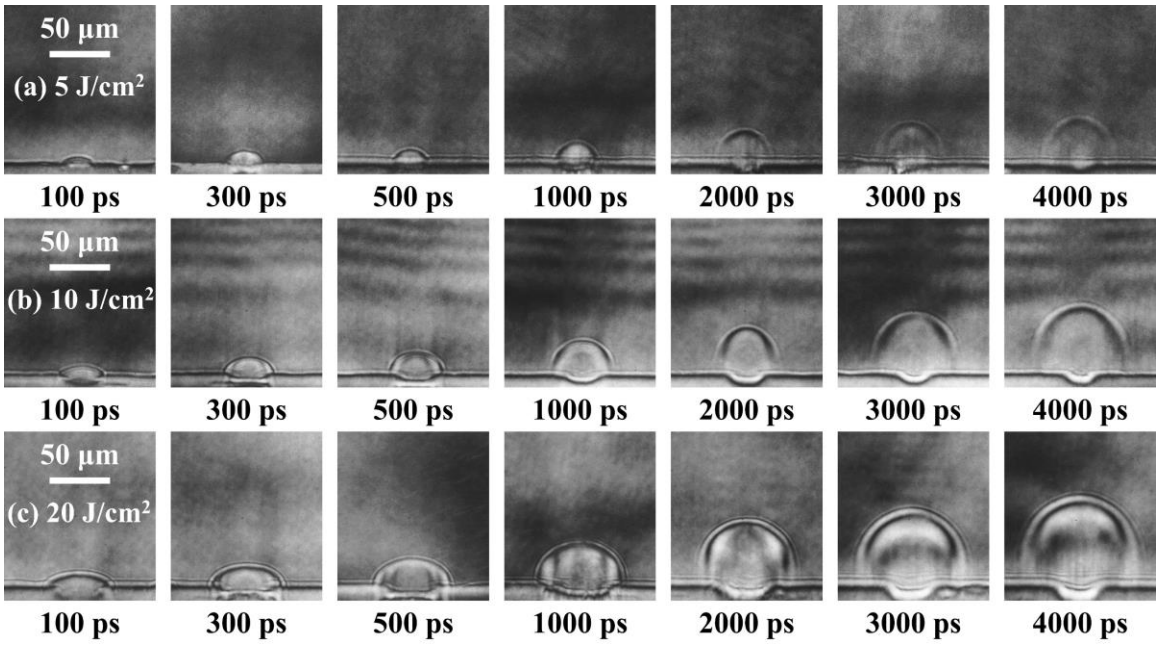

Figure 4.20 Evolution of early plasma by shadowgraph measurement. Target material: fused silica, pulse duration: 190 fs, wavelength: 1030 nm, and laser fluence: (a) 5 J/cm^2, (b) 10 J/cm^2 and (c) 20 J/cm^2.

The plasma ejection velocity is measured by shadowgraph images. The evolution of velocity is plotted in Figure 4.21. A clear decreasing trend with time is observed for plasma, which is mainly resulted from attenuation of plasma kinetic energy by scattering with gas molecules in air. The ejection velocity is closely related to plasma temperature and laser fluence and the measured peak velocity is compared with prediction from MD simulation. As shown in Figure 4.21, the normalized velocity at different laser fluences from measurements agrees well with the scale of the root of electron temperature. This unveils the fidelity of this computational model and highlights the dominating role of thermal ablation in dielectric materials.

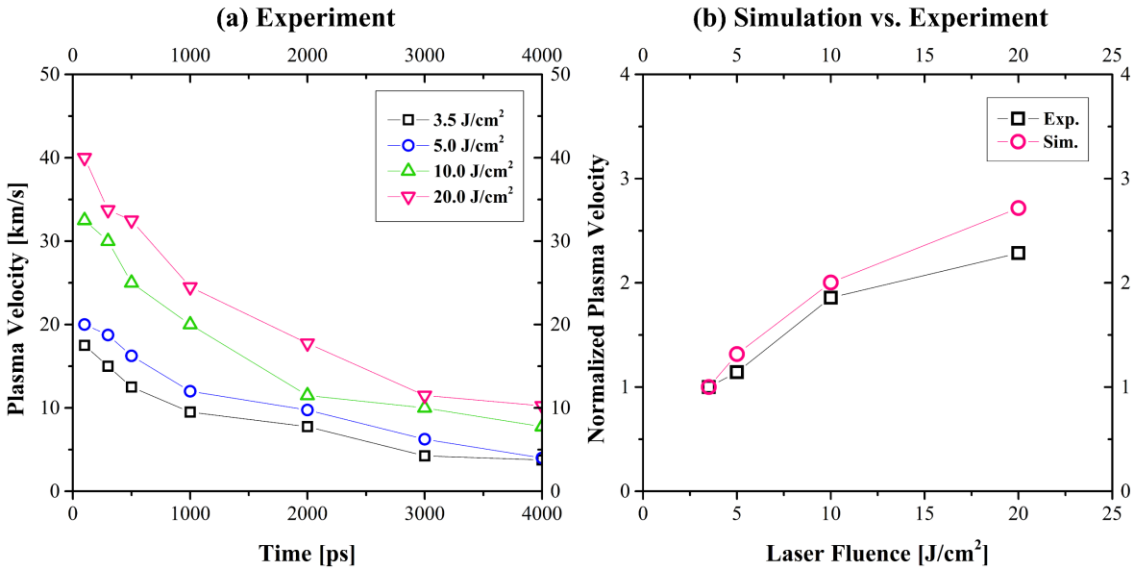

Figure 4.21 Comparison of plasma ejection velocity between (a) measurements by shadowgraph images and (b) prediction by MD simulation.

4.3 Summary

Thermal and non-thermal (photomechanical) behaviors in micro-size metal films from irradiation of ultrafast laser pulse have been investigated based on combined continuum-atomistic approach, including phase explosion (thermal ablation) and spallation (non-thermal ablation).

Coexistence of phase explosion and spallation has been observed for a considerably wide range of laser fluence, revealing the complicated interplay of different mechanisms in ultrafast laser-induced material decomposition. Phase explosion has higher threshold fluence than spallation, and becomes the dominating ablation mechanism with the increase of laser fluence.

Spallation can be induced on both the front side and the rear side of the metal film, where large-size nanoparticles are ejected in liquid and solid phase, respectively. A dimensionless quantity, tension factor, has been introduced, based on which a universal criterion for the occurrence of spallation has been proposed and validated. This dimensionless factor and the accompanying criterion, compared with spall strength, provides a better description of the underlying mechanism of spallation and facilitates further studies on mechanical behavior in material.

The spall strength, as the threshold stress to trigger spallation, is well comparable to the separately measured tensile strength, where temperature and strain rate have been considered as the most influential factors. The tensile (spall) strength follows linear decrease with the increase of temperature below melting point, and the inverse exponential function can better agree with our measured strength in the liquid regime compared to previously proposed theoretical descriptions.

At higher laser fluence over 0.5 J/cm^2, reduction in the spall strength can be observed, which should be mainly attributed to the structural deformation from the compressive process prior to the material breakdown under tension. With increasing shock compression above HEL (~30 GPa), stacking faults form and become densified and intersected approaching ~40 GPa. Twinning faults appear and coexist with stacking faults at ~50 GPa and becomes the dominating structural defects above ~60 GPa. Formation of stacking faults serves as the dominating mechanism for spall strength decrease by ~15%, while formation of twinning faults is responsible for material re-strengthening (~10%). Spall strength saturates with increasing presence of twinning above ~60 GPa, reaching

ultimate value at 95% of the strength in pristine material. This “valley-shape” pattern in spall strength with respect to compressive pressure and its interrelation with structural transformation has been corroborated by QI simulations. This study highlights the impacts of structural transformation by shock compression on spall strength and unveils the “self-healing” role of twinning in spallation.

An SRE-TTM-MD combined model has been further developed to investigate ultrafast laser interaction with dielectric materials and material decomposition process in a wide range of laser fluence. Dielectric material decomposition mechanisms are essentially similar to metals and semiconductors, where coexistence of non-thermal and thermal processes, and the dominance of thermal ablation at high fluence range are clearly demonstrated. However, since dielectric materials have much longer optical penetration depth (~100-200 nm) than metals (~10 nm) at 800 nm laser irradiation, non-linear absorption has to precede material heating, and the temperature gradient can be much lower, therefore the generated thermal-elastic stress is much weaker than in non-transparent materials at similar level of surface heating.

Plasma dynamics is further studied combining computational model and in-situ imaging. Fluorescence and shadowgraph images are captured to measure plasma ejection direction and velocity, respectively. Good agreements have been obtained between model predictions and measurements. It is found that the most probable direction (angle) is not significantly affected by the laser fluence, indicating the plasma deposition process insensitive to laser fluence/energy. The plasma ejection velocity scales pretty well the root

of electron temperature, indicating the dominance of thermal ablation in dielectric material decomposition by ultrafast laser irradiation.

CHAPTER FIVE

ULTRAFAST LASER ABLATION OF DIELECTRIC MATERIALS

Ultrafast laser ablation of dielectric materials has been studied based on a plasma-temperature combined model, as introduced in Chapter 3. Temperature evolution is captured to describe the evolution of ablation depth, where a temperature-based ablation criterion is employed and dynamic description of material removal is incorporated for the consideration of thermal energy losses through ablation. Characteristics of ablation have been investigated, covering laser-induced ablation threshold, optical properties, ablation depth, beam divergence effect, plasma defocusing effect in air and thermal accumulation effect. Details regarding numerical and experimental observations are described in the following sections.

5.1 Temperature evolution inside bulk material

The electron and lattice temperature evolution in the bulk material can be predicted by the proposed model. With a 190 fs, 1028 nm laser pulse at 6 J/cm^2, the calculated temperature evolution in fused silica is shown in Figure 5.1. The electron temperature experiences fast increase within the pulse duration. As for the lattice, much slower increase of the temperature can be observed. When the lattice temperature reaches the vaporization temperature, the material ablation is considered to take place. The ablated materials will be removed from the simulation domain, and thus there is no further heat transfer between the ablated material and the remaining part. Before the lattice reaches thermal equilibrium with the electron, continuous temperature increase will happen in the lattice through electron-

phonon coupling, and more materials will be ablated until the surface temperature of lattice is no longer higher than the ablation criterion. The evolution of ablation depth is tracked by the coloured surface in Figure 5.1 (b), and the final value will be treated as the final depth of the crater.

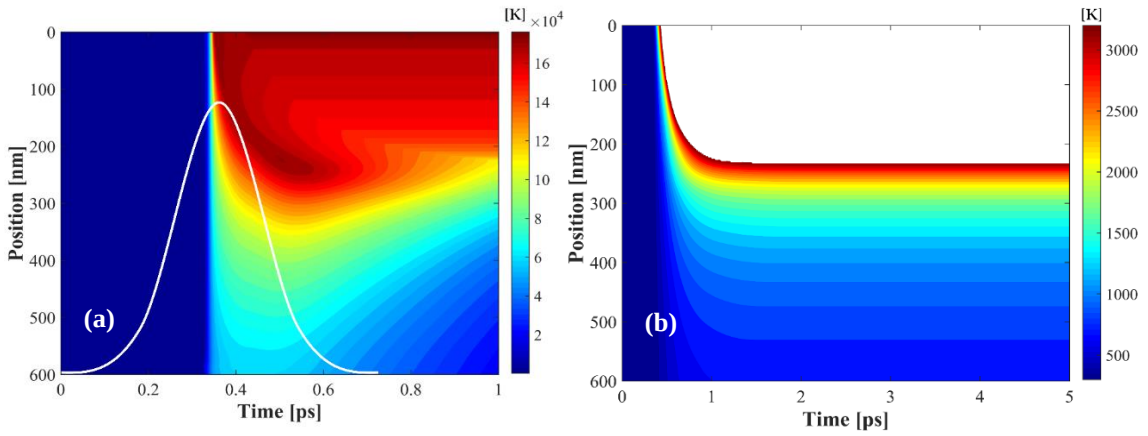

Figure 5.1 Temporal evolution and spatial distribution of (a) electron and (b) lattice temperature in fused silica with a 6 J/cm^2, 190 fs, 1028 nm single pulse. The solid line in (a) represents the Gaussian-shaped laser intensity profile.

5.2 Laser-induced ablation threshold

Laser-induced ablation threshold (LIAT) of fused silica has been determined through the temperature-based criterion. The dependence of LIAT on pulse duration has been numerically predicted and compared with experimental measurements, as shown in Figure 5.2. Good agreement between numerical and experimental results can be observed. Scaling law of LIAT can be studied and piecewise linear fitting is applied for three regions. In the region of below 40 fs and above 10 ps, the slope is close to 0.5 so that the law of

$F_{th} \propto \sqrt{\tau_p}$ can be applied, as has been observed in [25,144]. As for the middle region, an index of 0.216±0.008 has been obtained in the scaling law of $F_{th} \propto \tau_p^{\alpha}$. The linear fitting applied on the whole range gives an overall index of 0.290±0.013, which is in excellent agreement with the observation in [129] as 0.33±0.01. Based on this, the predicted LIAT and the scaling laws for dielectric materials agrees well with experiments in the literature.

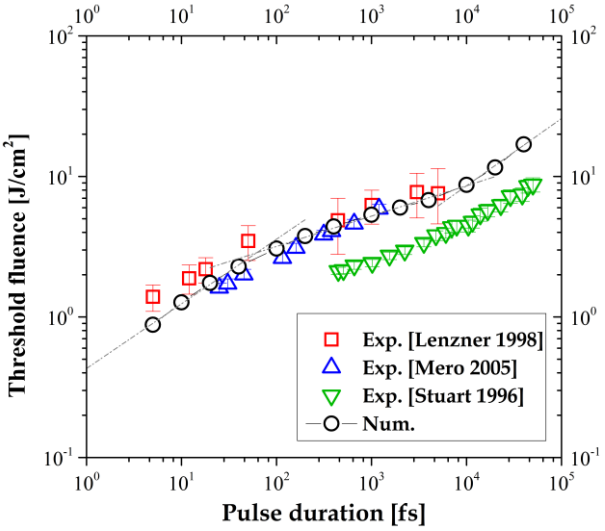

Figure 5.2 Ablation threshold of fused silica with pulsed laser irradiation at 780 nm.

The numerical prediction matches the trend of variation well with experiments in [25,144], however, homogeneous discrepancy in magnitude can still be observed. The great difference between numerical results and experiments in [25,144] should be attributed to the incubation effects [73,145], which is induced by thermal accumulation under multi-pulse laser irradiation. LIAT can be also affected by band gap [31,129], laser wavelength [25], and operations, as has been studied in [146].

The aforementioned incubation effect has been experimentally investigated. To determine the laser-induced ablation threshold (LIAT), the linear regression method [146,147] has been widely applied based on measurement of ablation crater diameter. The linear relationship between the square of crater diameter (D^2), and the logarithm of the pulse energy E or peak fluence F ($F = 2E / \pi\omega_0^2$), is given as

$$D^2 = 2\omega_0^2 \ln\left(E / E_{th}\right) = 2\omega_0^2 \ln\left(F / F_{th}\right) \tag{5.1}$$

where ω_0 is the laser beam radius at focal spot, E_{th} and F_{th} are the ablation threshold pulse energy and fluence, respectively. The dependence of D^2 on pulse energy is shown in Figure 5.3 (a) for 1, 10, and 100 pulses. The focal spot radius (ω_0) has been extracted by the slope as 24.4±1.4 μm. The LIAT can be obtained by extrapolating the linear regression to $D^2 = 0$, and the results are collected in Figure 5.3 (b) for pulse number up to 1000. The decrease of LIAT can be clearly seen with the increase of pulse number (N), from 3.72 J/cm^2 (N=1) to ~1.5 J/cm^2 (N=100). The LIAT remains as a constant level for pulse number over 100. The reduction of LIAT with multiple laser pulses irradiation is due to the incubation effects [148–151], and can be described by the following expression [150],

$$F_{th,N} = F_{th,\infty} + \left(F_{th,1} - F_{th,\infty}\right) e^{-k(N-1)} \tag{5.2}$$

where $F_{th,1}$, $F_{th,N}$, $F_{th,\infty}$ represent the threshold fluence for 1, N, and infinite number of pulses, respectively, and k is the incubation coefficient to characterize the strength of damage accumulation. Instead of the incubation model $F_{th,N} = F_{th,1} N^{S-1}$ [152] for metals, Eq. (5.2) considers the saturation of threshold for large pulse number, and can better describe the incubation in LIAT for dielectric materials.

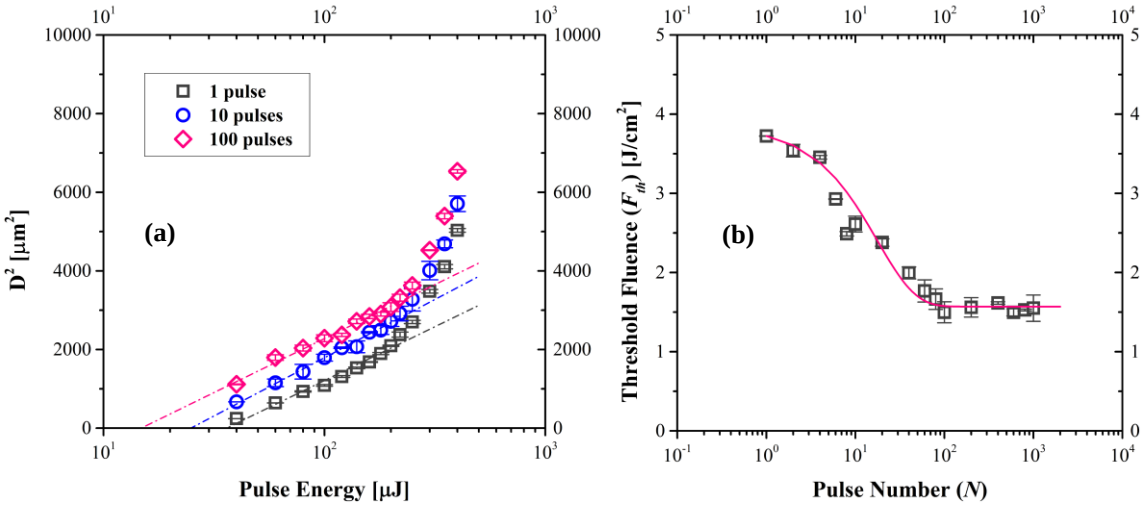

Figure 5.3 (a) Measurement of D^2 as a function of incident pulse energy and (b) threshold fluence as a function of pulse number. The dash-dot lines in (a) represents the linear relationship in Eq. (5.1), and solid line in (b) represents the fitting curve by Eq. (5.2).

Using Eq. (5.2) to fit the measurement of LIAT with different pulse number, good agreement can be obtained between the model prediction and experimental results, as depicted in Figure 5.3 (b). The constant level of LIAT indicates saturation of threshold reduction, which should be related to the low density of CBE excitation and its fast relaxation in fused silica, so that no considerable accumulation behavior (electronic and thermal) can be induced for the damage. This ultimate LIAT can be further decreased with shortened pulse interval comparable to the life time of CBE in fused silica [27].

5.3 Optical properties

The evolution of free electron number density excitation in fused silica for a 6 J/cm^2, 120 fs, 800 nm single pulse is shown in Figure 5.4 (a). The total number density of excited free electrons from MPI and AI is compared with that from MPI alone, so that contributions

from MPI and AI can be estimated. As mechanisms of free electron excitation are compared and focused, the number density of electron relaxation is not shown in Figure 5.4 (a). The Gaussian-shaped profile of laser pulse intensity is also included in a normalized manner. MPI is a highly non-linear process and sensitive to the laser intensity, no obvious change of electron density can be seen until the central part of the laser pulse. During the first half pulse, MPI is the dominant mechanism of ionization, providing seeding electrons for the avalanche process, which plays a more important role during the second half pulse. Electron excitation tends to saturate for both processes due to the weak laser intensity during the pulse tail. Without consideration of electron relaxation in Figure 5.4 (a), the stable value in the dash line and the difference between two lines approaching the pulse end can be treated as the final contribution from MPI and AI, respectively.

It can be expected that with the increase of incident laser fluence (intensity), the rate of free electrons generation will increase accordingly. Given that avalanche process will take over to be the dominant excitation mechanism until sufficient seeding electrons have been obtained, earlier initiation and more contribution from avalanche process can be expected with higher incident fluence. As shown in Figure 5.4 (b), the quotient of the electron excitation from MPI to the total density has been collected for various incident laser fluence. The contribution from MPI decreases from below 10^{-2} at 4 J/cm^2, and tends to saturate at the level of ~10^{-8} approaching 24 J/cm^2, which can be attributed to excitation saturation from valence-band density limitation, and less effective energy deposition due to plasma shielding effects.

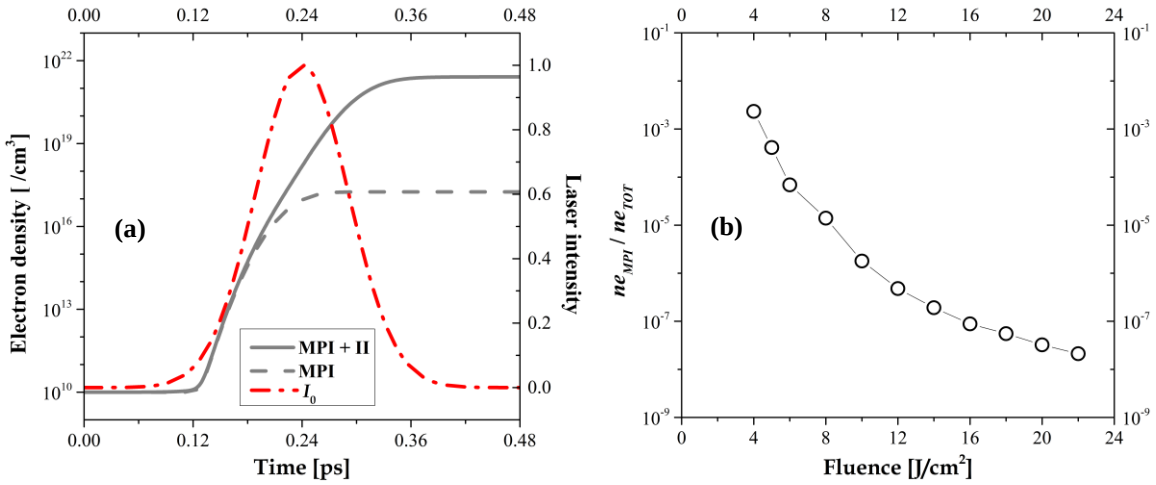

Figure 5.4 (a) Evolution of free electron excitation density within laser pulse duration at incident fluence of 6 J/cm^2 and (b) contribution of free electron excitation from MPI with various incident fluence.

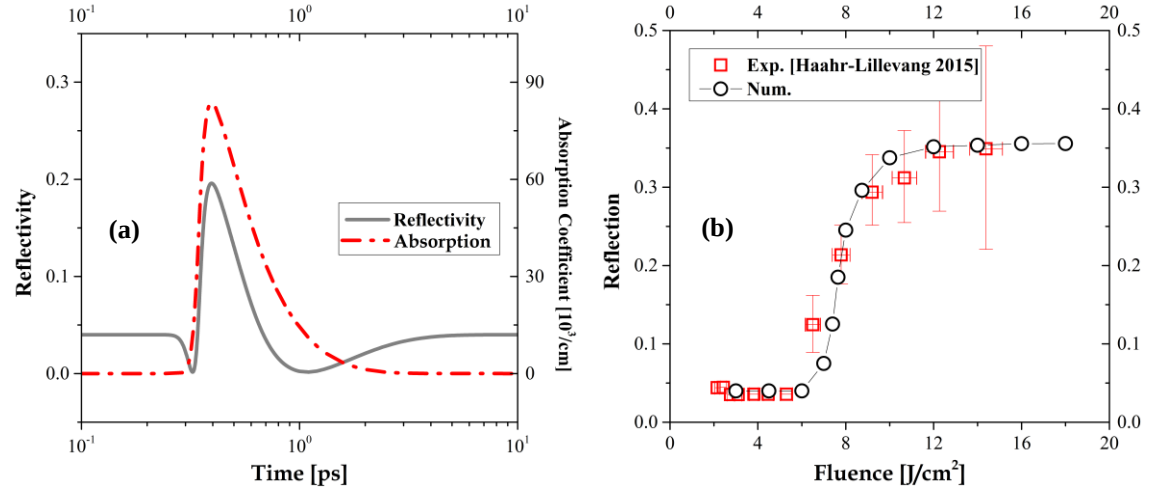

Figure 5.5 Variation of optical properties with (a) time (6 J/cm^2) and (b) incident fluence with laser irradiation of 120 fs, 800 nm single pulse.

The variation of the electron number density will affect the material optical properties. Figure 5.5 shows the evolution of surface reflectivity, and absorption coefficient, and reflection of silicon dioxide (quartz) with 120 fs, 800 nm single pulse irradiation. As shown in Figure 5.5 (a), the peak values in reflectivity and absorption coefficient are obtained when the free electrons reach the peak number density. While the absorption coefficient varies monotonously with the number density of free electrons, the surface reflectivity will first decrease with the electron number density, reaching the bottom around the critical electron density ~10^{21} cm^{-3}, and then increase quickly. After passing through the peak value, the reflectivity will decrease with the relaxation of free electrons, and then recover to the reflectivity in unexcited material until the completion of relaxation. Similar behavior in reflectivity variation has been observed during electronic excitation in dielectric materials [145], as well as semiconductors [24]. Figure 5.5 (b) displays the reflection of silicon dioxide with various incident fluence from both experimental measurements and numerical predictions. For fluence below the ablation threshold, no obvious variations of reflection can be seen, while for higher fluence, the reflection will increase quickly and tend to saturate in high fluence regime around 0.4 with 800 nm laser irradiation.

5.4 Laser-induced ablation depth

Laser-induced breakdown (LIB) and ablation (LIA) will be initiated when sufficient energy has been deposited onto the material through CBE excitation and absorption. As has been observed in Section 5.3, surface reflectivity will increase significantly at the

highly excited state. The increase of surface reflectivity, which reduces the effective laser energy deposition, plays an opposite role [24] to the energy absorption through inverse Bremsstrahlung. Though this plasma mirror effect exists, there is earlier strong absorption before the significant increase of reflectivity [153], leaving more space for fast energy deposition with higher fluence laser irradiation [154]. The heat losses taken away by the ablated material [155] has been considered in this model through the dynamic description of material removal.

Based on the plasma-temperature combined description of thermal response in dielectric materials to ultrafast laser pulses, ablation depth has been collected for various incident fluence in multi-case studies with near-infrared laser pulses. Ablation depths of silicon dioxide and aluminum oxide are displayed in Figure 5.6. Good agreement with experimental measurements has been obtained and similar behavior can be observed for these two different materials. No ablation craters can be observed for fluence below the LIAT in single-pulse measurements, though material densification and surface depression can be monitored [156], which is mainly resulted from laser-induced thermal shock wave [157]. Fast transition from gentle ablation regime to strong ablation regime can be observed with the increase of fluence around the threshold. The sharpness of ablation depth slightly above the threshold also indicates the non-linear feature during the complicated ULIA process. When incident fluence is further increased, no more steep increase in crater depth can be observed, and the ablation process tends to saturate, indicating a stable energy deposition efficiency in various fluences. The good agreements between numerical prediction and single-pulse experiments indicate capability of the numerical model to

capture major mechanisms in the complicated process of ULIA and give good prediction of crater depths.

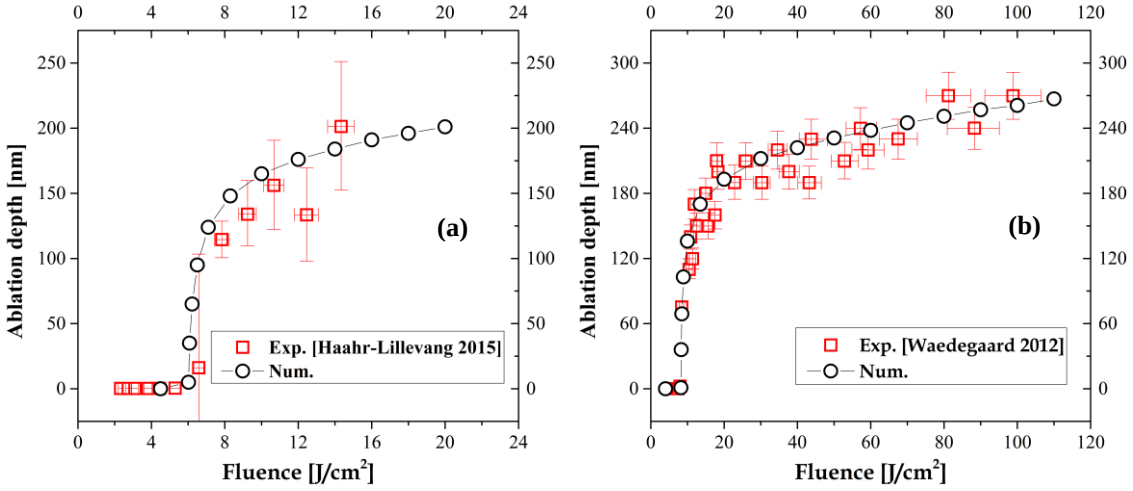

Figure 5.6 Ablation depth of (a) quartz, 120 fs, 800 nm and (b) sapphire, 160 fs, 795 nm with single laser pulse.

The experimental laser pulse durations shown in Figure 5.6 are within 200 fs, however, the numerical approach can capture ablation behavior for wider range of pulse duration. As shown in Figure 5.7 (a), the dependence of ablation depth on pulse duration is predicted at various incident fluence. For low incident fluence as 5 J/cm^2, the predicted ablation depth first experiences an increase from 5 fs, reaching the maximum value at ~40 fs, and then decreases until certain pulse duration, beyond which the ablation threshold will be higher than the incident fluence. This phenomenon has also been reported in [32], and a close value of pulse duration for peak ablation depth has been predicted as well. With higher fluence as 7.5 and 10 J/cm^2, similar trend of variation in ablation depth can be observed, with slightly longer pulse duration where peak ablation depth can be obtained.

Wider range of allowed operational pulse duration is obtained for higher incident fluence, due to the competition with local ablation threshold as well.

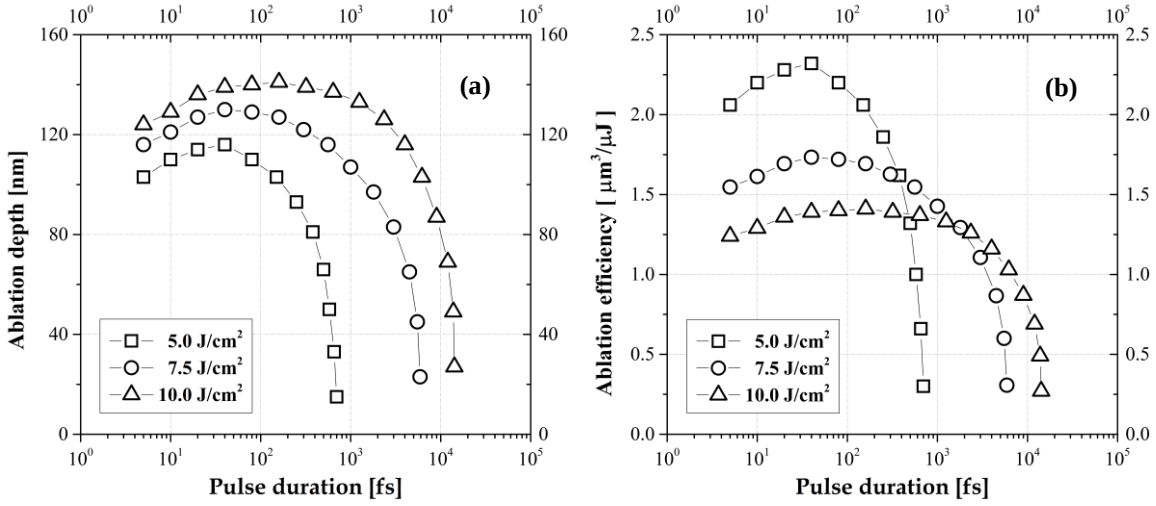

Figure 5.7 Dependence of (a) ablation depth and (b) ablation efficiency on pulse duration for various laser fluence.

Ablation efficiency is of great importance in laser micromachining, which has been calculated based on data in Figure 5.7 (a), as shown in Figure 5.7 (b). Ablation efficiency in experiments has been defined as the quotient of ablation volume and incident fluence [158], and the expansion of crater diameter with the increase of fluence [159] is neglected in this one-dimensional model. In the range of fluence from 5 to 10 J/cm^2, higher ablation efficiency can be obtained with lower incident fluence, resulted from the saturation of ablation depth in high fluence region. The decrease of ablation efficiency is observed to be initiated with a critical fluence around twice of the threshold [158,160], and for lower fluence than the critical value, ablation efficiency still experiences high-rate increase. A fluence range for efficient absorption has been defined in [160] where highly efficient

ablation can be obtained. In a similar approach, a pulse duration range can be defined for efficient ablation, and the criterion can be chosen as 80% of the maximum ablation efficiency. For low fluence as 5 J/cm^2, efficient ablation can be obtained within ~300 fs pulses. Wider range of pulse duration for efficient ablation is estimated to be ~1 ps and ~10 ps for higher incident fluence as 7.5 J/cm^2 and 10 J/cm^2, respectively. With even higher fluence, further wider range of pulse duration for efficient manufacturing can be expected, which will induce lower ablation efficiency for femtosecond laser pulses. In addition, manufacturing with high pulse energy will bring about more thermal damages, such as deteriorated entrance and side wall in microchannels, and cracks in brittle materials. For the overall consideration of ablation efficiency and microstructure quality, incident fluence in the range of 1-2 times of the threshold is proposed to be the healthy range in operation. The pulse duration range predicted with efficient ablation indicates the capability of the incident fluence, however, pulses in picosecond region are not widely employed in real cases due to the requirement of high pulse energy.

5.5 Laser beam propagation inside the material

With more tightly focused laser, the effects of beam divergence will increase in Gaussian-shaped beam propagation along the material. This effect has been generally neglected in the numerical description of ULIA. As shown in Figure 5.8 (a), ablation depth of silicon dioxide has been predicted for different numerical aperture (NA) at various incident fluence. The original data without considering this effect is included as reference.

Non-linear behavior can be observed that difference of the ablation depth at low fluence between different NA is less obvious than that at high fluence. Non-linearity can be also seen that the variation of ablation depth increases with NA. This is mainly related to the non-linear process of electron excitation, and the energy absorption will display certain non-linear behavior accordingly. In addition, the local intensity along with beam propagation will decrease in a non-linear manner. Therefore, for cases with NA lower than 0.1 [161], the consideration of beam divergence can be neglected for the simplicity of the numerical model, while for more tightly focused laser experiments [49], this effect is supposed to be considered, because the overestimation of ablation depth as high as 10 percent will be introduced based on current study. The effect of beam divergence on the geometry of the ablation crater [162] can be further studied with 2 or 3-dimensional model based on this work.

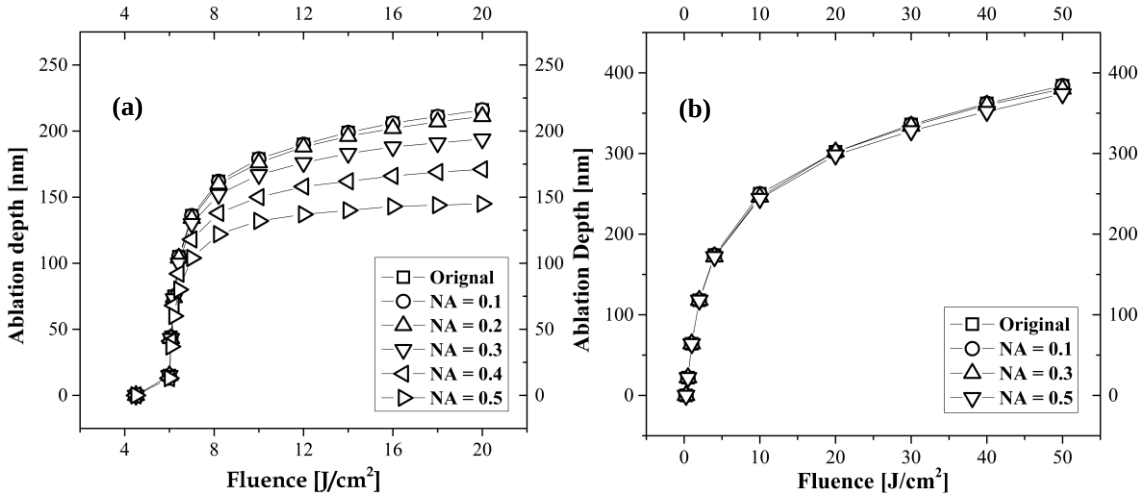

Figure 5.8 Dependence of ablation depth on incident fluence with various NA for (a) transparent (silicon dioxide) and (b) opaque (copper) materials.

It is also believed that the beam divergence effect plays a more important role in transparent materials than opaque ones, which have relatively limited optical penetration depth. To validate this proposition, ULIA is simulated for a common metal as copper. Optical penetration, as well as electron ballistic transportation, are considered, and the transient ablation process is captured with the dynamic description as well. The ablation depth at different incident fluence has been collected for various NA, as shown in Figure 5.8 (b), indicating much less evident differences in ablation depth between different NA. This phenomenon can be interpreted in two aspects. First, the laser intensity develops in a non-linear way with beam divergence below the beam waist, which is assumed be on the top surface of the bulk materials. With shorter beam penetration length, the decrease in energy deposition from beam divergence will be much lower. Also, there is sufficient original free electrons in metallic materials and the dominant mechanism of absorption is inverse Bremsstrahlung process, which is much less non-linear than MPI.

5.6 Plasma defocusing effect

It is also noticeable that the measurement of D^2 deviates from the linear relationship (Eq. (5.1)) with the pulse energy exceeding ~200 μJ. Figure 5.9 (a) shows the spatial distribution of fluence for Gaussian-shape laser pulse at different energy, with the representation of LIAT and measured crater radii by the red dash-dot line and colored circles, respectively. The Gaussian distribution in Figure 5.9 (a) is calculated based on the measurement of focal spot radius ω_0. It can be observed that good agreements can be obtained between the predicted crater radii (cross points of fluence profile and LIAT) and

the measurement for pulse energy up to 200 μJ. While considerable mismatch can be observed for higher pulse energy (300 and 400 μJ), indicating underestimation of crater lateral size following the focal spot size measured with linear relationship under relatively low energy. This extra expansion in ablation craters for high laser energy can be mainly attributed to the plasma defocusing effects induced by air ionization. With generation of air plasma, the focal spot will shift towards the incoming laser beam direction, as can be observed in the energy-dependence focal variation [163,164] and semi-analytical model prediction [163,165]. In order to predict the modified energy spatial distribution under plasma defocusing, modified spot radius ($\omega_{0,\text{defocus}}$) on the sample surface can be employed in replace of the normal value (ω_0), and Gaussian spatial distribution has been assumed to be maintained. The spatial distribution of fluence can be described by the Gaussian function, given as,

$$F = \left(2E / \pi\omega_{0,\text{defocus}}^2\right)\exp\left[-2\left(r / \omega_{0,\text{defocus}}\right)^2\right] \tag{5.3}$$

Based on Eq. (5.3), the modified Gaussian distribution can be obtained to match with the measured crater radii, as shown in Figure 5.9 (b). Through this modification, the laser energy is redistributed in a wider region, and the peak fluence at 300 and 400 μJ is predicted to drop below that at 200 μJ. The peak fluences from Gaussian distribution with normal radius ω_0 (Figure 5.9 (a)), and the defocused radius $\omega_{0,\text{defocus}}$ (Figure 5.9 (b)) are denoted as Gaussian and Real, respectively. Below 200 μJ, as shown in Figure 5.10 (a), the peak fluence is identical for both cases, however, the predicted Gaussian peak fluence can be much greater than the Real one, where the former value is more than 2 and 4 times of the latter value at 300 and 400 μJ, respectively. Instead of the linearly increasing Gaussian

peak fluence, the Real peak fluence turns to drop beyond 200 μJ down to around 10 J/cm^2 at 400 μJ. Taken 200 μJ as the threshold energy for air ionization, the corresponding peak intensity is ~1.04×10^{14} W/cm^2, which is close to the predicted air breakdown threshold with 100 fs laser pulse in [166], however, much lower than ~4.5×10^{14} W/cm^2 reported in [164] with 12 fs laser pulse. This decreasing breakdown intensity with extended pulse duration is consistent with the observation in [167] for ionization of dielectric materials. It is worth to mention that laser pulse energy consumption due to air ionization plays a negligible role in the reduction of fluence on the sample surface, and no more than 5% [102,164,166] of the pulse energy can be consumed for air ionization within the laser intensity range considered in this study. Based on this, the energy loss during beam penetration in air has been neglected.

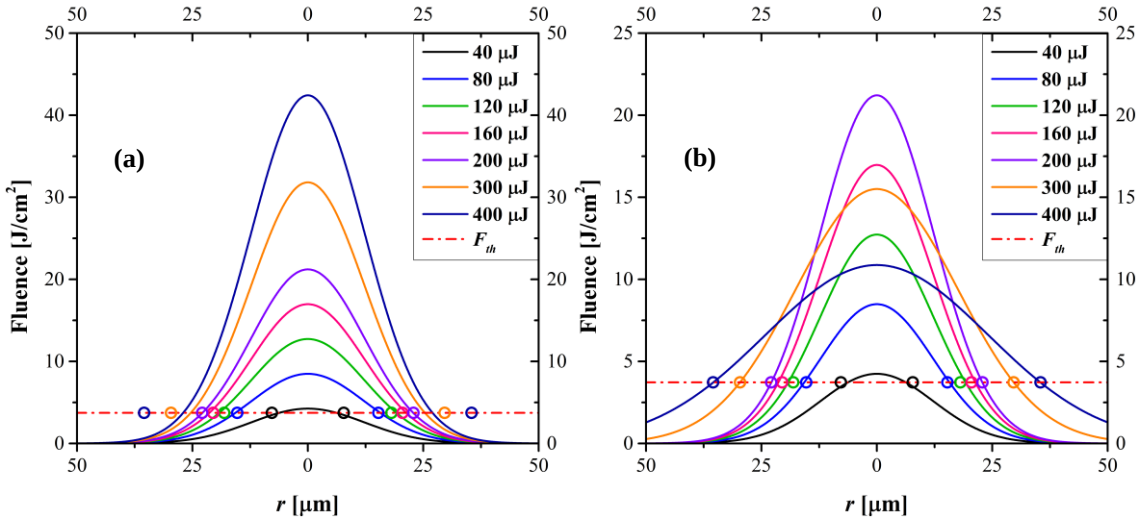

Figure 5.9 Gaussian-shape laser fluence distribution based on (a) normal beam focal spot radius ω_0 and (b) modified radius considering plasma defocusing $\omega_{0,\text{defocus}}$. Red dash-dot line indicates the single-pulse LIAT, and the circles in (a) and (b) represent the ablation crater radii at different pulse energy.

Ablation rate has been predicted based on both Gaussian and Real peak fluence, and compared as shown in Figure 5.10 (b). Instead of the continuously increasing ablation rate from Gaussian peak fluence (blue circle), decrease of ablation rate with pulse energy over 200 μJ can be successfully predicted based on the Real peak fluence, in good agreement with the experimental data. It cannot be fully guaranteed that the laser beam propagation can still maintain the Gaussian shape (both temporal and spatial) with air plasma defocusing, but in the current simulation and experiments, the simplified Gaussian-shape assumption can provide good prediction to quantify the ablation rate based on the measured crater diameter.

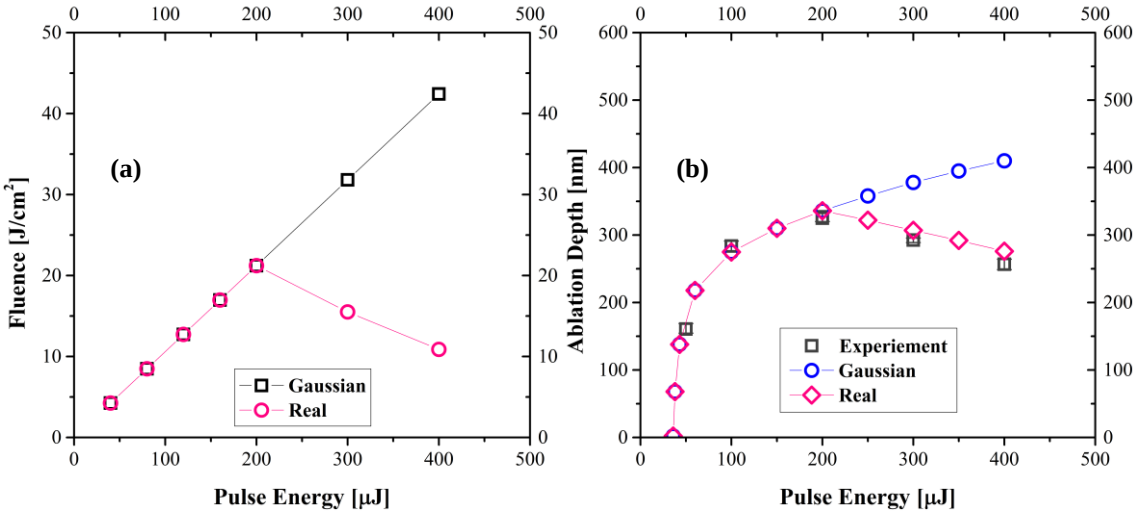

Figure 5.10 Comparison of (a) peak fluence and (b) ablation depth with and without plasma defocusing effects as a function of laser pulse energy.

5.7 Thermal accumulation effect

Ultrafast laser is proven to have remarkable potential in direct fabrication of dielectric materials [34,49,168,169], which are difficult to machine by traditional

techniques due to high hardness, brittleness and low thermal conductivity. However, the material removal efficiency remains unsatisfactory, typically within ~200 nm per laser pulse [145,170]. To alleviate this, high-repetition-rate multi-pulse laser irradiation has been suggested as a promising solution to diminish the ablation threshold [149,171] and enhance the ablation rate [155]. With high-repetition-rate laser pulses, material can be more easily ablated by thermal accumulation effect, which is predominantly resulted from material heating that cannot be completely relaxed and consequently accumulated under multi-pulse irradiation. Prominent thermal accumulation has been confirmed at repetition rates over megahertz (MHz) [148,155,171], but the requirement of high repetition rate can raise challenges to laser techniques (high-repetition-rate and high-power ultrafast laser) and place limitations on promoting this method. Therefore, it will be highly desirable if thermal accumulation can be stimulated at low repetition rates, e.g. kilohertz (kHz), to effectively enhance ablation rates. However, it was generally believed that repetition rates lower than MHz are insufficient to trigger thermal accumulation. This conclusion was found true in certain metals and semiconductors [155], but there is a lack of fundamental understanding of the mechanism. It is still unclear about other materials, such as dielectrics.

In addition to thermal accumulation effect, there is also non-thermal accumulation effect (by crater surface roughening, structural transformation, phase transition, etc.), which can enhance material removal rate under multi-pulse ablation. It was found to reduce ablation threshold even at low repetition rates [150]. However, there has been no previous study clearly discriminating the contribution by thermal and non-thermal accumulation, and usually their combined effect is referred as “incubation effect”. A clear knowledge in

this regard will greatly assist one to make the most of thermal accumulation in a variety of applications.

Based on these concerns, to promote thermal-accumulation-assisted ablation enhancement (termed as ablation cooling in [155]) in ultrafast laser processing of fused silica, we aim to distinguish the thermal and non-thermal accumulation regimes for fused silica, unveil the threshold repetition rate to trigger thermal accumulation, and enhance the fundamental understanding of the mechanism. For this purpose, ultrafast laser ablation in fused silica has been experimentally studied in a wide range of repetition rates (10 Hz-10 kHz) at varying pulse energy (40 μJ-200 μJ) and pulse number (1-100). We have established a comprehensive model incorporating the plasma model and the two-temperature model (TTM) to simulate ultrafast laser interaction with fused silica by single and multiple pulses at varying repetition rates. The fundamental mechanisms of thermal-accumulation-assisted ablation enhancement can be well interpreted through numerical simulation.

Single-pulse ablation threshold fluence is determined by Liu's method [147] as 3.72 J/cm^2, which agrees well with measurements in previous works [74,170]. Ablation rates (ablation depth per pulse) are evaluated through dividing the depth of ablated crater by the pulse number, as summarized in Figure 5.11. With varying pulse number and repetition rate, there are two major interesting observations. Firstly, ablation rate increases with increasing pulse number, as shown in Figure 5.11 (a). With the repetition rate of 10 Hz, the ablation rate is increased by 50-70% by 100 pulses compared to single-pulse ablation at the same pulse energy. This enhancement is mainly attributed to non-thermal accumulation

effect, leading to increased laser energy deposition and reduced ablation threshold. Compared with single-pulse ablation, laser absorption in multi-pulse ablation can be increased [172] due to the rough crater surface induced by preceding laser pulses. Besides, there is either structural transformation or phase transition in the unablated material, which can reduce the energy barriers for ablation.

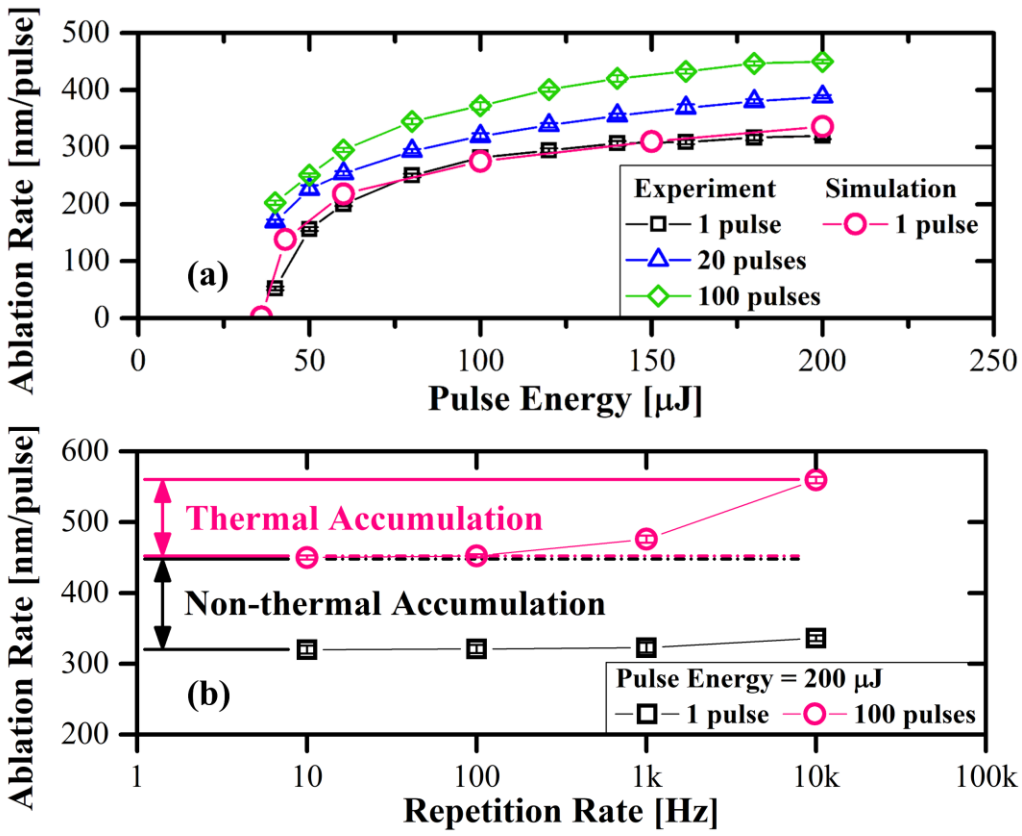

Figure 5.11 Experimental measurement of ablation rate as (a) a function of pulse energy at 10 Hz, and (b) a function of laser pulse repetition rate. Simulation results of single-pulse ablation rate are depicted in (a). Ablation enhancement by non-thermal and thermal accumulation are demonstrated in (b). Pulse numbers are denoted in the legends.

Secondly, by increasing the repetition rate to over 1 kHz, the ablation rate is further enhanced, in addition to that from the non-thermal accumulation effect. Figure 5.11 (b) summarizes the ablation rate as a function of repetition rate, by single and 100 pulses at 200 μJ. At repetition rates below 1 kHz, the ablation rate by 100 pulses is ~50% higher than that by single pulse ablation due to the non-thermal accumulation. Based on its nature, non-thermal accumulation effect should not be sensitive to repetition rates. However, when the repetition rate further increases, the ablation rate is enhanced by another ~10% (30 nm) at 1 kHz, and ~35% (100 nm) at 10 kHz, respectively. The cause of this additional enhancement is postulated as the thermal accumulation effect, which is expected to be more prominent at increasing repetition rates. As shown in Figure 5.11 (b), at 10 kHz, the thermal accumulation and non-thermal accumulation effect co-contribute to an overall ablation enhancement of virtually 100% compared with the single-pulse ablation rate. This overall effect has been generally termed as incubation effect, but without distinguishing the contribution from thermal and non-thermal accumulation effects previously.

It has been widely accepted that thermal accumulation can only happen at repetition rates over MHz [148,155,171], which is in contrast to the observation and hypothesis in this study. In order to confirm and understand the occurrence of thermal accumulation at kHz, a plasma model and the TTM are combined to study thermal responses to ultrafast laser in fused silica [173].

Based on this model, surface temperature evolutions in single and multiple pulses are predicted to study thermal relaxation in fused silica by ultrafast laser ablation. Figure 5.12 (a) demonstrates the evolution of surface temperature after single-pulse ablation. The

surface temperature at 1 ps is close to 3223 K, which is the maximum lattice temperature at the surface during ablation. By thermal relaxation until 10 ns, the surface temperature drops below the melting point (1986 K [174]). Until 1 ms (pulse time interval for 1 kHz), the temperature is ~20 K above the ambient temperature (300 K). This 20 K residual temperature is not much, but can be accumulated to have significant impact by applying multiple pulses. To clearly show this effect, Figure 5.12 (b) depicts the calculated surface temperature evolution by 20-pulse ablation at varying repetition rates. The surface temperature data are captured at the moments before the arrival of each successive laser pulse, as conceptually demonstrated by the heating and cooling cycle curve. At 10 and 100 Hz, the surface temperature is cooled sufficiently close to the room temperature by the arrival of a successive pulse, and there is negligible thermal accumulation. However, at repetition rates over 1 kHz, the thermal accumulation starts to occur. The surface temperature is "accumulated" by ~120 K at 1 kHz and over 450 K at 10 kHz. This temperature escalation reduces the energy barrier of ablation and consequently increases the ablation rates. Supported by the simulation analysis, we can confirm that thermal accumulation effect does happen at repetition rates over 1 kHz in fused silica, and is responsible for the additional ablation enhancement.

Another interesting finding by the numerical simulation is that the surface temperature relaxation is dominated by thermal conduction, while convection heat loss as well as thermal radiation have negligible impacts (even with very high convective heat transfer coefficient and emissivity). This is because the laser heated depth (~200 nm) is much smaller than the sample thickness (a couple of mm or thicker), and the surface is

mainly cooled down by thermal conduction within the time scale considered in this study (1 ms or less). Therefore, the threshold repetition rate to trigger thermal accumulation is independent on the ambient condition, except for very thin films (thickness of μm or less).

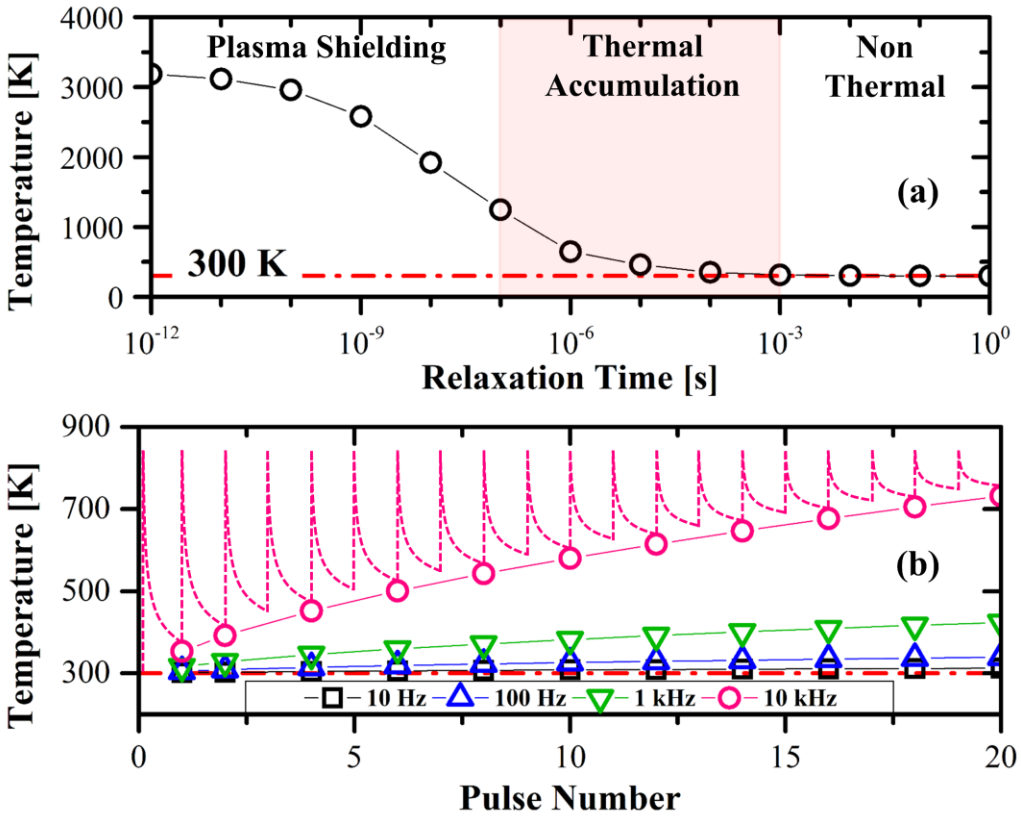

Figure 5.12 Calculated temperature at the surface of unablated material as (a) a function of time for single-pulse ablation and (b) a function of pulse number at different repetition rates for multi-pulse ablation. Three regimes are represented in (a) with respect to laser pulse repetition rate (thermal relaxation time). In (b), temperatures are captured at the moments before the arrival of the successive laser pulse, and surface heating and cooling cycles (dash curve) are conceptually depicted (not drawn to the temperature-axis scale), where the peak temperature of heating is the boiling temperature (3223 K).

Based on the current experimental and simulation results, thermal accumulation is confirmed to occur at repetition rates over 1 kHz in fused silica. Stronger thermal accumulation is expected at repetition rate over 10 kHz to further increase the ablation rate. However, when the repetition rate is over 10 MHz, plasma shielding effect [175,176] becomes considerable to diminish energy deposition into the bulk material. Based on this, multi-pulse ultrafast laser ablation of fused silica can be categorized into three regimes, namely, non-thermal accumulation (below 1 kHz), thermal accumulation (1 kHz-10 MHz) and plasma shielding (above 10 MHz). The transition from thermal accumulation to plasma shielding is not rigorously triggered at 10 MHz, but estimated based on the plasma lifetime of ~100 ns. Suppression of laser energy deposition and ablation by plasma shielding relies on strong absorption in the ejected dense plasma, so that thermal accumulation and plasma shielding are expected to compete in the range of 10-100 MHz.

The TTM is a computationally efficient model with decent accuracy, however, requires the accurate description of multiple thermodynamics and optical properties. In order to have a rapid prediction of the threshold repetition rates of thermal accumulation in different types of materials, a theoretical model [177] is further adopted to describe thermal relaxation process,

$$\Delta T_0(t,z) = \Delta T_0 \left(\frac{l_z^2}{l_z^2 + 4\alpha t} \right)^{0.5} \exp\left(-\frac{z^2}{l_z^2 + 4\alpha t} \right), \tag{5.4}$$

where ΔT_0 is the maximum temperature change, l_z is the initial heating depth, α is the thermal diffusivity, and z is position in depth. Copper and silicon are selected as the

representative of metals and semiconductors for comparison and their physical parameters are listed in Table 5.1.

Table 5.1 Physical parameters for materials [24,174,178].

Parameters	Fused silica	Copper	Silicon
α [mm^2/s]	0.85	111	88
T_b [K]	3223	2833	3538
l_z [nm]	326.5	150	200

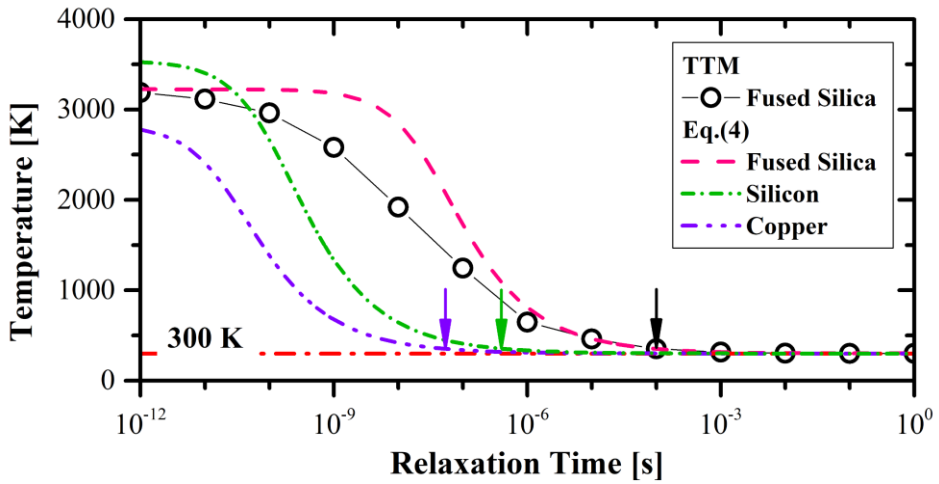

Figure 5.13 Surface temperature relaxation by Eq. (5.4) for fused silica, silicon and copper and by the TTM for fused silica. The colored arrows represent the threshold repetition rates from non-thermal accumulation to thermal accumulation for different materials.

Surface temperature evolution in fused silica calculated by Eq. (5.4) (red dash line) is depicted in Figure 5.13 in comparison with that from the TTM (black circle line). Apparent discrepancy can be observed within 1 μs, which is resulted from different initial temperature spatial distributions [177] and strong electron heat diffusion by laser ionization not considered in Eq. (5.4). Despite this discrepancy, satisfactory agreement with the TTM

can be attained by Eq. (5.4) with relaxation longer than 10 μs, which is close to the time scale corresponding to the threshold repetition rates of thermal accumulation. Due to its simplicity, we use this single analytical equation to perform a rapid prediction of the threshold repetition rates of thermal accumulation in copper and silicon. As shown in Figure 5.13, copper and silicon demonstrate thermal accumulation at much higher repetition rates. To compare the threshold repetition rates in three different materials (fused silica, copper and silicon), taking the residual surface temperature (~50 K) at 10^{-4} s (10 kHz) in fused silica as reference, thermal accumulation is anticipated to be considerable at repetition rate above 1 MHz and 10 MHz for silicon and copper, which are 100 and 1000 times higher than that in fused silica (10 kHz), respectively. These repetition rates are well corroborated by experiments in [155], where pronounced ablation enhancement has been achieved in silicon and copper at 27 MHz and 108 MHz, respectively. As mentioned, thermal conduction dominates the thermal relaxation, therefore, differences in thermal diffusivity are responsible for these different threshold repetition rates. As shown in Table 1, the thermal diffusivity of fused silica (0.85 mm^2/s) is 100 and 130 times smaller than that of silicon (88 mm^2/s) and copper (111 mm^2/s), respectively, which leads to much stronger thermal accumulation in fused silica triggered at kHz.

5.8 Summary

Ultrafast laser-induced ablation of dielectric materials has been investigated based on a one-dimensional plasma-temperature combined model. CBE excitation and relaxation have been involved to describe the evolution of electron number density. Temporal and

spatial variations of temperature are monitored to capture the evolution of ablation depth, where the vaporization temperature is treated as the ablation criterion and a dynamic description of material removal is employed for the consideration of thermal energy losses through ablation. Numerical prediction of LIAT and ablation depth based on the proposed ablation criterion agree well with experimental observations. With the increase of pulse energy, ablation depth experiences sharp increase above ablation threshold, and tends to increase slowly. Further increase of energy brings about, however, decrease in ablation depth, which can be mainly attributed to plasma defocusing effect with non-equilibrium air ionization. With increasing pulse number from 1 to 100, the ablation rate can be increased by 100-150 nm with repetition rate below 1 kHz. While with higher repetition rate than 1 kHz to 10 kHz, more significant enhancement of ablation rate can be observed with multi-pulse irradiation, as high as 250 nm (almost double of the ablation rate at single pulse). This enhanced thermal accumulation effect by increasing repetition rate above 1 kHz can be well demonstrated by the simulation. For ULIA, especially for femtosecond laser pulses, low fluence manufacturing is proposed for high ablation efficiency and good microstructure quality. Consideration of beam divergence in calculation is observed to be more important for transparent than for opaque materials. The ablation enhancement with multiple pulse and increasing repetition rate provides valuable information to improve the processing and micromachining of dielectric materials with ultrafast laser pulses.

CHAPTER SIX

ULTRAFAST LASER MICROMACHINING OF DIELECTRIC MATERIALS

Ultrafast lasers provide a promising solution for microchannel fabrication in transparent materials. Nevertheless, laser-based direct drilling has been believed as disqualified to fabricate high-aspect-ratio channels. More importantly, the fundamental mechanism of channel self-termination remains elusive. This chapter presents a comprehensive study of ultrafast laser direct drilling in fused silica with a wide range of drilling speed (20-500 μm/s) and pulse energy (60-480 μJ) to examine the feasibility of high-aspect-ratio and high-quality channel drilling inside fused silica. Moreover, the dominating mechanism of channel self-termination is discussed.

6.1 High aspect-ratio and high-quality drilling

The channels are drilled in the method as described in Section 2.2 and quantitatively characterized to evaluate length, diameter, aspect ratio and structure quality as a function of drilling speed and pulse energy, as summarized in Figure 6.1. A wide range of pulse energy (60-120-180-270-360-480 μJ) and drilling speeds (20-50-100-150-200-250-300-400-500 μm/s) are applied. The maximum channel length over 2000 μm (with ~60 μm diameter) is achieved in this study, which is longer than most of the channels obtained in previous studies with even more complicated methods [48,179,180], indicating the feasibility of ultrafast laser direct drilling in air to achieve satisfactory channel length without complicated setup. As shown in Figure 6.1 (a), the channel length generally increases with the pulse energy at the same drilling speed, because of the increasing kinetic

energy of the ejected material to escape from longer channels at higher pulse energy [49]. However, at drilling speeds lower than 300 μm/s, the channel length starts to decrease after the pulse energy reaches 270 μJ. It can be resulted from microcracks by material overeating and strong shock waves [49]. This phenomenon does not happen at high drilling speeds (over 300 μm/s) because the energy deposition is not sufficient to trigger microcracks with such high drilling speeds.

At the same pulse energy, the channel length first increases with the drilling speed to the maximum value and then decreases, introducing an optimal drilling speed for each pulse energy. The optimal drilling speed tends to increase with the pulse energy, raising from 100 μm/s at 60 μJ to 150, 200 and 300 μm/s at 180, 270 and 480 μJ, respectively. This observation for the first time unveils the close correlation between drilling speed and pulse energy in channel drilling. In previous studies [47,49,57,179,181,182], the optimal drilling speed was believed to be a constant and independent on pulse energy. It is easy to understand that the channel length is shorter at high drilling speed due to insufficient laser energy deposition for material removal. However, it is surprising that the channel length will be reduced at very low drilling speed. The underlying mechanism will be analyzed and discussed in Section 6.3.

The variation of channel diameter with pulse energy and drilling speed is shown in Figure 6.1 (b). The channel diameter increases with the pulse energy due to the radial expansion of the damage area. As the drilling speed increases, the channel diameter will decrease since the energy deposition per unit volume is reduced.

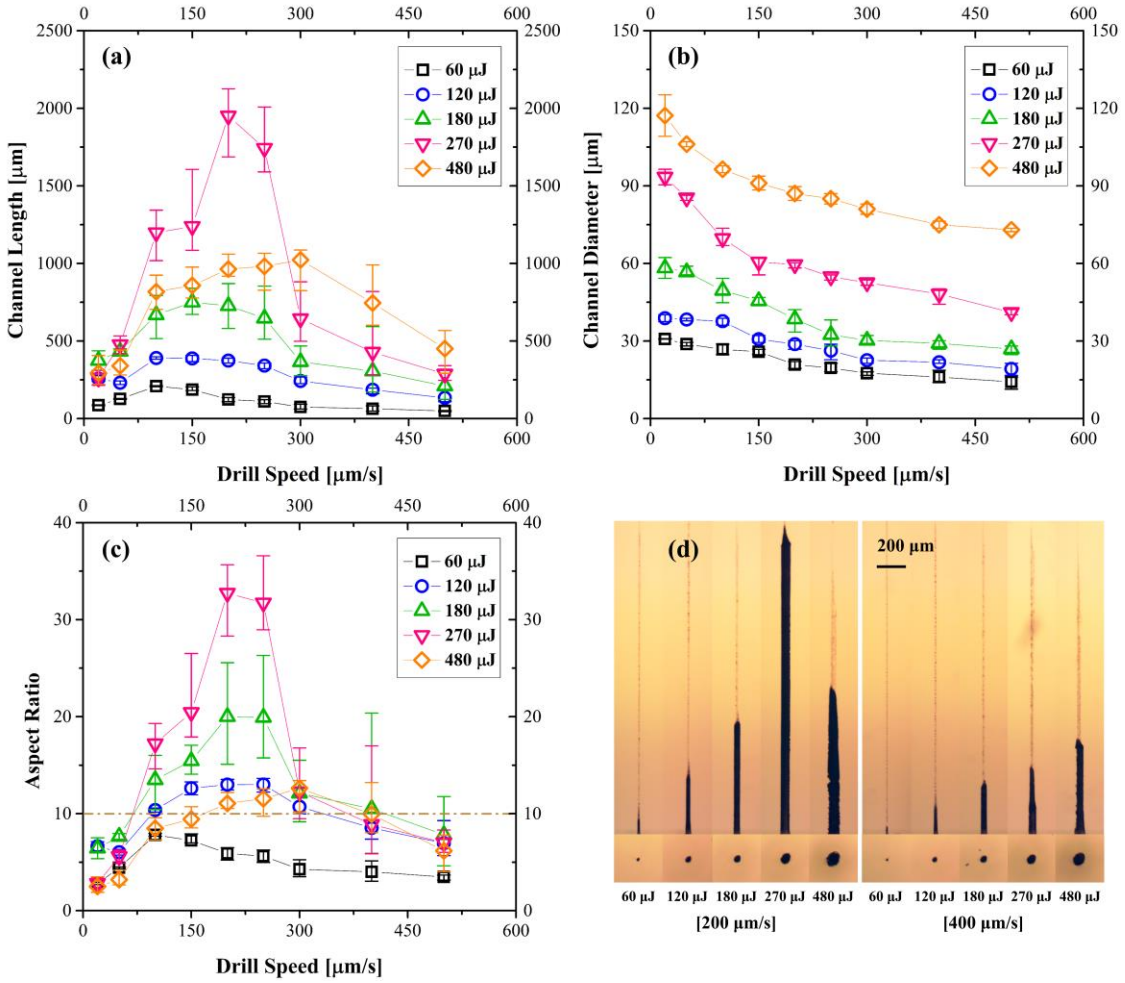

Figure 6.1 Ultrafast laser-fabricated microchannel (a) length, (b) diameter, (c) aspect ratio and (d) structural and geometric quality as function of drilling speed at different pulse energy.

The aspect ratio is calculated and displayed in Figure 6.1 (c). The maximum aspect ratio (~35:1) is obtained at 270 μJ, which is comparable to the highest aspect ratio (40:1) obtained by a more complicated method [48] and much higher than those by previous studies using laser direct drilling [47,49,179]. The variation of the aspect ratio with drilling speeds follows the similar trend with the channel length, since the variation of diameter is

less sensitive to drilling speeds. However, the ranking of the aspect ratio can be different from that of channel length. For instance, at the drilling speed of 200 μm/s, the aspect ratio at 180 μJ reaches as high as twice of that at 480 μJ, while the length at 180 μJ is only three fourth of that at 480 μJ. At 300 μm/s, the aspect ratio is comparable between 120 μJ and 480 μJ, whereas the length at 480 μJ is as high as four times of that at 120 μJ. As a result of this changed ranking, the optimal drilling speed in pursuit of the maximum aspect ratio can be higher than that for the maximum channel length, for instance, rising from 150 μm/s (the maximum channel length) to 200 μm/s (the maximum aspect ratio) at 180 μJ. Taking 10:1 as the minimum aspect ratio, most of the qualified channels are drilled at drilling speeds between 100 and 300 μm/s, which can guarantee a rapid drilling process.

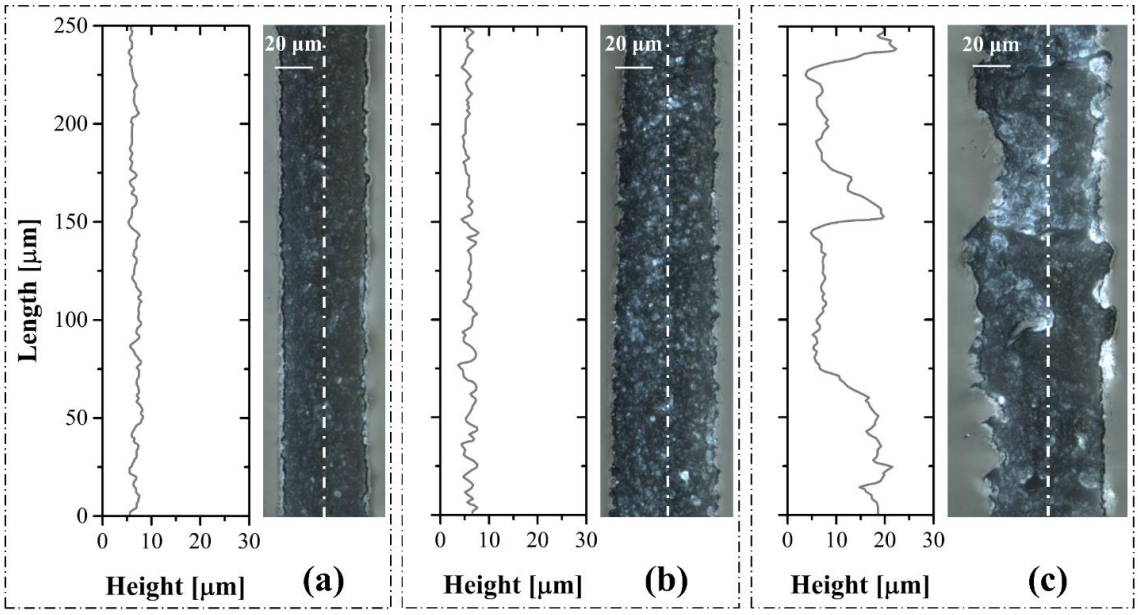

Figure 6.2 Morphology and centerline profile of the cross section in drilled channels at 200 μm/s drilling speed and pulse energy of (a) 180 μJ, (b) 270 μJ and (c) 480 μJ. The centerline profiles are captured along the white dash-dot lines.

Besides the channel length and the aspect ratio, the channel sidewall quality is important for applications. To examine the quality, side-view optical microscope images are captured and depicted in Figure 6.1 (d) for different pulse energy at selected drilling speeds (200 and 400 μm/s). The drilled channels appear as the dark regions. Despite occasional narrowing at the end of the channel (at high drilling speed of 400 μm/s), excellent uniformity is observed in the channels, which are free of tapering and bending.

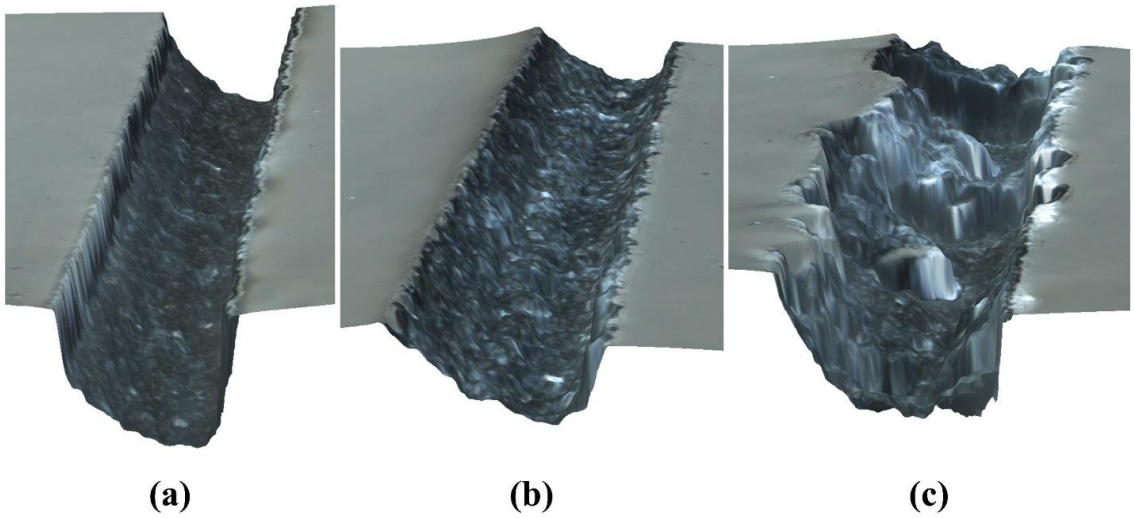

Figure 6.3 3D representation of cross-sectional morphology in the drilled channels at 200 μm/s drilling speed and pulse energy of (a) 180 μJ, (b) 270 μJ and (c) 480 μJ.

To evaluate the sidewall roughness, the channels are cut to examine the cross-sectional features. Based on the cross-sectional images in Figure 6.2, the sidewall roughness is captured from the centerline profile along the dash-dot line. 3D morphology in the perspective view is also captured to better demonstrate the channel sidewall quality, as shown in Figure 6.3. Smooth sidewalls are achieved at 180 μJ and 270 μJ and rough

sidewall is observed at 480 μJ. This rough sidewall is mainly caused by microcracks from strong thermoelastic shock waves [49]. The surface roughness (Ra) is measured as 0.65, 0.66 and 5.17 μm for 180, 270 and 480 μJ, respectively, suggesting satisfactory sidewall quality at pulse energy no higher than 270 μJ.

In summary, 270 μJ serves as the overall optimal pulse energy for channel drilling, providing maximum channel length and aspect ratio, outstanding sidewall quality and excellent uniformity (free of tapering and bending).

6.2 Analytical model

Laser beam propagation and interaction with fused silica is conceptually demonstrated in Figure 6.4. In Figure 6.4 (a), the laser focusing geometry and the damage profile are represented by the solid and dash-dot line, respectively. The region enclosed in the damage profile has local fluence higher than the material ablation threshold F_{th}. Based on this damage profile, the drilling process is schematically illustrated in Figure 6.4 (b), where the material will be removed along the upward scanning path of damage profile, forming a straight channel from the rear surface.

Based on Gaussian-beam spatial distribution and focusing geometry, the damage region in Figure 6.4 (a) can be analytically described as follows. Given the laser wavelength of λ, laser beam radius at focal spot (waist radius) of ω_0, pulse energy E, laser beam quality M^2, and ablation threshold fluence of F_{th}, the Rayleigh length z_R, peak laser fluence F_0 at the focal spot and the beam radius ω at distance z away from the focal plane are defined as follows,

$$z_R = \frac{\pi\omega_0^2}{\lambda \mathrm{M}^2}, \tag{6.1}$$

$$F_0 = 2E / \pi\omega_0^2, \tag{6.2}$$

$$\omega = \omega_0 \sqrt{1 + \left(\frac{z}{z_R}\right)^2}. \tag{6.3}$$

The local fluence F in the focusing geometry can be expressed as,

$$F = F_0 \frac{w_0^2}{w^2} \exp\left(-2\frac{r^2}{w^2}\right) = F_0 \left(\frac{z_R^2}{z_R^2 + z^2}\right) \exp\left[-2\frac{r^2}{w_0^2}\left(\frac{z_R^2}{z_R^2 + z^2}\right)\right], \tag{6.4}$$

where r represents the distance in the transverse direction to the beam center.

For simplicity, the following auxiliary variable is defined as,

$$z^* = \frac{z_R^2}{z_R^2 + z^2}, z^* \in (0,1], \tag{6.5}$$

and Eq. (6.4) is rewritten in a simplified form as,

$$F = F_0 z^* \exp\left[-2z^* \frac{r^2}{\omega_0^2}\right]. \tag{6.6}$$

The damage profile is determined by the material damage threshold fluence, $F_{th} = F = F_0 z^* \exp\left[-2z^* r^2 / \omega_0^2\right]$, which leads to the prediction of diameter as follows,

$$D^2 = \frac{2w_0^2}{z^*} \ln\left(\frac{F_0 z^*}{F_{th}}\right), z^* \in \left[\frac{F_{th}}{F_0}, 1\right]. \tag{6.7}$$

Based on Eq. (6.7), on one hand, the channel diameter, as well as the maximum D_m at given laser fluence can be predicted,

$$D_m^2 = \begin{cases} 2\omega_0^2 \ln\left(\dfrac{F_0}{F_{th}}\right), & F_{th} \le F_0 < eF_{th}, \text{ at } z^* = 1 \quad (a) \\ 2\omega_0^2 \dfrac{F_0}{eF_{th}}, & F_0 \ge eF_{th}, \quad \text{at } z^* = \dfrac{eF_{th}}{F_0} \quad (b) \end{cases} \tag{6.8}$$

This relationship demonstrates a linear dependence of the diameter square on the laser fluence applicable in a much wider range of laser fluence ($F_0 \ge eF_{th}$) than the semilogarithmic relationship limited within $F_{th} \le F_0 < eF_{th}$.

On the other hand, a damage length L is defined as the distance between the focal spot to the damage profile in longitudinal direction as shown in Figure 6.4 (a). Let D=0, the longitudinal boundary is achieved at $z^* = F_{th} / F_0$, which leads to,

$$L = |z| = z_R \sqrt{\frac{F_0}{F_{th}} - 1} \tag{6.9}$$

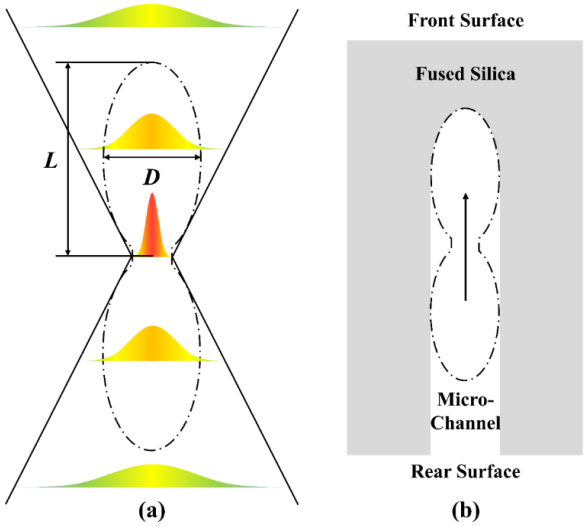

Figure 6.4 Schematic illustration of (a) damage profile in a focused Gaussian laser beam and (b) laser-based rear-side drilling in fused silica.

This analytical model essentially features the laser beam propagation and interaction with dielectrics during drilling process, providing the theoretical basis for estimation of material removal dimensions (diameter and damage length L) in laser-based dynamics fabrication.

The damage profile in this analytical model is verified as follows. As shown in Figure 6.5 (a), a channel exit is formed on the front surface when the laser beam drills through the sample. Since the laser fluences studied are higher than e times of the threshold, Eq. (6.8b) is utilized to capture the relationship between the exit diameter and laser pulse energy and compare with experimental measurements.

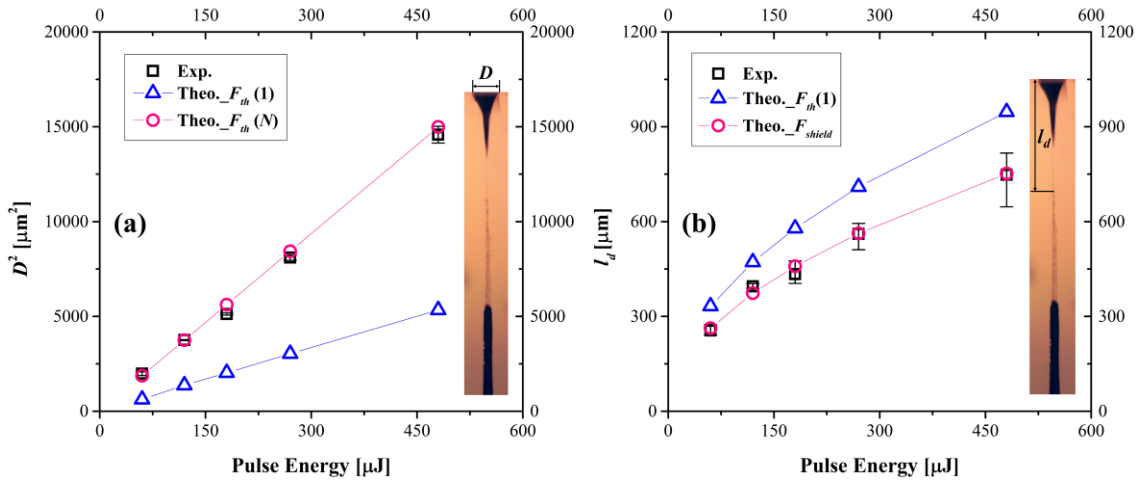

Figure 6.5 Experimental measurements and theoretical estimation of the (a) channel exit diameter and (b) surface damage shielding length as function of pulse energy.

The linear relationship in Eq. (6.8b) can be corroborated by experimental results in Figure 6.5 (a), where the physical parameters in Eq. (6.8b) are adopted as ω_0=3.95 μm and F_{th}=4.04 J/cm^2 measured in Liu's method [147]. However, the theoretical prediction (blue

triangle) is significantly underestimated compared to the experiments (black squares). This is mainly because the adopted threshold fluence is determined based on single-pulse measurement, whereas threshold decrease due to incubation effect [148,150,152] plays an important role during repetitive laser pulse irradiation in the drilling process. To adapt the physical parameters, linear fitting is applied to the measured diameters, and the corrected damage threshold F_{th} (N) is determined as 1.53 J/cm^2, which is in excellent agreement with multi-pulse measurements [183]. Based on this, the linear dependence between the square of channel diameter and laser pulse energy (fluence) has been fully validated and significant incubation effect inside the material during drilling process has been elucidated.

Another feature can be evaluated based on the analytical model as well. As mentioned, when laser beam is moved approaching the front surface, a channel exit is formed on the front surface. This surface damage can start before the arrival of focal spot and shield successive laser pulses. Due to this surface damage shielding effect, laser-induced modification (drilled channel or filament) will terminate at certain position beneath the surface exit. The distance (l_d) between this termination position and the front surface is expected to relate closely with the damage length L defined in Eq. (6.9). To verify this, l_d is measured at different pulse energy and compared with theoretical estimation (blue triangle) based on Eq. (6.9) (ω_0=3.95 μm and F_{th} (1)=4.04 J/cm^2), as shown in Figure 6.5 (b). In contrast to the diameter, the predicted damage lengths are higher than measurements based on the single-pulse damage threshold. This overestimation can be attributed to two major factors. On one hand, incubation effect in surface shielding is not as significant as in the diameter expansion. Surface shielding takes effect as long as there is sufficient surface

damage, and successive laser pulses cannot further modify internal materials. Therefore, incubation effect is only effective before surface shielding is triggered. On the other hand, surface shielding cannot be triggered as soon as the fluence on the front surface just reaches the damage threshold, but requires sufficient damage area on the surface. Theoretical fitting of the measurements suggests a surface shielding threshold (F_{shield}) as 6.40 J/cm^2, which is 60% higher than F_{th} (1). The corresponding diameter to F_{shield} in the damage profile will be considered as the necessary surface damage area for surface shielding. Excellent agreements between l_d measurements and Eq. (6.9) further validate the analytical model in accurate description of laser-based drilling process.

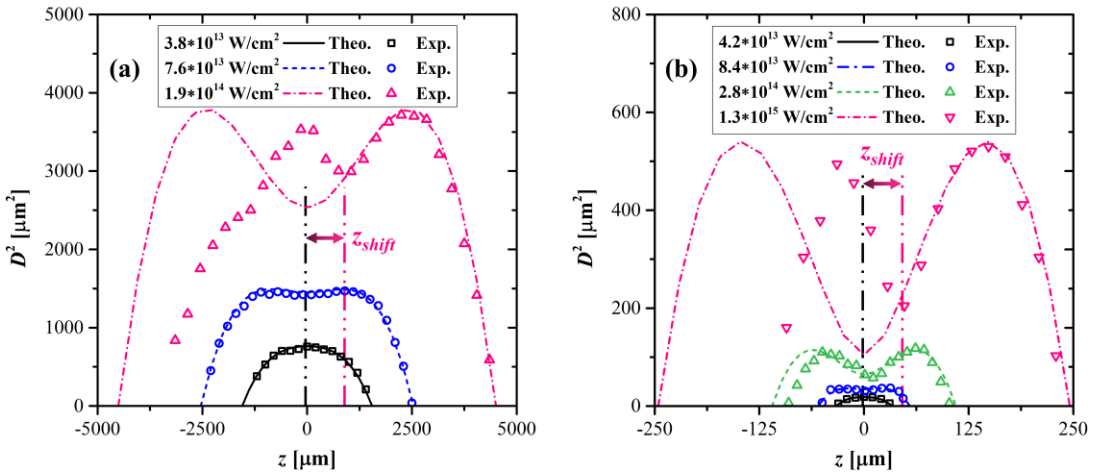

Figure 6.6 Comparison between theoretical prediction and experimental measurements of ablation spot diameter square in fused silica as function of off-focal distance at various laser intensity for (a) NA=0.01 and (b) NA=0.08. Zero position of z indicates the focal spot position, positive and negative values in z axis represent the distance between the sample surface and the focal spot position beneath and above the sample surface, respectively.

To further examine the damage region profile, the ablation crater diameters at different focal positions are measured. Diameter squares are displayed as a function of longitudinal position in Figure 6.6 and Figure 6.7 for fused silica and stainless steel, respectively. Based on Eq. (6.7), in focused Gaussian-shape laser beam, the damage region transition from single-lobe to double-lobe shape at increasing laser fluence across eF_{th} is expected. Theoretical damage profiles at different fluences are predicted based on single-pulse ablation thresholds (3.72 J/cm^2 for fused silica [184] and 0.17 J/cm^2 for stainless steel [148,185]), since incubation effect is eliminated by single-pulse shot on spot. Two shapes of damage profiles are validated by experimental measurements, as shown in Figure 6.6.

Despite the decent agreements at relatively low fluences, deformation of the damage region can be observed at high laser fluences, with focal shift (z_{shift}) towards the laser beam incoming direction (positive z). This is mainly attributed to strong air ionization, where air plasma defocuses the incoming laser beam before it arrives at the designated focal plane. This plasma defocusing effect cannot be triggered at laser fluence lower than air ionization threshold and becomes increasingly significant with higher laser fluence over air ionization threshold. As shown in Figure 6.6, the focal shift in NA=0.01 at intensity of 1.9×10^{14} W/cm^2 can reach as long as ~1000 μm. On the contrary, in stronger geometrical focusing (NA=0.08), the focal shift at similar laser intensity is only ~10 μm. On one hand, this much shorter focal shift at high NA is resulted from much shorter Rayleigh length in NA=0.08 (~40 μm) than that (~1800 μm) in NA=0.01. On the other hand, Kerr self-focusing (KSF) plays a more important role in low NA condition than high NA condition [186], stimulating air plasma formation at farther distance away from the designated focal

plane, so that the focal shift is much greater. The focal shifts are only determined by the ambient ionization and insensitive to the sample material. This is confirmed by the identical focal shifts of stainless steel to those of fused silica at similar laser conditions.

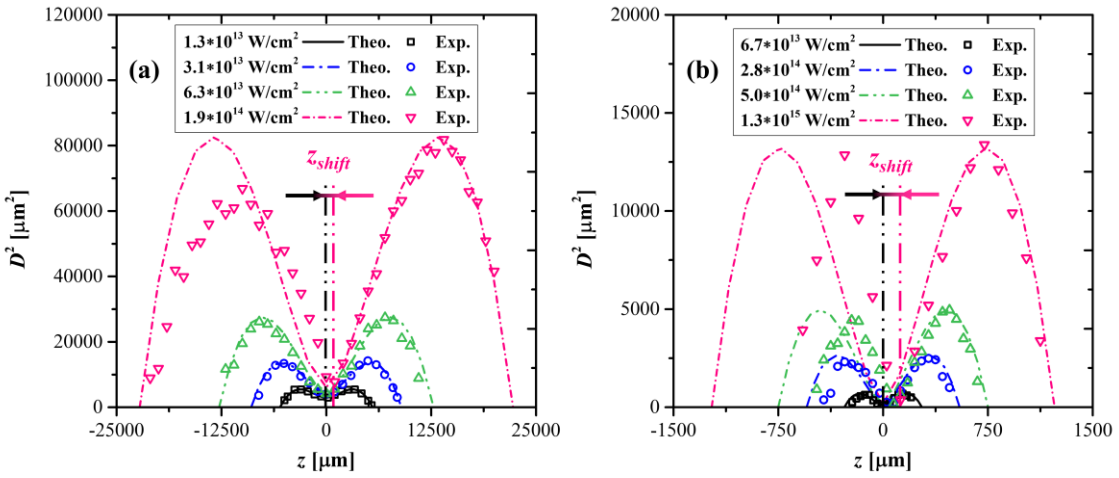

Figure 6.7 Comparison between theoretical prediction and experimental measurements of ablation spot diameter square in stainless steel as function of off-focal distance at various laser intensity for (a) NA=0.01 and (b) NA=0.08. Zero position of z indicates the focal spot position, positive and negative values in z axis represent the distance between the sample surface and the focal spot position beneath and above the sample surface, respectively.

With plasma defocusing, before arrival at the shifted focal plane, the measured damage profiles can accurately resemble the theoretical profile and the maximum diameter. In the region below the shifted focal plane, another maximum diameter can be observed, however, this diameter is asymmetric to the first maximum diameter and different from the predicted one. This second diameter is typically smaller than the predicted value due to laser energy loss in plasma ionization and absorption [102]. The diameter discrepancy increases with longer damage profile in *z* direction (much significant discrepancy in Figure

6.7 (a)). Therefore, shorter damage profile from high NA focusing geometry and high material damage threshold F_{th} could help to diminish the diameter discrepancy. Even with deformed damage profile and different diameters on the two lobes, since the percussion drilling diameter is always determined by the maximum diameter, the theoretical prediction will be reliable.

The percussion drilling diameters being not affected by ambient ionization requires the laser fluence (eF_{th}) at the first maximum diameter to be smaller than the ambient ionization threshold ($F_{ionization}$). If $eF_{th} > F_{ionization}$, the first maximum diameter will be affected as well, and the drilling diameter can be different from the prediction. Based on this, it can be suggested that whether the diameter is affected by ambient ionization depends on two quantities, namely, the material damage threshold F_{th} and the ambient ionization threshold $F_{ionization}$. For low F_{th} material and high $F_{ionization}$ ambient condition, ionization is difficult to occur before the first maximum diameter is reached, therefore, the diameter prediction will be accurate. For high F_{th} material and low $F_{ionization}$ ambient condition, ionization is easy to occur before the first maximum diameter is reached, and the diameter can be smaller than the prediction. Since $F_{ionization}$ of air is much higher than F_{th} of most materials, air ionization will not affect diameter prediction. For laser-based fabrication in liquid [187] (such as water), since the ambient ionization threshold is much lower, the impacts on the drilling diameter will be more significant, especially for high F_{th} material, such as fused silica.

6.3 Laser-based channel self-termination mechanisms

To better understand the channel aspect ratio variation with pulse energy and drilling speed, it is of particular significance to clarify the fundamental mechanisms of channel self-termination. As discussed in the introduction, most researchers believe debris accumulation is mainly responsible for channel self-termination, however, this hypothesis is questionable. In the following section, we propose alternative mechanisms and provide substantial verification on the rationality.

6.3.1 Early termination at nonoptimal drilling speeds

The ultrafast laser drilling and termination process is schematically demonstrated in Figure 6.8. A circular damage zone in the laser propagation direction is assumed in the focused Gaussian beam. At optimal drilling speeds, laser beam movement and material removal are maintained at the same paces and the damage zone will be located at the glass/air interface. Nonoptimal drilling speeds will introduce mismatch of laser beam movement and material removal and lead to early termination (reduced length) of channel drilling.

High drilling speeds will cause the material removal to lag behind the laser beam movement. The typical material removal rate by ultrafast laser pulses in fused silica is 100-300 nm per pulse and the corresponding drilling speed at 1 kHz is 100-300 μm/s. In Figure 6.8 (a), at higher drilling speeds than this range, the material removal cannot catch up with the laser beam movement and the lag will increase gradually. When the damage zone is above the channel head, there will be solid material in the lag to impede material removal

and the drilling process will be terminated. The lag between the laser beam movement and the channel head increases more rapidly at higher drilling speeds, and this results in earlier termination (shorter channels).

On the contrary, when the drilling speed is low, the material removal can always catch up with the laser beam movement. If the material along the drill path is transparent, continuous material removal is expected and long channels should be drilled. However, experiments suggest reduced channel lengths at low speeds. In reality, low drilling speeds introduce excessive laser irradiation, which can damage the material above the channel head and make this part nontransparent. This nontransparent material will shield the laser beam and terminate the drilling process. At decreasing drilling speeds, increasing laser irradiation is expected to cause earlier laser shielding and shorter channels.

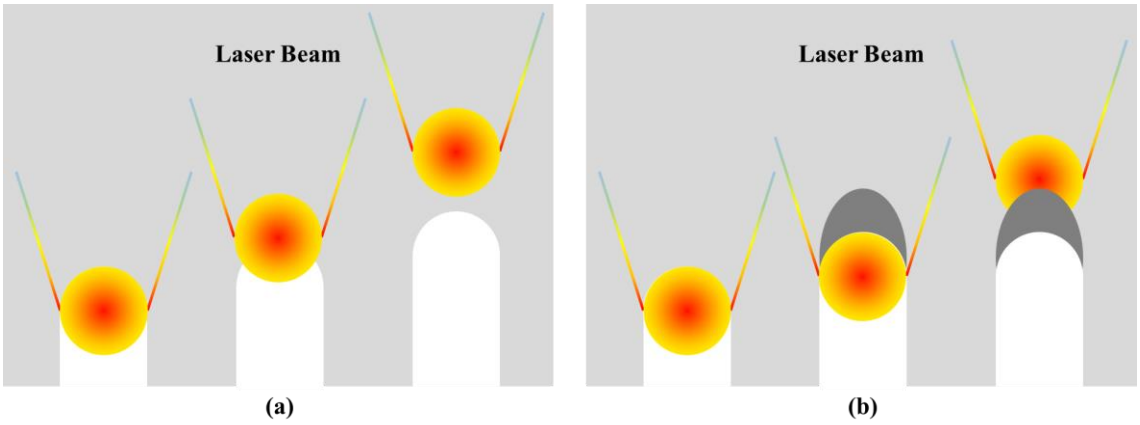

Figure 6.8 Schematic illustration of channel self-termination at (a) high and (b) low drilling speeds. The solid lines in color represent the laser beam focusing geometry, the colored areas represent the laser damage area in beam propagation direction and the dark-grey regions represent the modified material by repetitive laser pulses.

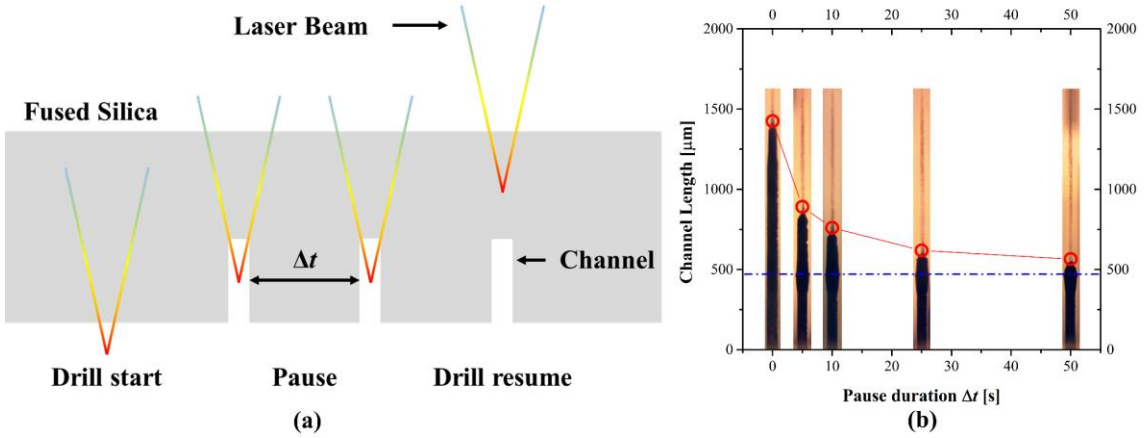

Figure 6.9 (a) Schematic illustration of interrupted laser drilling process. The solid lines in gradient colors represent the laser beam focusing geometry. (b) Channel length variation with different pause duration. The blue dash-dot line indicates the position where channel drilling is paused.

To examine this hypothesis, we performed another experiment at 270 μJ and 150 μm/s. The experiment is schematically displayed in Figure 6.9 (a). The channel is drilled and deliberately paused at a designated position before self-termination. The drilling process is resumed at the same speed afterwards. During the pause duration, laser pulses are still applied to mimic the excessive laser irradiation in low-speed drilling and longer pause duration corresponds to lower drilling speeds. If the hypothesis is valid, shorter channel should be expected with longer pause duration. Figure 6.9 (b) summarizes the channel lengths as a function of the pause duration. The channel drilled without pause (zero pause duration) is displayed for comparison. Monotonic decrease of channel length is observed with longer pause duration, and the channel with 50 seconds pause cannot further

drilled after the pause. This experiment provides additional validation on the proposed mechanism for early termination by low-speed drilling.

Early termination by nonoptimal drilling speeds is not triggered instantly by any single pulse. Both the lag at high speeds and material damage shielding at low speeds need to be accumulated by multiple pulses. Moreover, material removal rates during the whole drilling process may not be kept constant due to the inevitable incubation effect, however, drilling speeds are kept as constant. Therefore, same paces between the laser beam movement and material removal cannot be infinitely maintained and channel cannot be drilled infinitely long.

6.3.2 Damage shielding on front surface

Besides the dominating mechanism of channel self-termination in Section 6.3.1, there is a secondary mechanism as elaborated in the following section. When laser drills through the sample, there is an exit formed on the front surface. This front surface damage can start (hundreds of microns beneath the surface) before the arrival of the focal spot and terminate drilling process by shielding successive laser pulses. This mechanism is schematically demonstrated in Figure 6.10. When the laser beam is focused beneath the sample rear surface (Figure 6.10 (a)), the front surface laser fluence is much lower than the damage threshold. With upwards moving of the focal spot (Figure 6.10 (b)), the front surface fluence increases. Once this fluence is higher than the ablation threshold (Figure 6.10 (c)), front surface damage will be triggered. After that, the surface damage will block the laser beam (Figure 6.10 (d)), and the drilling process will be terminated (Figure 6.10

(e)). For thick samples (2.5 mm in this work), the impact of surface damage shielding is much less important, since most of the drilled channels are self-terminated before surface damage shielding takes effect. On the contrary, for samples of 1 mm thickness or less, this surface shielding effect will be the dominating mechanism to terminate drilling before self-termination occurs.

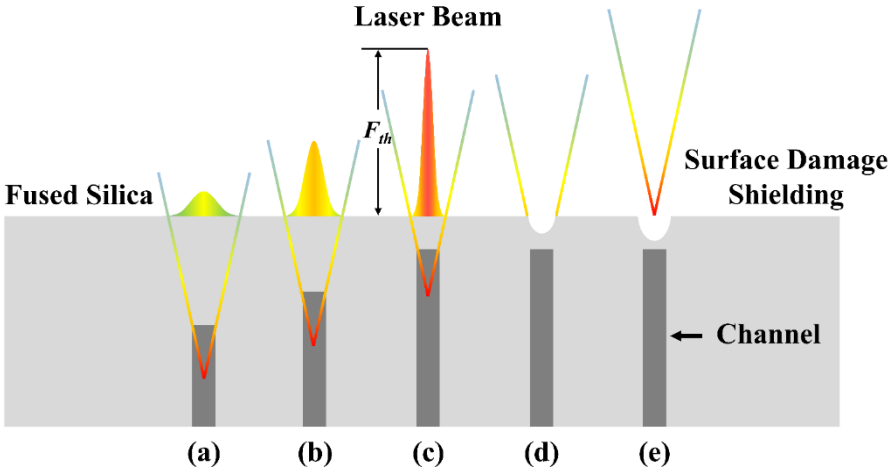

Figure 6.10 Schematic illustration of the rear-side drilling in fused silica. Surface damage (white semicircle) is formed on the front surface before the focal spot arrives at the front surface, shielding laser beam, and resulting in drilling termination.

6.4 Summary

This chapter presents ultrafast laser direct drilling of fused silica and highlighted the feasibility of high-aspect-ratio and high-quality channel direct drilling at high processing speeds (hundreds of micron per second). Uniform and taper-free microchannels have been achieved with maximum channel length over 2000 μm, aspect ratio as high as ~40:1 and excellent sidewall quality (roughness ~0.65 μm) at pulse energy of 270 μJ. Close

interrelation between pulse energy and drilling speed has been demonstrated in affecting channel aspect ratio. Optimal drilling speeds can be always observed at different pulse energy and these speeds increase at higher pulse energy, from 100 μm/s at 60 μJ to 300 μm/s at 480 μJ.

We proposed the dominating mechanism for channel self-termination as mismatch of material removal and laser beam movement under repetitive laser pulse irradiation. At higher drilling speed over optimal value, material removal cannot catch up with the motion of laser focal spot and drilling process terminates due to insufficient laser energy deposition. At lower drilling speed below optimal value, excessive laser irradiation induces structural modification above channel drilling front, therefore obstruct laser beam propagation and terminates the drilling process. We developed an analytical model to quantify laser-induced damage inside fused silica and provide substantial verification of this mechanism. Surface damage shielding is found to be a secondary mechanism for channel self-termination in thick samples (over 2 mm), however, this can be the dominating mechanism in thin samples (1 mm thickness or less).

CHAPTER SEVEN

CONCLUSIONS AND FUTURE WORKS

This chapter summarizes the conclusions in the current stage and discusses future works in the next stage.

7.1 Conclusions

Ultrafast laser ablation mechanisms and characteristics have been investigated for metals and dielectrics. Hybrid models have been developed based on combination of two-temperature model, plasma model, and molecular dynamics model to reveal fundamental physics during laser-material interaction. Material removal has been incorporated in two-temperature model to take account the thermal energy losses through particles ejection. Experiments have been conducted to study key factors in ultrafast laser ablation of dielectric materials.

Thermal and non-thermal (photomechanical) behaviors in micro-size metal films from irradiation of ultrafast laser pulse have been investigated based on combined continuum-atomistic approach, including phase explosion (thermal ablation) and spallation (non-thermal ablation). Coexistence of phase explosion and spallation has been observed for a considerably wide range of laser fluence, revealing the complicated interplay of different mechanisms in ultrafast laser-induced material decomposition. Phase explosion has higher threshold fluence than spallation, and becomes the dominating ablation mechanism with the increase of laser fluence. A dimensionless quantity, tension factor, has been introduced, based on which a universal criterion for the occurrence of spallation has

been proposed and validated. The tensile (spall) strength follows linear decrease with the increase of temperature below melting point, and the inverse exponential function can better agree with our measured strength in the liquid regime compared to previously proposed theoretical descriptions. At higher laser fluence over 0.5 J/cm^2, reduction in the spall strength can be observed, which should be mainly attributed to the structural deformation from the compressive process prior to the material breakdown under tension. Separate measurement of spall strength in the QI method considering pre-compression corroborate the observation in laser-induced spallation, implicate the considerable structural effect on the determination of spall strength. Dielectric material decomposition mechanisms are essentially similar to metals and semiconductors. However, since dielectric materials have much longer optical penetration depth (~100-200 nm) than metals (~10 nm) at 800 nm laser irradiation, non-linear absorption has to precede material heating, and the temperature gradient can be much lower, therefore the generated thermal-elastic stress is much weaker than in non-transparent materials at similar level of surface heating.

Plasma dynamics with respect to ejection direction and velocity have been studied based on fluorescence and shadowgraph images. Good agreements have been obtained between model predictions and measurements. The most probable direction (angle) is found not significantly affected by the laser fluence, indicating the plasma deposition process insensitive to laser fluence/energy. The plasma ejection velocity scales pretty well the root of electron temperature, which highlights the nature of thermal ablation in dielectric material decomposition by laser irradiation.

Ultrafast laser-induced ablation of dielectric materials has been investigated based on a one-dimensional plasma-temperature combined model. Numerical prediction of LIAT and ablation depth based on the proposed ablation criterion agree well with experimental observations. With the increase of pulse energy, ablation depth experiences sharp increase above ablation threshold, and tends to increase slowly. Further increase of energy brings about, however, decrease in ablation depth, which can be mainly attributed to plasma defocusing effect with non-equilibrium air ionization. With increasing pulse number from 1 to 100, the ablation rate can be increased by 100-150 nm with repetition rate below 1 kHz. While with higher repetition rate than 1 kHz to 10 kHz, more significant enhancement of ablation rate can be observed with multi-pulse irradiation, as high as 250 nm (almost double of the ablation rate at single pulse). This enhanced thermal accumulation effect by increasing repetition rate above 1 kHz can be well demonstrated by the simulation. For ULIA, especially for femtosecond laser pulses, low fluence manufacturing is proposed for high ablation efficiency and good microstructure quality. Consideration of beam divergence in calculation is observed to be more important for transparent than for opaque materials. The ablation enhancement with multiple pulse and increasing repetition rate provides valuable information to improve the processing and micromachining of dielectric materials with ultrafast laser pulses.

Ultrafast laser direct drilling of fused silica has been performed and the feasibility of high-aspect-ratio, high-quality and high-speed channel drilling has been highlighted. Uniform and taper-free microchannels have been achieved with maximum channel length over 2000 μm, aspect ratio as high as ~40:1 and excellent sidewall quality (roughness ~0.65

μm). Close interrelation between pulse energy and drilling speed has been demonstrated in affecting channel aspect ratio. Optimal drilling speeds can be always observed at different pulse energy and these speeds increase at higher pulse energy, from 100 μm/s at 60 μJ to 300 μm/s at 480 μJ.

The dominating mechanism for channel self-termination has been proposed as mismatch of material removal and laser beam movement under repetitive laser pulse irradiation. At higher drilling speed over optimal value, material removal cannot catch up with the motion of laser focal spot and drilling process terminates due to insufficient laser energy deposition. At lower drilling speed below optimal value, excessive laser irradiation induces structural modification above channel drilling front, therefore obstruct laser beam propagation and terminates the drilling process. An analytical model has been developed to quantify laser-induced damage inside fused silica and provide substantial validation of this mechanism. Surface damage shielding is found to be a secondary mechanism for channel self-termination in thick samples (over 2 mm), however, this can be the dominating mechanism in thin samples (1 mm thickness or less).

7.2 Future works

To better understand the laser-material interaction and micromachining processes, several subjects are proposed based on the current studies.

7.2.1 Ultrafast laser-based processing of transparent materials

A unique advantage of ultrafast laser processing is nonlinear absorption, which enables not only surface processing, but also three-dimensional (3D) internal microfabrication of transparent materials such as glass and polymers. My Ph.D. research has made me prepared with high-fidelity numerical models and rich experimental experiences on transparent material processing. In my future research, I would like to extend straight channel drilling to a series of other processes, including (but not limited to) cutting, marking, dicing and 3D internal structure fabrication, etc. Ultrafast laser will find great opportunities in fulfilling the foreseeable huge demands on transparent material processing. Meanwhile, prosperous industrial production with ultrafast laser is promising with the rapidly increasing application of novel transparent material, such as flexible display materials in mobile phone and variety of other consumer electronics, where high precision and minimized thermal effects are critical.

7.2.2 Dual-wavelength and double-pulse laser processing

During ultrafast laser fabrication, electrons are mainly responsible for energy absorption and thermal transportation, making transient electron dynamics the dominating factor in fabrication process. Ultrafast laser permits manipulation of electron dynamics through temporal and spatial shaping of laser pulses, which offers high flexibility and controllability in modification of material. In my future research, I propose to investigate double-pulse fabrication of material using independently controlled laser wavelengths. This approach does not only provide more flexibility and controllability in electron

dynamics but take advantage of both the high ionization rate of short wavelength (in ultraviolet) and high energy absorption of long wavelength (in infrared). This technique has great potential in improving machining precision, throughput, reproducibility, and controllability. I plan to perform surface machining for primary verification of the effectiveness and seek for implementation into other fabrication processes. If successful, this technique will find variety of applications, especially in processing of high-value and hard-to-machine materials for products requiring high precision, such as sapphire in mechanical watches and scratch resistant covers for precious devices.

7.2.3 Ultrahigh repetition rate (GHz) laser burst processing

Nowadays the relevance and the robustness of ultrafast lasers are well established for many industrial applications. The main limitation is the insufficient productivity compared to the needs of the application markets. Increasing the power, pulse energy or repetition rate of femtosecond lasers has been a general trend in order to comply to higher throughput. One of the strategies is the development of ultrahigh repetition rate (GHz) ultrafast laser. When increasing the repetition rate during the process beyond several hundred kHz, the delay between the laser pulses is less than the thermal relaxation time and there is thermal accumulation in the target material. The resulting rise in temperature leads to an ablation efficiency enhancement.

Current studies on this promising technique heavily rely on experimental studies. However, due to the complex setup, high/extra cost [188] and accuracy of experimental setup [188], the pulse number in burst, intra-burst repetition rates and burst/pulse fluence

are limited. Therefore, a comprehensive perspective towards the effectiveness of laser-burst technique is still missing and the fundamental mechanism is still unclear. To tackle this issue and promote the understanding of laser-burst ablation, I plan to develop a physics-based numerical model to study how laser burst interact with material and how ablation efficiency change with different burst conditions (pulse number, repetition rate, fluence). If successful, the results will provide comprehensive perspective on the fundamental mechanisms of laser burst material processing, therefore save a great amount of experimental efforts, and promote application of this technique in the manufacturing industry.

REFERENCES

[1] B.N. Chichkov, C. Momma, S. Nolte, F. Von Alvensleben, A. Tünnermann, Femtosecond, picosecond and nanosecond laser ablation of solids, Appl. Phys. A. 63 (1996) 109–115.

[2] M. Lenzner, F. Krausz, J. Krüger, W. Kautek, Photoablation with sub-10 fs laser pulses, Appl. Surf. Sci. 154 (2000) 11–16.

[3] www.photonics.com/Articles/Selecting_Industrial_Laser_ Optics.

[4] M. V. Shugaev, C. Wu, O. Armbruster, A. Naghilou, N. Brouwer, D.S. Ivanov, T.J.Y. Derrien, N.M. Bulgakova, W. Kautek, B. Rethfeld, L. V. Zhigilei, Fundamentals of ultrafast laser-material interaction, MRS Bull. 41 (2016) 960–968.

[5] D. Perez, L.J. Lewis, Molecular-dynamics study of ablation of solids under femtosecond laser pulses, Phys. Rev. B. 67 (2003) 184102.

[6] F. Vidal, T.W. Johnston, S. Laville, O. Barthélemy, M. Chaker, B. Le Drogoff, J. Margot, M. Sabsabi, Critical-point phase separation in laser ablation of conductors, Phys. Rev. Lett. 86 (2001) 2573–2576.

[7] D. Perez, L.J. Lewis, Ablation of Solids under Femtosecond Laser Pulses, Phys. Rev. Lett. 89 (2002) 255504.

[8] R. Stoian, D. Ashkenasi, A. Rosenfeld, E.E.B. Campbell, Coulomb explosion in ultrashort pulsed laser ablation of Al2O3, Phys. Rev. B. 62 (2000) 13167–13173.

[9] R. Stoian, A. Rosenfeld, D. Ashkenasi, I. V. Hertel, N.M. Bulgakova, E.E. Campbell, Surface charging and impulsive ion ejection during ultrashort pulsed laser ablation, Phys. Rev. Lett. 88 (2002) 097603.

[10] L.J. Lewis, D. Perez, Laser ablation with short and ultrashort laser pulses: Basic mechanisms from molecular-dynamics simulations, Appl. Surf. Sci. 255 (2009) 5101–5106.

[11] S.K. Sundaram, E. Mazur, Inducing and probing non-thermal transitions in semiconductors using femtosecond laser pulses, Nat. Mater. 1 (2002) 217–224.

[12] S. Anisimov, B. Kapeliovich, T. Perel'Man, Electron emission from metal surfaces exposed to ultrashort laser pulses, Sov. J. Exp. Theor. Phys. 39 (1974) 776–781.

[13] T.Q. Qiu, C.L. Tien, Heat transfer mechanisms during short-pulse laser heating of metals, J. Heat Transfer. 115 (1993) 835–841.

[14] D.Y. Tzou, A unified field approach for heat conduction from macro- to micro-scales, J. Heat Transfer. 117 (1995) 8–16.

[15] J.K. Chen, J.E. Beraun, Modelling of ultrashort laser ablation of gold films in vacuum, J. Opt. A Pure Appl. Opt. 5 (2003) 168–173.

[16] J.K. Chen, D.Y. Tzou, J.E. Beraun, A semiclassical two-temperature model for ultrafast laser heating, Int. J. Heat Mass Transf. 49 (2006) 307–316.

[17] T.E. Itina, J. Hermann, P. Delaporte, M. Sentis, Modeling of metal ablation induced by ultrashort laser pulses, Thin Solid Films. 453–454 (2004) 513–517.

[18] B. Wu, Y.C. Shin, A simple model for high fluence ultra-short pulsed laser metal ablation, Appl. Surf. Sci. 253 (2007) 4079–4084.

[19] J.P. Colombier, P. Combis, F. Bonneau, R. Le Harzic, E. Audouard, Hydrodynamic simulations of metal ablation by femtosecond laser irradiation, Phys. Rev. B. 71 (2005) 165406.

[20] N.M. Bulgakova, A. Rosenfeld, L. Ehrentraut, R. Stoian, I. V. Hertel, Modeling of electron dynamics in laser-irradiated solids: progress achieved through a continuum approach and future prospects, in: V.Y. Panchenko, O.A. Louchev, S. Malyshev (Eds.), Int. Conf. Lasers, Appl. Technol. 2007 Laser-Assisted Micro-Nanotechnologies, SPIE, 2007: p. 673208.

[21] X. Zhao, Y.C. Shin, A two-dimensional comprehensive hydrodynamic model for femtosecond laser pulse interaction with metals, J. Phys. D. Appl. Phys. 45 (2012) 105201.

[22] L. V. Zhigilei, B.J. Garrison, Microscopic mechanisms of laser ablation of organic solids in the thermal and stress confinement irradiation regimes, J. Appl. Phys. 88 (2000) 1281–1298.

[23] W. Hu, Y.C. Shin, G. King, Energy transport analysis in ultrashort pulse laser ablation through combined molecular dynamics and Monte Carlo simulation, Phys. Rev. B. 82 (2010) 094111.

[24] X. Zhao, Y.C. Shin, Ablation enhancement of silicon by ultrashort double-pulse laser ablation, Appl. Phys. Lett. 105 (2014) 111907.

[25] B.C. Stuart, M.D. Feit, A.M. Rubenchik, B.W. Shore, M.D. Perry, Laser-induced damage in dielectrics with nanosecond to subpicosecond pulses, Phys. Rev. Lett. 74 (1995) 2248–2251.

[26] P. Martin, S. Guizard, P. Daguzan, G. Petite, P. D'Oliveira, P. Meynadier, M. Perdrix, Subpicosecond study of carrier trapping dynamics in wide-band-gap crystals, Phys. Rev. B. 55 (1997) 5799–5810.

[27] M. Li, S. Menon, J.P. Nibarger, G.N. Gibson, Ultrafast electron dynamics in femtosecond optical breakdown of dielectrics, Phys. Rev. Lett. 82 (1999) 2394–2397.

[28] T.Q. Jia, Z.Z. Xu, X.X. Li, R.X. Li, B. Shuai, F.L. Zhao, Microscopic mechanisms of ablation and micromachining of dielectrics by using femtosecond lasers, Appl. Phys. Lett. 82 (2003) 4382–4384.

[29] B. Rethfeld, Unified model for the free-electron avalanche in laser-irradiated dielectrics, Phys. Rev. Lett. 92 (2004) 187401.

[30] B. Rethfeld, Free-electron generation in laser-irradiated dielectrics, Phys. Rev. B. 73 (2006) 035101.

[31] B.H. Christensen, P. Balling, Modeling ultrashort-pulse laser ablation of dielectric materials, Phys. Rev. B. 79 (2009) 155424.

[32] L. Jiang, H.L. Tsai, A plasma model combined with an improved two-temperature equation for ultrafast laser ablation of dielectrics, J. Appl. Phys. 104 (2008) 093101.

[33] B. Wu, Y.C. Shin, A simplified predictive model for high-fluence ultra-short pulsed laser ablation of semiconductors and dielectrics, Appl. Surf. Sci. 255 (2009) 4996–5002.

[34] K. Sugioka, Y. Cheng, Ultrafast lasers—reliable tools for advanced materials processing, Light Sci. Appl. 3 (2014) e149.

[35] L. Shah, A.Y. Arai, S.M. Eaton, P.R. Herman, Waveguide writing in fused silica with a femtosecond fiber laser at 522 nm and 1 MHz repetition rate, Opt. Express. 13 (2005) 1999–2006.

[36] L. Guo, H. Xia, H.-T. Fan, Y.-L. Zhang, Q.-D. Chen, T. Zhang, H.-B. Sun, Femtosecond laser direct patterning of sensing materials toward flexible integration of micronanosensors, Opt. Lett. 35 (2010) 1695–1697.

[37] V. Maselli, R. Osellame, G. Cerullo, R. Ramponi, P. Laporta, L. Magagnin, P.L. Cavallotti, Fabrication of long microchannels with circular cross section using astigmatically shaped femtosecond laser pulses and chemical etching, Appl. Phys. Lett. 88 (2006) 191107.

[38] S. Kiyama, S. Matsuo, S. Hashimoto, Y. Morihira, Examination of etching agent and etching mechanism on femotosecond laser microfabrication of channels inside vitreous silica substrates, J. Phys. Chem. C. 113 (2009) 11560–11566.

[39] S. Loturco, R. Osellame, R. Ramponi, K.C. Vishnubhatla, Hybrid chemical etching of femtosecond laser irradiated structures for engineered microfluidic devices, J. Micromechanics Microengineering. 23 (2013) 085002.

[40] A. Marcinkevičius, S. Juodkazis, M. Watanabe, M. Miwa, S. Matsuo, H. Misawa, J. Nishii, Femtosecond laser-assisted three-dimensional microfabrication in silica, Opt. Lett. 26 (2001) 277–279.

[41] Y. Bellouard, A. Said, M. Dugan, P. Bado, Fabrication of high-aspect ratio, micro-fluidic channels and tunnels using femtosecond laser pulses and chemical etching, Opt. Express. 12 (2004) 2120–2129.

[42] S. Ho, M. Haque, P.R. Herman, J.S. Aitchison, Femtosecond laser-assisted etching of three-dimensional inverted-woodpile structures in fused silica, Opt. Lett. 37 (2012) 1682–1684.

[43] R. Osellame, V. Maselli, R.M. Vazquez, R. Ramponi, G. Cerullo, Integration of optical waveguides and microfluidic channels both fabricated by femtosecond laser irradiation, Appl. Phys. Lett. 90 (2007) 231118.

[44] C. Hnatovsky, R.S. Taylor, E. Simova, P.P. Rajeev, D.M. Rayner, V.R. Bhardwaj, P.B. Corkum, Fabrication of microchannels in glass using focused femtosecond laser radiation and selective chemical etching, Appl. Phys. A. 84 (2006) 47–61.

[45] M. Zhao, J. Hu, L. Jiang, K. Zhang, P. Liu, Y. Lu, Controllable high-throughput high-quality femtosecond laser-enhanced chemical etching by temporal pulse shaping based on electron density control, Sci. Rep. 5 (2015) 13202.

[46] Y. Li, K. Itoh, W. Watanabe, K. Yamada, D. Kuroda, J. Nishii, Y. Jiang, Three-dimensional hole drilling of silica glass from the rear surface with femtosecond laser pulses, Opt. Lett. 26 (2001) 1912–1914.

[47] S. Karimelahi, L. Abolghasemi, P.R. Herman, Rapid micromachining of high aspect ratio holes in fused silica glass by high repetition rate picosecond laser, Appl. Phys. A. 114 (2014) 91–111.

[48] L. Jiang, P. Liu, X. Yan, N. Leng, C. Xu, H. Xiao, Y. Lu, High-throughput rear-surface drilling of microchannels in glass based on electron dynamics control using femtosecond pulse trains, Opt. Lett. 37 (2012) 2781–2783.

[49] X. Zhao, Y.C. Shin, Femtosecond laser drilling of high-aspect ratio microchannels in glass, Appl. Phys. A. 104 (2011) 713–719.

[50] X. Liu, N. Sanner, M. Sentis, R. Stoian, W. Zhao, G. Cheng, O. Utéza, Front-surface fabrication of moderate aspect ratio micro-channels in fused silica by single picosecond Gaussian–Bessel laser pulse, Appl. Phys. A. 124 (2018) 206.

[51] B. Xia, L. Jiang, X. Li, X. Yan, W. Zhao, Y. Lu, High aspect ratio, high-quality microholes in PMMA: a comparison between femtosecond laser drilling in air and in vacuum, Appl. Phys. A. 119 (2015) 61–68.

[52] L. Jiang, J. Fang, Q. Cao, K. Zhang, P. Wang, Y. Yu, Q. Huang, Y. Lu, Femtosecond laser high-efficiency drilling of high-aspect-ratio microholes based on free-electron-density adjustments, Appl. Opt. 53 (2014) 7290–7295.

[53] M.K. Bhuyan, F. Courvoisier, P.-A. Lacourt, M. Jacquot, L. Furfaro, M.J. Withford, J.M. Dudley, High aspect ratio taper-free microchannel fabrication using femtosecond Bessel beams, Opt. Express. 18 (2010) 566–574.

[54] X. Yu, M. Zhang, S. Lei, Multiphoton polymerization using femtosecond bessel beam for layerless three-dimensional printing, J. Micro Nano-Manufacturing. 6 (2018) 010901.

[55] M.K. Bhuyan, P.K. Velpula, J.P. Colombier, T. Olivier, N. Faure, R. Stoian, Single-shot high aspect ratio bulk nanostructuring of fused silica using chirp-controlled ultrafast laser Bessel beams, Appl. Phys. Lett. 104 (2014) 021107.

[56] O. Jedrkiewicz, S. Kumar, B. Sotillo, M. Bollani, A. Chiappini, M. Ferrari, R. Ramponi, P. Di Trapani, S.M. Eaton, Pulsed Bessel beam-induced microchannels on a diamond surface for versatile microfluidic and sensing applications, Opt. Mater. Express. 7 (2017) 1962–1970.

[57] Z. Wang, L. Jiang, X. Li, A. Wang, Z. Yao, K. Zhang, Y. Lu, High-throughput microchannel fabrication in fused silica by temporally shaped femtosecond laser Bessel-beam-assisted chemical etching, Opt. Lett. 43 (2018) 98–101.

[58] C. Lin, Z. Rao, L. Jiang, W. Tsai, P. Wu, C. Chien, S. Chen, H. Tsai, Investigations of femtosecond–nanosecond dual-beam laser ablation of dielectrics, Opt. Lett. 35 (2010) 2490–2492.

[59] Y. Ito, R. Yoshizaki, N. Miyamoto, N. Sugita, Ultrafast and precision drilling of glass by selective absorption of fiber-laser pulse into femtosecond-laser-induced filament, Appl. Phys. Lett. 113 (2018) 061101.

[60] L. Englert, M. Wollenhaupt, L. Haag, C. Sarpe-Tudoran, B. Rethfeld, T. Baumert, Material processing of dielectrics with temporally asymmetric shaped femtosecond laser pulses on the nanometer scale, Appl. Phys. A. 92 (2008) 749–753.

[61] L. Englert, B. Rethfeld, L. Haag, M. Wollenhaupt, C. Sarpe-Tudoran, T. Baumert, Control of ionization processes in high band gap materials via tailored femtosecond pulses, Opt. Express. 15 (2007) 17855–17862.

[62] R.M. More, K.H. Warren, D.A. Young, G.B. Zimmerman, A new quotidian equation of state (QEOS) for hot dense matter, Phys. Fluids. 31 (1988) 3059–3078.

[63] Y.T. Lee, R.M. More, An electron conductivity model for dense plasmas, Phys. Fluids. 27 (1984) 1273–1286.

[64] S. Laville, F. Vidal, T.W. Johnston, O. Barthélemy, M. Chaker, B. Le Drogoff, J. Margot, M. Sabsabi, Fluid modeling of the laser ablation depth as a function of the pulse duration for conductors, Phys. Rev. E. 66 (2002) 066415.

[65] F. Quéré, S. Guizard, P. Martin, Time-resolved study of laser-induced breakdown in dielectrics, Europhys. Lett. 56 (2001) 138–144.

[66] G. Grosso, G.P. Parravicini, Solid State Physics, Academic Press, Oxford, 2014.

[67] K. Eidmann, J. Meyer-Ter-Vehn, T. Schlegel, S. Hüller, Hydrodynamic simulation of subpicosecond laser interaction with solid-density matter, Phys. Rev. E. 62 (2000) 1202–1214.

[68] J.R. Peñano, P. Sprangle, B. Hafizi, W. Manheimer, A. Zigler, Transmission of intense femtosecond laser pulses into dielectrics, Phys. Rev. E. 72 (2005) 036412.

[69] M. Fox, Optical Properties of Solids, Oxford University Press, Oxford, 2005.

[70] D. Grojo, M. Gertsvolf, S. Lei, T. Barillot, D.M. Rayner, P.B. Corkum, Exciton-seeded multiphoton ionization in bulk SiO2, Phys. Rev. B. 81 (2010) 212301.

[71] S.S. Mao, F. Quéré, S. Guizard, X. Mao, R.E. Russo, G. Petite, P. Martin, Dynamics of femtosecond laser interactions with dielectrics, Appl. Phys. A. 79 (2004) 1695–1709.

[72] I. Mirza, N.M. Bulgakova, J. Tomáštík, V. Michálek, O. Haderka, L. Fekete, T. Mocek, Ultrashort pulse laser ablation of dielectrics: Thresholds, mechanisms, role of breakdown, Sci. Rep. 6 (2016) 39133.

[73] L.A. Emmert, M. Mero, W. Rudolph, Modeling the effect of native and laser-induced states on the dielectric breakdown of wide band gap optical materials by multiple subpicosecond laser pulses, J. Appl. Phys. 108 (2010) 043523.

[74] B. Chimier, O. Utéza, N. Sanner, M. Sentis, T. Itina, P. Lassonde, F. Légaré, F. Vidal, J.C. Kieffer, Damage and ablation thresholds of fused-silica in femtosecond regime, Phys. Rev. B. 84 (2011) 094104.

[75] L. V. Keldysh, Ionization in the Field of a Strong Electromagnetic Wave, Sov. J. Exp. Theor. Phys. 20 (1965) 1307–1314.

[76] L.V. Keldysh, Kinetic theory of impact ionization in semiconductors, Sov. J. Exp. Theor. Phys. 37 (1960) 509–518.

[77] D.S. Ivanov, L. V. Zhigilei, Effect of Pressure Relaxation on the Mechanisms of Short-Pulse Laser Melting, Phys. Rev. Lett. 91 (2003) 105701.

[78] C. Schäfer, H.M. Urbassek, L. V. Zhigilei, Metal ablation by picosecond laser pulses: A hybrid simulation, Phys. Rev. B. 66 (2002) 115404.

[79] C. Cheng, X. Xu, Mechanisms of decomposition of metal during femtosecond laser ablation, Phys. Rev. B. 72 (2005) 165415.

[80] M.E. Povarnitsyn, V.B. Fokin, P.R. Levashov, T.E. Itina, Molecular dynamics simulation of subpicosecond double-pulse laser ablation of metals, Phys. Rev. B. 92 (2015) 174104.

[81] D. Ivanov, L. Zhigilei, Combined atomistic-continuum modeling of short-pulse laser melting and disintegration of metal films, Phys. Rev. B. 68 (2003) 064114.

[82] S. Plimpton, Fast parallel algorithms for short-range molecular dynamics, J. Comput. Phys. 117 (1995) 1–19.

[83] M.S. Daw, M.I. Baskes, Embedded-atom method: Derivation and application to impurities, surfaces, and other defects in metals, Phys. Rev. B. 29 (1984) 6443–6453.

[84] Y. Mishin, M.J. Mehl, D.A. Papaconstantopoulos, A.F. Voter, J.D. Kress, Structural stability and lattice defects in copper: Ab initio, tight-binding, and embedded-atom calculations, Phys. Rev. B. 63 (2001) 224106.

[85] S.N. Luo, Q. An, T.C. Germann, L.B. Han, Shock-induced spall in solid and liquid Cu at extreme strain rates, J. Appl. Phys. 106 (2009) 013502.

[86] A. Carré, J. Horbach, S. Ispas, W. Kob, New fitting scheme to obtain effective potential from Car-Parrinello molecular-dynamics simulations: Application to silica, Europhys. Lett. 82 (2008) 17001.

[87] F. Barmes, L. Soulard, M. Mareschal, Molecular dynamics of shock-wave induced structural changes in silica glasses, Phys. Rev. B. 73 (2006) 224108.

[88] B. Coluzzi, P. Verrocchio, The liquid-glass transition of silica, J. Chem. Phys. 116 (2002) 3789–3794.

[89] Y. Guissani, B. Guillot, A numerical investigation of the liquid-vapor coexistence curve of silica, J. Chem. Phys. 104 (1996) 7633–7644.

[90] K. Vollmayr, W. Kob, K. Binder, Cooling-rate effects in amorphous silica: A computer-simulation study, Phys. Rev. B. 54 (1996) 15808–15827.

[91] D. Wolf, P. Keblinski, S.R. Phillpot, J. Eggebrecht, Exact method for the simulation of Coulombic systems by spherically truncated, pairwise r-1 summation, J. Chem. Phys. 110 (1999) 8254–8282.

[92] P.P. Ewald, Die Berechnung optischer und elektrostatischer Gitterpotentiale, Ann. Phys. 369 (1921) 253–287.

[93] R. Renou, L. Soulard, E. Lescoute, C. Dereure, D. Loison, J.P. Guin, Silica Glass Structural Properties under Elastic Shock Compression: Experiments and Molecular Simulations, J. Phys. Chem. C. 121 (2017) 13324–13334.

[94] B.J. Demaske, V. V. Zhakhovsky, N.A. Inogamov, I.I. Oleynik, Ablation and spallation of gold films irradiated by ultrashort laser pulses, Phys. Rev. B. 82 (2010) 064113.

[95] Y. Cao, Y.C. Shin, Multi-scale modeling of phase explosion in high fluence nanosecond laser ablation and clarification of ablation depth prediction criterion, Appl. Surf. Sci. 357 (2015) 74–85.

[96] B.J. Garrison, T.E. Itina, L. V. Zhigilei, Limit of overheating and the threshold behavior in laser ablation, Phys. Rev. E. 68 (2003) 041501.

[97] L. V. Zhigilei, Z. Lin, D.S. Ivanov, Atomistic modeling of short pulse laser ablation of metals: Connections between melting, spallation, and phase explosion, J. Phys. Chem. C. 113 (2009) 11892–11906.

[98] C. Cheng, X. Xu, Molecular dynamics calculation of critical point of nickel, Int. J. Thermophys. 28 (2007) 9–19.

[99] J.A. Cahill, A.D. Kirshenbaum, The density of liquid copper from its melting point (1356°K.) to 2500°K. and an estimate of its critical constants, J. Phys. Chem. 66 (1962) 1080–1082.

[100] R. Kelly, A. Miotello, Comments on explosive mechanisms of laser sputtering, Appl. Surf. Sci. 96–98 (1996) 205–215.

[101] N.M. Bulgakova, R. Stoian, A. Rosenfeld, I. V. Hertel, W. Marine, E.E.B. Campbell, A general continuum approach to describe fast electronic transport in pulsed laser irradiated materials: The problem of Coulomb explosion, Appl. Phys. A. 81 (2005) 345–356.

[102] X. Zhao, Y.C. Shin, Femtosecond laser ablation of aluminum in vacuum and air at high laser intensity, Appl. Surf. Sci. 283 (2013) 94–99.

[103] J.L. Shao, P. Wang, A.M. He, R. Zhang, C. Sen Qin, Spall strength of aluminium single crystals under high strain rates: Molecular dynamics study, J. Appl. Phys. 114 (2013) 173501.

[104] D.E. Grady, The spall strength of condensed matter, J. Mech. Phys. Solids. 36 (1988) 353–384.

[105] M.E. Povarnitsyn, T.E. Itina, M. Sentis, K. V. Khishchenko, P.R. Levashov, Material decomposition mechanisms in femtosecond laser interactions with metals, Phys. Rev. B. 75 (2007) 235414.

[106] S.N. Luo, T.C. Germann, D.L. Tonks, Spall damage of copper under supported and decaying shock loading, J. Appl. Phys. 106 (2009) 123518.

[107] J.P. Cuq-Lelandais, M. Boustie, L. Berthe, T. De Rességuier, P. Combis, J.P. Colombier, M. Nivard, A. Claverie, Spallation generated by femtosecond laser driven shocks in thin metallic targets, J. Phys. D. Appl. Phys. 42 (2009) 065402.

[108] H. Jarmakani, B. Maddox, C.T. Wei, D. Kalantar, M.A. Meyers, Laser shock-induced spalling and fragmentation in vanadium, Acta Mater. 58 (2010) 4604–4628.

[109] V. V. Zhakhovskii, N.A. Inogamov, Y. V. Petrov, S.I. Ashitkov, K. Nishihara, Molecular dynamics simulation of femtosecond ablation and spallation with different interatomic potentials, Appl. Surf. Sci. 255 (2009) 9592–9596.

[110] P. Wen, G. Tao, C. Pang, S. Yuan, Q. Wang, A molecular dynamics study of the shock-induced defect microstructure in single crystal Cu, Comput. Mater. Sci. 124 (2016) 304–310.

[111] M.A. Meyers, F. Gregori, B.K. Kad, M.S. Schneider, D.H. Kalantar, B.A. Remington, G. Ravichandran, T. Boehly, J.S. Wark, Laser-induced shock compression of monocrystalline copper: Characterization and analysis, Acta Mater. 51 (2003) 1211–1228.

[112] D. Seif, G. Po, R. Crum, V. Gupta, N.M. Ghoniem, Shock-induced plasticity and the Hugoniot elastic limit in copper nano films and rods, J. Appl. Phys. 115 (2014) 054301.

[113] X.H. Chen, L. Lu, K. Lu, Grain size dependence of tensile properties in ultrafine-grained Cu with nanoscale twins, Scr. Mater. 64 (2011) 311–314.

[114] L. Lu, Y. Shen, X. Chen, L. Qian, K. Lu, Ultrahigh Strength and High Electrical Conductivity in Copper, Science 304 (2004) 422–426.

[115] K. Mackenchery, R.R. Valisetty, R.R. Namburu, A. Stukowski, A.M. Rajendran, A.M. Dongare, Dislocation evolution and peak spall strengths in single crystal and nanocrystalline Cu, J. Appl. Phys. 119 (2016) 044301.

[116] E.N. Hahn, S.J. Fensin, T.C. Germann, G.T. Gray, Orientation dependent spall strength of tantalum single crystals, Acta Mater. 159 (2018) 241–248.

[117] S.J. Fensin, S.M. Valone, E.K. Cerreta, J.P. Escobedo-Diaz, G.T. Gray, K. Kang, J. Wang, Effect of grain boundary structure on plastic deformation during shock compression using molecular dynamics, Model. Simul. Mater. Sci. Eng. 21 (2013) 015011.

[118] T.P. Remington, E.N. Hahn, S. Zhao, R. Flanagan, J.C.E. Mertens, S. Sabbaghianrad, T.G. Langdon, C.E. Wehrenberg, B.R. Maddox, D.C. Swift, B.A. Remington, N. Chawla, M.A. Meyers, Spall strength dependence on grain size and strain rate in tantalum, Acta Mater. 158 (2018) 313–329.

[119] C. Schäfer, H.M. Urbassek, L. V. Zhigilei, B.J. Garrison, Pressure-transmitting boundary conditions for molecular-dynamics simulations, Comput. Mater. Sci. 24 (2002) 421–429.

[120] P. Vashishta, R.K. Kalia, J.P. Rino, I. Ebbsjö, Interaction potential for SiO2: A molecular-dynamics study of structural correlations, Phys. Rev. B. 41 (1990) 12197–12209.

[121] R.L. Mozzi, B.E. Warren, The structure of vitreous silica, J. Appl. Crystallogr. 2 (1969) 164–172.

[122] D.I. Grimley, A.C. Wright, R.N. Sinclair, Neutron scattering from vitreous silica IV. Time-of-flight diffraction, J. Non. Cryst. Solids. 119 (1990) 49–64.

[123] A. Pedone, G. Malavasi, M. Cristina Menziani, U. Segre, A.N. Cormack, Molecular dynamics studies of stress-strain behavior of silica glass under a tensile load, Chem. Mater. 20 (2008) 4356–4366.

[124] F. Yuan, L. Huang, Molecular dynamics simulation of amorphous silica under uniaxial tension: From bulk to nanowire, J. Non. Cryst. Solids. 358 (2012) 3481–3487.

[125] S.C. Chowdhury, B.Z. (Gama. Haque, J.W. Gillespie, Molecular dynamics simulations of the structure and mechanical properties of silica glass using ReaxFF, J. Mater. Sci. 51 (2016) 10139–10159.

[126] A.C.T. Van Duin, S. Dasgupta, F. Lorant, W.A. Goddard, ReaxFF: A reactive force field for hydrocarbons, J. Phys. Chem. A. 105 (2001) 9396–9409.

[127] P.B. Corkum, F. Brunel, N.K. Sherman, T. Srinivasan-Rao, Thermal response of metals to ultrashort-pulse laser excitation, Phys. Rev. Lett. 61 (1988) 2886–2889.

[128] E.G. Gamaly, A. V. Rode, B. Luther-Davies, V.T. Tikhonchuk, Ablation of solids by femtosecond lasers: Ablation mechanism and ablation thresholds for metals and dielectrics, Phys. Plasmas. 9 (2002) 949.

[129] M. Mero, J. Liu, W. Rudolph, D. Ristau, K. Starke, Scaling laws of femtosecond laser pulse induced breakdown in oxide films, Phys. Rev. B. 71 (2005) 115109.

[130] A.C. Tien, S. Backus, H. Kapteyn, M. Murnane, G. Mourou, Short-pulse laser damage in transparent materials as a function of pulse duration, Phys. Rev. Lett. 82 (1999) 3883–3886.

[131] H. Varel, D. Ashkenasi, A. Rosenfeld, R. Herrmann, F. Noack, E.E.B. Campbell, Laser-induced damage in SiO2 and CaF2 with picosecond and femtosecond laser pulses, Appl. Phys. A. 62 (1996) 293–294.

[132] P. Lorazo, L.J. Lewis, M. Meunier, Short-pulse laser ablation of solids: From phase explosion to fragmentation, Phys. Rev. Lett. 91 (2003) 225502.

[133] I. Iosilevskiy, V. Gryaznov, A. Solov'ev, Properties of high-temperature phase diagram and critical point parameters in silica, High Temp. - High Press. 43 (2013) 227–241.

[134] J.A.D. Connolly, Liquid-vapor phase relations in the Si-O system: A calorically constrained van der Waals-type model, J. Geophys. Res. Planets. 121 (2016) 1641–1666.

[135] S. Faik, A. Tauschwitz, I. Iosilevskiy, The equation of state package FEOS for high energy density matter, Comput. Phys. Commun. 227 (2018) 117–125.

[136] D.A. Young, B.J. Alder, Critical point of metals from the van der Waals model, Phys. Rev. A. 3 (1971) 364–371.

[137] N.S. Shcheblanov, M.E. Povarnitsyn, Bond-breaking mechanism of vitreous silica densification by IR femtosecond laser pulses, Europhys. Lett. 114 (2016) 26004.

[138] L. Zheng, J.C. Lambropoulos, A.W. Schmid, UV-laser-induced densification of fused silica: A molecular dynamics study, J. Non. Cryst. Solids. 347 (2004) 144–152.

[139] M. Garcia-Lechuga, J. Siegel, J. Hernandez-Rueda, J. Solis, Femtosecond laser ablation of dielectric materials in the optical breakdown regime: Expansion of a transparent shell, Appl. Phys. Lett. 105 (2014) 112902.

[140] M. Garcia-Lechuga, J. Solis, J. Siegel, Key stages of material expansion in dielectrics upon femtosecond laser ablation revealed by double-color illumination time-resolved microscopy, Appl. Phys. A. 124 (2018) 221.

[141] T. Kumada, T. Otobe, M. Nishikino, N. Hasegawa, T. Hayashi, Dynamics of spallation during femtosecond laser ablation studied by time-resolved reflectivity with double pump pulses, Appl. Phys. Lett. 108 (2016) 011102.

[142] P. Lorazo, L.J. Lewis, M. Meunier, Thermodynamic pathways to melting, ablation, and solidification in absorbing solids under pulsed laser irradiation, Phys. Rev. B. 73 (2006) 134108.

[143] E.N. Hahn, T.C. Germann, R. Ravelo, J.E. Hammerberg, M.A. Meyers, On the ultimate tensile strength of tantalum, Acta Mater. 126 (2017) 313–328.

[144] B.C. Stuart, M.D. Feit, S. Herman, A.M. Rubenchik, B.W. Shore, M.D. Perry, Optical ablation by high-power short-pulse lasers, J. Opt. Soc. Am. B. 13 (1996) 459–468.

[145] D. Puerto, J. Siegel, W. Gawelda, M. Galvan-Sosa, L. Ehrentraut, J. Bonse, J. Solis, Dynamics of plasma formation, relaxation, and topography modification induced by femtosecond laser pulses in crystalline and amorphous dielectrics, J. Opt. Soc. Am. B. 27 (2010) 1065–1076.

[146] N. Sanner, O. Utéza, B. Bussiere, G. Coustillier, A. Leray, T. Itina, M. Sentis, Measurement of femtosecond laser-induced damage and ablation thresholds in dielectrics, Appl. Phys. A. 94 (2009) 889–897.

[147] J.M. Liu, Simple technique for measurements of pulsed Gaussian-beam spot sizes, Opt. Lett. 7 (1982) 196–198.

[148] F. Di Niso, C. Gaudiuso, T. Sibillano, F.P. Mezzapesa, A. Ancona, P.M. Lugarà, Role of heat accumulation on the incubation effect in multi-shot laser ablation of stainless steel at high repetition rates, Opt. Express. 22 (2014) 12200–12210.

[149] C. Gaudiuso, G. Giannuzzi, A. Volpe, P.M. Lugarà, I. Choquet, A. Ancona, Incubation during laser ablation with bursts of femtosecond pulses with picosecond delays, Opt. Express. 26 (2018) 3801–3813.

[150] D. Ashkenasi, M. Lorenz, R. Stoian, A. Rosenfeld, Surface damage threshold and structuring of dielectrics using femtosecond laser pulses: the role of incubation, Appl. Surf. Sci. 150 (1999) 101–106.

[151] Z. Sun, M. Lenzner, W. Rudolph, Generic incubation law for laser damage and ablation thresholds, J. Appl. Phys. 117 (2015) 073102.

[152] Y. Jee, M.F. Becker, R.M. Walser, Laser-induced damage on single-crystal metal surfaces, J. Opt. Soc. Am. B. 5 (1988) 648–659.

[153] M. Lebugle, N. Sanner, N. Varkentina, M. Sentis, O. Utéza, Dynamics of femtosecond laser absorption of fused silica in the ablation regime, J. Appl. Phys. 116 (2014) 063105.

[154] M. Lebugle, O. Utéza, M. Sentis, N. Sanner, High temporal resolution and calibration in pump–probe experiments characterizing femtosecond laser–dielectrics interaction, Appl. Phys. A. 120 (2015) 455–461.

[155] C. Kerse, H. Kalaycloğlu, P. Elahi, B. Çetin, D.K. Kesim, Ö. Akçaalan, S. Yavaş, M.D. Aşlk, B. Öktem, H. Hoogland, R. Holzwarth, F.Ö. Ilday, Ablation-cooled material removal with ultrafast bursts of pulses, Nature. 537 (2016) 84–88.

[156] J. Siegel, D. Puerto, W. Gawelda, G. Bachelier, J. Solis, L. Ehrentraut, J. Bonse, Plasma formation and structural modification below the visible ablation threshold in fused silica upon femtosecond laser irradiation, Appl. Phys. Lett. 91 (2007) 082902.

[157] N. Zhang, X. Zhu, J. Yang, X. Wang, M. Wang, Time-resolved shadowgraphs of material ejection in intense femtosecond laser ablation of aluminum, Phys. Rev. Lett. 99 (2007) 167602.

[158] C. Pasquier, M. Sentis, O. Utéza, N. Sanner, Characterization of surface ablation of dielectrics irradiated by 12-fs laser pulse in air, Laser Appl. Microelectron. Optoelectron. Manuf. XXI. 9735 (2016) 97350H.

[159] F. Watanabe, D.G. Cahill, B. Gundrum, R.S. Averback, Ablation of crystalline oxides by infrared femtosecond laser pulses, J. Appl. Phys. 100 (2006) 083519.

[160] N. Varkentina, N. Sanner, M. Lebugle, M. Sentis, O. Utéza, Absorption of a single 500 fs laser pulse at the surface of fused silica: Energy balance and ablation efficiency, J. Appl. Phys. 114 (2013) 173105.

[161] L. Haahr-Lillevang, K. Wædegaard, D.B. Sandkamm, A. Mouskeftaras, S. Guizard, P. Balling, Short-pulse laser excitation of quartz: experiments and modelling of transient optical properties and ablation, Appl. Phys. A. 120 (2015) 1221–1227.

[162] R.R. Gattass, E. Mazur, A round-up of recent papers in the field of photonics published by the physical sciences division of the Nature Publishing Group, Nat. Photonics. 2 (2008) 378–379.

[163] J. Schwarz, P. Rambo, M. Kimmel, B. Atherton, Measurement of nonlinear refractive index and ionization rates in air using a wavefront sensor, Opt. Express. 20 (2012) 8791–8803.

[164] C. Pasquier, M. Sentis, O. Utéza, N. Sanner, Predictable surface ablation of dielectrics with few-cycle laser pulse even beyond air ionization, Appl. Phys. Lett. 109 (2016) 051102.

[165] P. Whalen, J. V. Moloney, M. Kolesik, Self-focusing collapse distance in ultrashort pulses and measurement of nonlinear index, Opt. Lett. 36 (2011) 2542–2544.

[166] W. Hu, Y.C. Shin, G. King, Effect of air breakdown with a focusing lens on ultrashort laser ablation, Appl. Phys. Lett. 99 (2011) 234104.

[167] P.P. Rajeev, M. Gertsvolf, P.B. Corkum, D.M. Rayner, Field dependent avalanche ionization rates in dielectrics, Phys. Rev. Lett. 102 (2009) 083001.

[168] A. Ródenas, M. Gu, G. Corrielli, P. Paiè, S. John, A.K. Kar, R. Osellame, Three-dimensional femtosecond laser nanolithography of crystals, Nat. Photonics. 13 (2019) 105–109.

[169] R. Gattass, E. Mazur, Femtosecond laser micromachining in transparent materials, Nat. Photonics. 2 (2008) 219–225.

[170] M. Lenzner, J. Krüger, S. Sartania, Z. Cheng, C. Spielmann, G. Mourou, F. Kautek, Femtosecond optical breakdown in dielectrics, Phys. Rev. Lett. 80 (1998) 4076–4079.

[171] B.J. Nagy, L. Gallais, L. Vámos, D. Oszetzky, P. Rácz, P. Dombi, Direct comparison of kilohertz- and megahertz-repetition-rate femtosecond damage threshold, Opt. Lett. 40 (2015) 2525–2528.

[172] A.Y. Vorobyev, C. Guo, Enhanced absorptance of gold following multipulse femtosecond laser ablation, Phys. Rev. B. 72 (2005) 195422.

[173] X. Jia, X. Zhao, Numerical investigation of ultrashort laser interaction with dielectric materials based on a plasma-temperature combined model, J. Manuf. Process. 28 (2017) 508–514.

[174] W. Haynes, CRC handbook of chemistry and physics, CRC Press, Boca Raton, 2014.

[175] X. Zhao, Y.C. Shin, Laser–plasma interaction and plasma enhancement by ultrashort double-pulse ablation, Appl. Phys. B. 120 (2015) 81–87.

[176] M.E. Povarnitsyn, P.R. Levashov, D. V. Knyazev, Simulation of ultrafast bursts of subpicosecond pulses: In pursuit of efficiency, Appl. Phys. Lett. 112 (2018) 051603.

[177] M. Shimizu, M. Sakakura, M. Ohnishi, Y. Shimotsuma, T. Nakaya, K. Miura, K. Hirao, Mechanism of heat-modification inside a glass after irradiation with high-repetition rate femtosecond laser pulses, J. Appl. Phys. 108 (2010) 073533.

[178] S. Nolte, C. Momma, H. Jacobs, A. Tünnermann, B.N. Chichkov, B. Wellegehausen, H. Welling, Ablation of metals by ultrashort laser pulses, J. Opt. Soc. Am. B. 14 (1997) 2716–2722.

[179] D.J. Hwang, T.Y. Choi, C.P. Grigoropoulos, Liquid-assisted femtosecond laser drilling of straight and three-dimensional microchannels in glass, Appl. Phys. A. 79 (2004) 605–612.

[180] Y. Tan, W. Chu, P. Wang, W. Li, Z. Wang, Y. Cheng, Water-assisted laser drilling of high-aspect-ratio 3D microchannels in glass with spatiotemporally focused femtosecond laser pulses, Opt. Mater. Express. 9 (2019) 1971–1978.

[181] J. Qi, Z. Wang, J. Xu, Z. Lin, X. Li, W. Chu, Y. Cheng, Femtosecond laser induced selective etching in fused silica: optimization of the inscription conditions with a high-repetition-rate laser source, Opt. Express. 26 (2018) 29669–29678.

[182] P. Liu, L. Jiang, J. Hu, X. Yan, B. Xia, Y. Lu, Etching rate enhancement by shaped femtosecond pulse train electron dynamics control for microchannels fabrication in fused silica glass, Opt. Lett. 38 (2013) 4613–4616.

[183] S. Xu, C. Yao, H. Dou, W. Liao, X. Li, R. Ding, L. Zhang, H. Liu, X. Yuan, X. Zu, An investigation on 800 nm femtosecond laser ablation of K9 glass in air and vacuum, Appl. Surf. Sci. 406 (2017) 91–98.

[184] X. Jia, X. Zhao, Thermal accumulation at kilohertz repetition rates inside fused silica under ultrafast laser irradiation, Opt. Lett. 45 (2020) 3390–3393.

[185] P.T. Mannion, J. Magee, E. Coyne, G.M. O'Connor, T.J. Glynn, The effect of damage accumulation behaviour on ablation thresholds and damage morphology in ultrafast laser micro-machining of common metals in air, Appl. Surf. Sci. 233 (2004) 275–287.

[186] K. Lim, M. Durand, M. Baudelet, M. Richardson, Transition from linear-to nonlinear-focusing regime in filamentation, Sci. Rep. 4 (2014) 7217.

[187] D. Zhang, B. Ranjan, T. Tanaka, K. Sugioka, Underwater persistent bubble-assisted femtosecond laser ablation for hierarchical micro/nanostructuring, Int. J. Extrem. Manuf. 2 (2020) 015001.

[188] M. Domke, V. Matylitsky, S. Stroj, Surface ablation efficiency and quality of fs lasers in single-pulse mode, fs lasers in burst mode, and ns lasers, Appl. Surf. Sci. 505 (2020) 144594.